Title
Effects of Downscaling on the Low Swirl Burner

Author
Frank, Aaron Alex

Publication Date
2019

Peer reviewed|Thesis/dissertation

Effects of Downscaling on the Low Swirl Burner

by

Aaron Alex Frank

A dissertation submitted in partial satisfaction of the

requirements for the degree of

Doctor of Philosophy

in

Engineering - Mechanical Engineering

in the

Graduate Division

of the

University of California, Berkeley

Committee in charge:

Professor Jyh-Yuan Chen, Chair

Professor Robert Woodrow Dibble

Professor Alexis T. Bell

Summer 2019

Abstract

Effects of Downscaling on the Low Swirl Burner

by

Aaron Alex Frank

Doctor of Philosophy in Mechanical Engineering

University of California, Berkeley

Professor Jyh-Yuan Chen, Chair

There has been a recent surge of interest in power generation for a variety of small-scale energy applications. However, as devices are scaled down, a variety of problems emerge from both a system and combustion perspective. Addressing the latter, as a machine gets smaller, the effects of heat losses and fluid interaction with walls can quench radical species, effecting the combustion reactions. Furthermore, boundary layer and friction effects which are normally predictable and small (compared to the system output) at high Reynolds numbers can play a large role in the flowfield development as the size of the combustor shrinks and moves from turbulent flow into the laminar and transitional regime.

Seeking to specifically address this gap in available small-scale combustion technology, a potential candidate exists, however, it has only been demonstrated in larger-scale ($>$ 1.5") applications. This combustion technology, named the low swirl burner (LSB), offers a variety of potential benefits such as ultra low NO_x and CO emissions, low pressure drop, and high turndown ratios to suit these downscaled devices. This dissertation first seeks to understand whether the low swirl burner can be adapted to small scale ($\approx$ 3 kW) combustors and, secondly, attempts to shed light on the flowfield evolution as the LSB is downscaled.

Addressing the first aspect, the LSB was successfully scaled down to a 14 mm diameter unit and tested both qualitatively and quantitatively. Results indicated that miniaturized LSBs exhibited all of the operational characteristics of their large-scale counterparts, indicating they are a perfect candidate for future small-scale energy systems.

Secondly, in order to gain an understanding of the flowfield evolution of the miniaturized LSBs, three different diameter LSBs (12, 14, and 25.4 mm) were probed using laser diagnostics over a wide range of bulk inlet velocities and equivalence ratios. Results indicate that while the effects of scaling are evident in certain parameters, the fundamental properties of the LSB are clearly observed. Additionally, the diagnostics employed proved to be ineffective at measuring a key parameter, the turbulent burning velocity indicating that further diagnostics and modeling efforts may be required.

This work is dedicated to William David Goldberg for inspiring me to be an Engineer.

Acknowledgments

There are so many people that have helped me throughout my PhD and I am so grateful to every one of you. This short section is not long enough to truly express my gratitude but I will do my best.

First, I would like to thank Professors Andy Packard and Michael Frenklach for admitting me into Berkeley. Without you, I would have never been able to start this entire experience. With my transition into a new group, Andy could not have been more supportive and helpful at a time that was extremely stressful and uncertain. Thank you for helping me ensure my time at Berkeley did not end too early.

Secondly, I would like to thank everyone at Lawrence Berkeley National Laboratory for not only funding me and helping me find a research direction but also for guiding my research. It was such a pleasure working with Dr. Peter Therkelsen who helped ensure I was always focused on the big picture in my research and always provided great life advice. Peter hiring me at LBNL positively impacted my entire PhD experience. Thank you to Dr. Vi Rapp for always being supportive of my research and allowing me to be a part of the lab. Additionally, Dr. Robert K. Cheng was the guiding light for my research and an amazing mentor in every aspect. Robert essentially donated his time to help me find a research project even after he was retired. Thank you, Robert, for allowing me to work on your creation and hopefully adding some useful knowledge in the process. Through the years, everyone at the lab made the days so enjoyable. Thank you, Darren Sholes, for all the research advice, help, and good conversation during our time at the lab together. Thank you Miguel Sierra Aznar for providing support from the first day I arrived on campus and also during our time at LBNL. Mr. Gary Hubbard was instrumental in all of the data acquisition while also providing good conversations and plenty of sanity checks on my work.

Third, I would like to thank Professor JY Chen for allowing me to be a part of his group. His support in my research and help has been instrumental into making this all a possibility. Thank you Professor Robert Dibble for the enlightening conversations, life advice, and for being on my dissertation committee. Additionally, thank you Professor Alexis Bell for being on both my qualifying exam committee and dissertation committee, I truly appreciate it and appreciate the time you spent helping me.

Furthermore, to everyone in the combustion labs - Xian Shi, David Vuilleumier, Charles Scudiere, Daniel Pineda, and Tiernan Casey, thank you for all of your help and support, without you, none of this would have been possible.

Lastly, and not least by any means, I want to thank my wife, Ashley, for being

you and coming on this journey with me and making our lives in California so amazing. There were so many ups and downs and you have always been there through everything and have been so supportive of all my decisions. None of this would have been possible without you.

Nomenclature

α	Swirler vane angle	$-$
A_L	Area of laminar flame surface	mm^2
A_T	Area of wrinkled flame surface	mm^2
a_x	Normalized axial divergence rate	$1/s$
c	Progress variable $= (T - T_R)/(T_P - T_R)$	$-$
D	Diameter of LSB $= 2 * R_b$	mm
δ_T	Turbulent flame thickness	mm
η	Coordinate normal to flame front at c = 0.5	$-$
G_{ang}	Axial flux of angular momentum	N/m^2
G_x	Axial flux of axial momentum	N/m^2
HRR	Heat release rate	W
I_0	Stretch factor	$1/mm$
K	Turbulent flame speed correlation factor	$-$
k	Thermal conductivity	$W/m - K$
L	Swirler recess distance	mm
$\dot{m}$	Mass flow rate	kg/s
m	Ratio of mass flux $= \dot{m}_c/\dot{m}_a$	$-$
m_a	Mass flux through swirler annulus	$kg/m^2 - s$
m_c	Mass flux through swirler center channel	$kg/m^2 - s$
n	Data correlation constant	$-$
n_{LE}	Normal vector for leading edge of flame	$-$

ϕ	Equivalence ratio	$-$
$q^{'}$	2D turbulent kinetic energy $=1/2(u^{'2}+v^{'2})^{1/2}$	m/s
Re	Reynolds number	$-$
ρ	Density	kg/m^3
R	Ratio injector radius $= R_c/R_b$	$-$
R_b	Radius of LSB	mm
R_c	Radius of centerbody of LSB	mm
R_i	Outer radius of swirler	m
S	Swirl number	$-$
Σ	Flame surface density	$1/mm$
S_L	Unstretched laminar flame speed	m/s
S_T	Turbulent flame speed	m/s
S_{T-GC}	Global consumption turbulent flame speed	m/s
S_{T-GD}	Global displacement turbulent flame speed	m/s
S_{T-LC}	Local consumption turbulent flame speed	m/s
S_{T-LD}	Local displacement turbulent flame speed	m/s
T	Temperature	K
T_{AD}	Adiabatic flame temperature	K
TKE	Turbulence kinetic energy	m/s
T_P	Temperature of products	K
T_R	Temperature of reactants	K
U_0	Bulk inlet flow velocity	m/s
U	Local axial velocity	m/s
$u^{'}$	Axial RMS velocity	m/s
V	Local radial velocity	m/s
$v^{'}$	Radial RMS velocity	m/s
V_{flame}	Flame velocity	m/s

V_{gas}	Reactant velocity	m/s
x_f	Leading edge flame brush position	mm
x_0	Virtual origin position	mm
...	...	...

Abbreviations

1-D	One dimensional
2-D	Two dimensional
3-D	Three dimensional
ARPA - E	Advanced Research Projects Agency - Energy
BAT	Best available technology
CAI	California Analytical Instruments
CARB	California Air Resource Board
CDF	Cumulative density function
CDZ	Central divergence zone
CEC	California Energy Commission
CFD	Computational fluid dynamics
CHP	Combined heat and power
CO	Carbon monoxide
CRZ	Central recirculation zone
CV	Curved vane
DAQ	Data acquisition
DOE	Department of Energy
DMLS	Direct metal laser sintering
DNS	Direct numerical simulation
FPS	Frames per second

GENSETS	GENerators for Small Electric and Thermal Systems
GT	Gas turbine
GUI	Graphical user interface
HCCI	Homogeneous charge compression ignition
HSI	High swirl injector
ICE	Internal combustion engine
ISL	Inner shear layer
JAXA	Japan Aerospace EXploration Agency
LBNL	Lawrence Berkeley National Laboratory
LBO	Lean blowoff
LE	Leading edge
LES	Large eddy simulation
LHS	Left hand side
LP	Lean premixed
LSB	Low swirl burner
LSI	Low swirl injector
MDC	Metis Design Corporation
MFC	Mass flow controller
NETL	National Energy Technology Laboratory
NDIR	Non-dispersive infrared
NI	National instruments
NO_x	Nitrogen oxides
N-S	Navier-Stokes
NYSERDA	New York State Energy Research and Development Authority
ORZ	Outer recirculation zone
OSL	Outer shear layer
PDF	Probability density function

PIV	Particle image velocimetry
PLIF	Planar laser-induced fluorescence
RE	Reynolds number
RES	Renewable energy sources
RHS	Right hand side
RMS	Root mean square
RPM	Revolutions per minute
SLA	Stereolithography apparatus
SLPM	Standard liters per minute
THC	Total hydrocarbon
UCI	University of California, Irvine
UTRC	United Technologies Research Center
WSB	Weak swirl burner
ZAG	Zero air generator
...	...

List of Tables

List of Figures

Table of Contents

Chapter 1

Introduction

1.1 Motivation

Power generation portfolios have been evolving to integrate a larger share of renewable energy sources (RES) and as a result, the electric power grid faces the need to overcome reliability challenges brought on by their intermittent nature. RES dependence on weather and climate conditions limit when and where they can operate, and thus the demand for load balancing and peak shaving grid services increases. Motivated by the recent surge of low-cost natural gas and the establishment of a global liquefied natural gas (LNG) network, the power generation industry has shifted their focus to the development of technologies that overcome the new challenges while making use of cleaner and affordable fuels [1].

Addressing this issue, the United States Department of Energy's Advanced Research Projects Agency – Energy (ARPA - E) performed a study which indicated that a shift from the current method of generating electricity in centralized locations to a distributed combined heat and power (CHP) network could achieve an increase in overall system-wide energy efficiency from 50% to 83% [2]. In this distributed grid scenario, the energy efficiency would increase significantly because of two primary reasons; the recovery of waste heat for use in the household and the elimination of electricity transmission losses. In addition to an energy savings, this increase in energy efficiency also reduces the amount of CO_2 emitted into the atmosphere. In their analysis, it was estimated that a CHP system size with an electric output of 1 kW and a thermal output of 1.5 kW would be sufficient for most American households.

There are currently very few commercially available small-scale (< 5 kW) CHP systems on the market [3]. The most efficient small-scale system for sale on the market was developed by Honda and utilizes a conventional reciprocating internal combustion engine (ICE) to produce 1 kW of energy achieving 26.3% efficiency (fuel to electricity) [4]. Other technologies, such as Stirling engines and microturbines

approximately attain 20% efficiency and are all larger than 2 kW [5,6]. This therefore indicates that a gap exists in CHP technology at scales smaller than 5 kW due to limited system availability and their low operational efficiency.

Seeking to fill this void, ARPA - E created a program - Generators for Small Electric and Thermal Systems (GENSETS) to develop systems with 1 kW of electrical output and an efficiency of 40% (fuel to electricity) which is, in itself, an aggressive target at this scale. Furthermore, the program required that the system be able to meet California Air Resource Board (CARB) 2007 emissions levels, have a cost below $3,000, and guarantee a 10-year operational lifespan, all while maintaining noise levels below 55 dB at 3 feet among several other stringent requirements [2]. A graphic of how the system would be installed in a home can be seen in Figure 1.1.

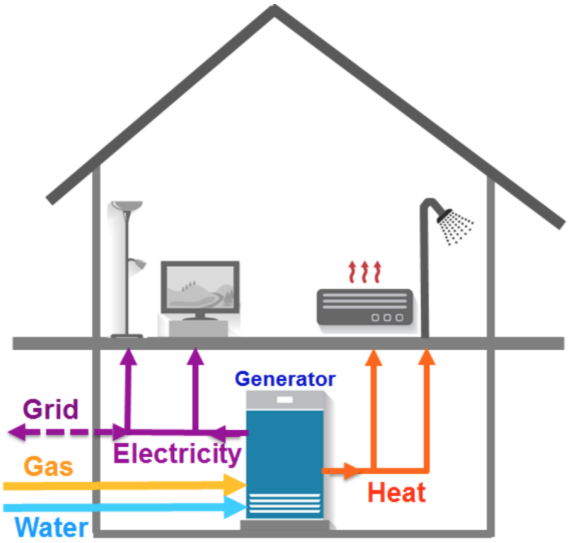

Figure 1.1: Schematic of the GENSETS system [7].

There are a myriad of technologies that can potentially meet the GENSETS requirements as demonstrated by the fourteen teams that were funded to achieve the ARPA - E targets. Some examples of the technologies utilized include Otto and Atkinson cycle two and four stroke ICEs, advanced cycle ICE engines such as homogeneous charge compression ignition (HCCI), external combustion cycles such as Stirling engines, thermoelectric generators, oscillating linear engines, and microturbines, among a few others. Each of these technologies has unique challenges at both an overall system level and at a combustion level when the device is scaled down to the 1 kW size, or any size below 5 kW for that matter.

For example, in the case of the ICE, as the combustion chamber is scaled down, the surface area-to-volume ratio of the combustion chamber rises, increasing heat losses significantly. Additionally, the friction between the piston and cylinder walls can become so high that it approaches the order of magnitude of the engine output power, reducing the engine efficiency significantly [8]. In order to mitigate these losses, operating the engine in an advanced mode such as HCCI may need to be considered in order to meet efficiency targets, however, these cycles have shown limited success

in smaller engines [9]. Multiple advanced engine technologies have been shown to work in controlled laboratory environments but success in the marketplace has been very limited.

In the case of microturbines (< 100 kW), similar challenges exist but others also emerge such as the importance of tight manufacturing tolerances of rotating components that are required to operate at very high RPM (> 150,000). Additionally, blade tip clearances become increasingly important as a significant portion of the flow can bypass the compressor and turbine blades, drastically decreasing the performance of the engine. Additionally, because of the very small component size, internal cooling of hot gaspath components is typically not possible, requiring lower operating temperatures for part durability and, therefore, lower thermodynamic efficiency [10]. From a combustion perspective, the smaller the system becomes, the higher the heat loses and possibility for interaction between the wall and radical species, quenching the combustion reaction. Furthermore, boundary layer and friction effects which are normally predictable and small (compared to the energy output of the system) at larger scales and high Reynolds numbers can play a major role in the flowfield development as the system shrinks in size and enters the laminar to the transitional flow regime [11, 12].

While the GENSETS program presents one specific case for the proliferation of small-scale systems, there has been a recent surge of interest in the miniaturization of combustion systems for various other applications, such as range extenders for electric vehicles and trucks as well as long-range drones. For automotive applications, companies are developing microturbines such as Metis Design Corporation (MDC) who has partnered with BMW to develop a 40 kW system [13] with many other systems being developed secretly. For long-range drone applications, Southwest Research Institute is currently developing a microturbine of unspecified size for unmanned aerial vehicles that is claimed to have a far greater operational lifetime and higher efficiency than any other system [14]. There are a multitude of projects currently under development and these two cases merely serve as examples of recent developments.

Furthermore, there has also been interest in the ability for systems to achieve high turndown ratios, which is defined as the highest power input divided by the lowest power input. While many devices operate at a single baseload operating condition (such as the microturbines discussed above), many systems require a variable range of operating conditions. One example of such a device is a tankless, on-demand residential water heater which requires the burner to have a turndown ratio of up to 30:1 [15]. In order to achieve this operational range in burner energy input, burner staging is typically required which adds costly valves and control software and, therefore additional complexity. A typical staging arrangement can be seen in Figure 1.2 where different portions of the burner are lit to match the load required by the user. Based on the complexity and cost of staging, it is highly desirable to have a single burner that can achieve this level of turndown without any hardware or software.

In 2015, the New York State Energy Research and Development Authority (NYSERDA) funded a development program to determine if a single burner could be used in an on-demand water heater while meeting stringent emissions, ultra-low pressure drop < 1 psi, and achieve turndown ratios greater than 20:1. Currently, there are no

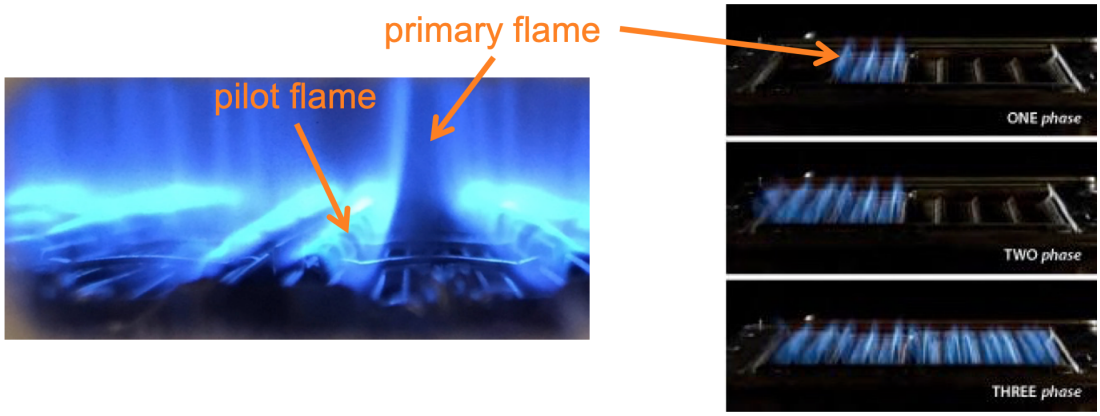

Figure 1.2: On-demand tankless water heater staged burner [16].

burners on the market which can meet this criteria without having a staged combustor design, similar to what is shown above.

1.2 Research Goals and Objectives

There is a potential burner technology that can potentially meet the requirements of these future downsized systems: ultra low emissions without aftertreatment, ultra low pressure drop, fuel feedstock flexibility, and high turndown ratios which would not require a staged combustion system described above. This combustion technology, named the low swirl burner (LSB), however, has only been applied to large-scale systems. There is currently little data and knowledge of the flowfield characteristics and operability of the LSB as it is scaled down to the sizes needed for the future energy systems described previously. As a flow device is miniaturized, fundamental questions arise about the impact of scaling on the fluid dynamics of the flowfield and how they are altered by scale. This dissertation seeks to develop an understanding of the flowfield evolution as the LSB is scaled down to sizes never before tested while also investigating its applicability to future small-scale energy systems.

In order to attain these research goals, the following objectives are identified and pursued:

1. **Perform literature review of all LSB studies to understand the flowfield and operational characteristics that have been exhibited.**

2. **Design and manufacture hardware to measure the flowfield properties as well as operational characteristics of the downscaled LSB hardware.**

3. **Conduct experiments to determine applicability of the LSB to small-scale energy systems.**

4. **Collect data to test whether the flowfield exhibits self-similar behavior.**

5. **Analyze data and provide insight into the effects of scaling on the LSB.**

This investigation will extend our knowledge of the LSB into scales and operating regimes that are not currently well understood. From an engineering perspective, this dissertation will also discuss the feasibility of using the LSB for miniaturized energy systems and the design considerations involved for such applications.

The first section of Chapter 2 provides a brief background of lean premixed combustion, discussing pertinent considerations in the design of low emission flames. The second portion of the chapter provides a literature review of previous LSB studies, a detailed overview of the LSB flame characteristics, and lastly a discussion of the knowledge gap in the current understanding of small-scale LSBs. The details of the experimental setup, facility, and considerations are discussed in Chapter 3. Chapter 4 details the experimental test results of the miniaturized LSB including the flowfield interrogation. Lastly, Chapter 5 details the conclusions from this dissertation and future work.

Chapter 2

Background

This chapter will provide a brief background on the design considerations for lean premixed combustion devices with a brief history of the LSB. A literature review of previous LSB research and the current understanding of the flowfield is also presented.

2.1 Combustor Sizing Nomenclature

The research presented in this dissertation involves the downsizing of combustion hardware that has typically been applied to larger-scale (>1.5" diameter) industrial applications. In the search for the appropriate terminology to define the scale of burner, it has become clear that the nomenclature for the scale of combustion devices is often a point of ambiguity among researchers. Two names are often utilized, the "micro-scale" or the "meso-scale" and three unique methods are used to classify a device or combustor into either category.

The first and most common method uses a physical dimension within the combustion chamber. By this definition, conventionally, if the length is under 1 mm, the device is in the micro-scale regime. If it is larger than 1 mm but of the order of 1 cm, then it is considered to be meso-scale. The second method utilizes a reference parameter within the flame - the quenching distance [17]. This distance is defined as the "minimum distance at which a flame can approach a material surface before quenching" where quenching is the point at which the flame can not propagate due to the heat losses being greater than the heat generated by the combustion reaction [17]. Lastly, the third definition compares the system size to that of a conventional large-scale unit such as a "microturbine" combustor would therefore be a "micro" combustor [18].

Depending on which definition is used, the work presented in this dissertation could either be defined in the meso-scale or the micro-scale. If one considers the diameter of the low swirl burner as the characteristic combustor length, then this work (<1") would fall into the meso-scale, however, if the application of the small-scale low swirl burners are considered, such as a Stirling engine or microturbine (with an output <100 kW), then the scale would be classified in the micro regime. In order to differentiate this work and avoid confusion, the LSBs studied in this dissertation

will be referred to as "miniaturized".

2.2 Premixed Combustion Fundamentals

There are a wide variety of methods to continuously (as opposed to discrete combustion events in an ICE for example) burn a fuel and oxidizer in order to produce useful heat and work. The method of burning gaseous or liquid fuels is typically divided into two forms, premixed or non-premixed. In premixed systems, the fuel and air are combined upstream of the flame front before they are burned whereas in the case of non-premixed systems, the fuel and air react at the location of the flame front.

Non-premixed systems are prevalent in industrial and commercial applications (specifically transportation) because they are safe and easy to design and use. However, emissions, specifically NO_x are high because at the flame front, the mixture burns at stoichiometric conditions and thus a high temperature. More details about the mechanisms for NO_x production in flames will be discussed in the sections below. In stationary (non-transportation) combustion systems, in order to achieve low emissions, it is necessary to premix the fuel and air and operate the burner at a cooler flame temperature which can achieve low emissions without catalytic or non-catalytic aftertreatment.

2.2.1 NO_x Pathways

The production of nitric oxides, NO_x, is of great concern in the design of any combustion device because of its harmful environmental effects and strict regulation limiting emissions. It is therefore necessary to introduce the important NO_x pathways and how they can be mitigated. However, this discussion is not meant to be comprehensive but rather briefly touch on the subject matter.

Thermal

Thermal NO also referred to as Zeldovich NO is named after Y.B. Zeldovich who theorized that NO could be produced in high temperature environments. NO is produced by the three reactions below:

$$O + N_2 \xrightarrow{k1} NO + N \tag{2.1}$$

$$N + O_2 \xrightarrow{k2} NO + O \tag{2.2}$$

$$N + OH \xrightarrow{k3} NO + H \tag{2.3}$$

The name "thermal" is derived from the high activation temperature required in Equation 2.1 to break the nitrogen triple bond which is the rate limiting step of these three reactions [19]. The most noteworthy aspect about thermal NO is that it is highly overpredicted by equilibrium chemistry, meaning that the amount

of time that the products spend at high temperature is very important to the NO concentration. Thermal NO is almost always the most significant contributor to the total NO concentration in the system, and as a result, practical systems almost always operate under 1800 K [20]. Figure 2.1 shows the equilibrium flame temperature calculated using CHEMKIN for methane/air with an inlet temperature of 300 K using the GRI 3.0. Here, the temperature increases with the equivalence ratio, ϕ, up until slightly after 1, whereby the temperature decreases with increasing ϕ. In order to achieve temperatures below 1800 K, combustors are typically run lean as opposed to rich in order to avoid the production of unburned fuel and carbon monoxide.

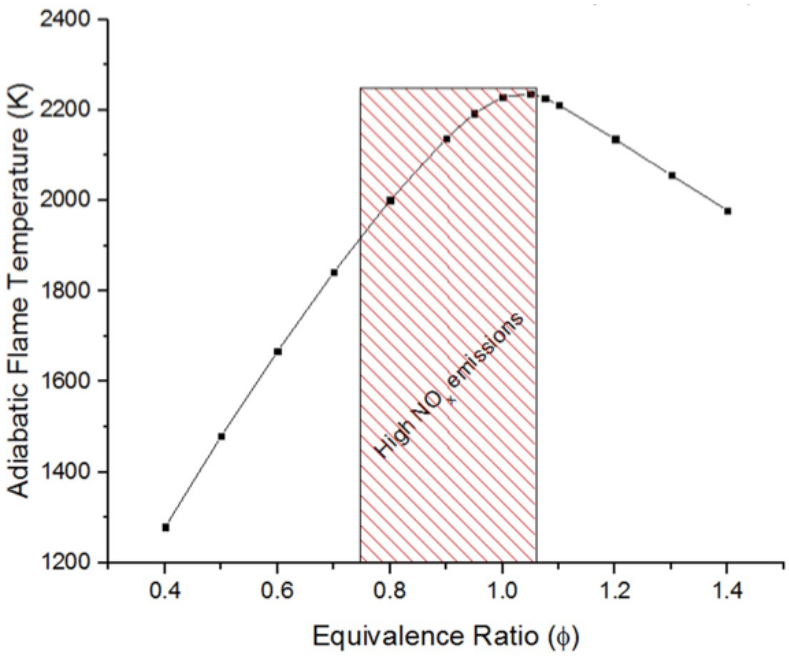

Figure 2.1: Equilibrium temperature vs. equivalence ratio for methane

Prompt

Prompt NO, also known as Fenimore NO was discovered in a flat flame burner near the flame front and was thus "prompt". The mechanism for prompt NO is significantly more complicated than thermal NO (which occurs after the oxidization of the fuel) because it is interlinked with CH radicals in the flame front. The reactions are as follows [21]:

$$CH + N_2 \longrightarrow HCN + N \tag{2.4}$$

$$CH_2 + N_2 \longrightarrow HCN + NH \tag{2.5}$$

$$CH_2 + N_2 \longrightarrow H_2CN + N \tag{2.6}$$

$$C + N_2 \longrightarrow CN + N \tag{2.7}$$

The conversion of the products in the above reactions into NO is very complex but extensive studies have been performed and this process and reaction pathways are well understood.

Fuel Bound Nitrogen

The conversion of fuel bound nitrogen to NO has been extensively studied. Nitrogen is converted to hydrogen cyanide and ammonia before reacting to form NO. For lean premixed combustion, this pathway is negligible because gaseous fuels often contain little nitrogen [22].

Nitric Oxide

The last and most overlooked pathway is similar to the thermal pathway in that it involves molecular nitrogen and can be significant in lean premixed combustion systems. In lean conditions, because the flame is cool, thermal NO is small and the formation of CH is suppressed leading to low prompt NO. In these cases, and at higher pressures, the N_2O mechanism can be a major contributor by the following pathway.

$$N_2 + O + M \longrightarrow N_2O + M \tag{2.8}$$

$$N_2O + O \longrightarrow NO + NO \tag{2.9}$$

where M represents a third body reaction [19].

2.2.2 Flame Stabilization

The work presented in this thesis focuses exclusively on premixed combustion and thus a few important factors are discussed in the design of these systems. One essential principal in the design of any combustion is to anchor or "hold" the flame at a specific location within the flowfield. This is accomplished by matching the local burning velocity of the flame front to the velocity of the non-reacted local mean velocity [23]. The mean velocity upstream of the flame front is often significantly larger than the local velocity needed to sustain a flame and a variety of methods are used to decelerate the reactant velocity.

There are several methods that are used to anchor the flame at a desired location. These include low-velocity bypass ports, refractory burner tiles, bluff-body flame-holders, swirl or jet-induced recirculating flows, or abrupt geometry changes such as a rapid increase in flow area creating recirculating separated flow [23]. It can be noted that the above reference does not mention the use of a diverging flowfield that is created by the low swirl burner (LSB) even though his book was written nine years after the LSB was invented and patented.

For gas turbines or any type of high energy density combustion system, two aerodynamic stabilization methods are primarily used, bluff-body and swirl or a combination of the two. In the case of bluff-body stabilization, a body is inserted into the bulk flow which creates a recirculation zone downstream where the flame can anchor. In the case of swirl stabilization, the flow is swirled in a manner that creates a recirculation zone which decelerates the flow and brings in hot gases to ignite the fresh fuel and air.

A typical geometry configuration for a bluff-body, swirl-stabilized lean premixed (LP) gas turbine combustor is shown in Figure 2.2 and is referred to as a high swirl injector (HSI). In this configuration, swirl vanes are placed in the annulus with a center channel that is blocked (some configurations may have a pilot hole in this center body) creating a central recirculation zone (CRZ) downstream in the core of the flow. For this design, and LP burners in general, the fuel is injected and mixed upstream of the swirler either by some type of fuel injector or holes within the vanes.

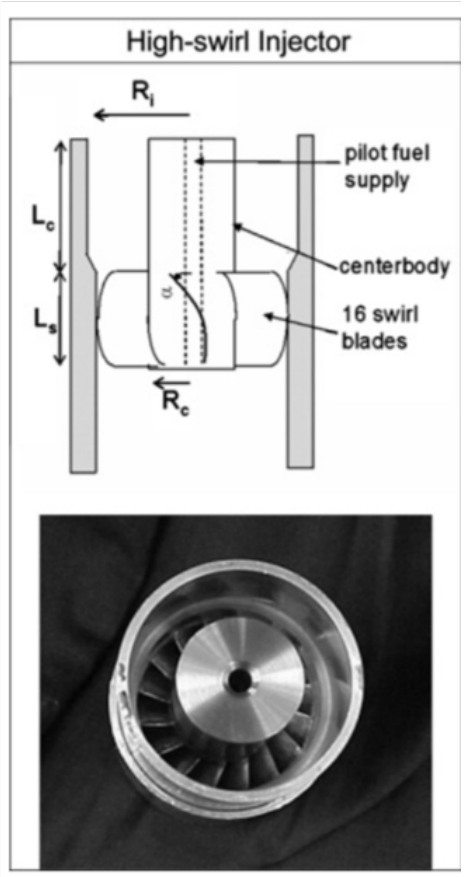

Figure 2.2: High swirl injector geometry for gas turbine applications [24].

The flowfield and flame generated by this geometry can be seen in Figure 2.3. In this case, the flame attaches to the bluff-body and stabilizes along the inner shear layer (ISL) at the boundary of the CRZ in the core of the flow. The expansion of the swirling flow into the volume cause the outer shear layer (OSL) and outer recirculation zone (ORZ) shown in the image [25, 26]. It can be noted that due to the large-scale

recirculation zone within the flame front, the combustion products spend a relatively long time at high temperatures which results in the production of thermal NO_x, a consequence of HSI burners.

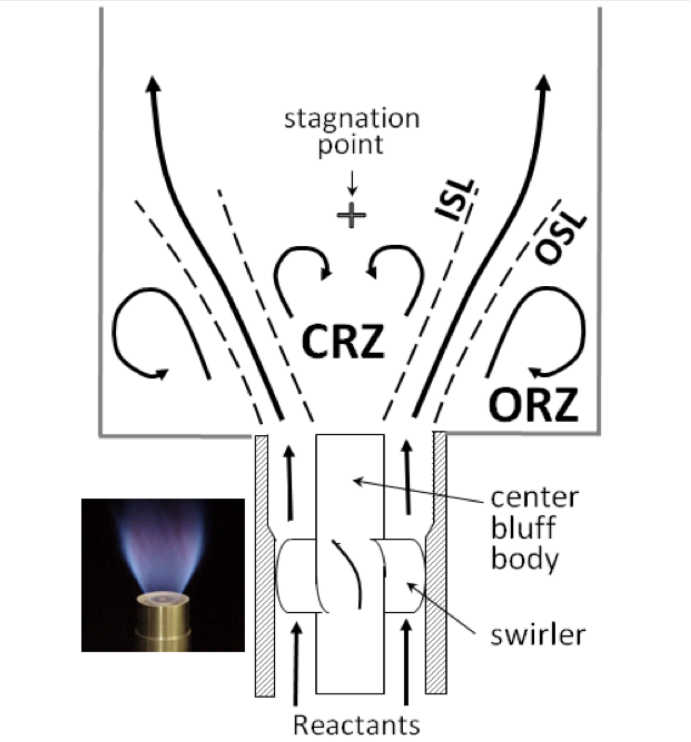

Figure 2.3: Flowfield and flame of a typical gas turbine high swirl injector [26].

One key parameter that is used to characterize a swirl burner is known as the swirl number, S, which is shown below:

$$S = \frac{G_{ang}}{G_x \cdot R_i} \tag{2.10}$$

where G_{ang} is the axial flux of angular momentum, G_x is the axial flux of linear momentum and R_i is the outer radius of the annulus. The swirl number for most HSI configurations studied in various laboratories have been in the range of $0.6 < S < 1.6$ [24].

2.3 Low Swirl Burner History and Literature Review

The LSB, often referred to as the low swirl injector (LSI) and the weak swirl burner (WSB), was invented under the guidance of Robert K. Cheng at Lawrence Berkeley National Laboratory in 1991. The primary purpose of developing the LSB was to create a flame that could be stabilized in the open without any physical obstructions near the flame front so that the system would be amenable to laser diagnostics [27].

Furthermore, it was noted that the flame created in this configuration can be considered to be 1-D and planar, meaning that the flame front at the centerline can be considered normal to the approaching flow which is optimal for determining flame properties. The LSB flame is freely propagating and is stabilized by creating a central turbulent region of non-swirling flow which is generated by inserting a turbulence generating grid and an outer annulus that swirls flow around the core.

The flowfield generated by the LSB is novel and unique, generating a flame that is stabilized in a different manner than every other device. In 1993, a patent was granted by the US Patent and Trademark Office for the type of flowfield developed in the LSB under Patent # 5,735,681. In the early studies of the LSB [27–29], the swirling flow was provided by tangential air jets which can be seen in Figure 2.4. This configuration which was 114 mm in diameter allowed the adjustment of the flow properties "on the fly" by changing the flow rates of air to the core and the swirling flow.

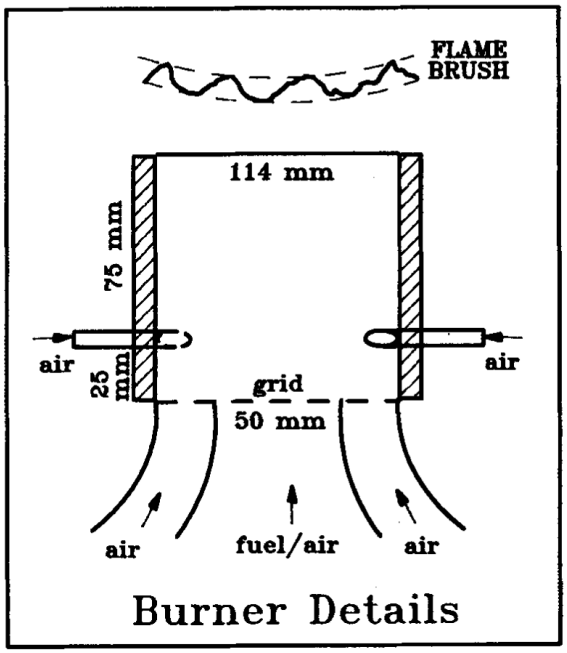

Figure 2.4: Jet LSB with center co-flow and tangential air jets to produce swirl [27].

After the discovery of this unique flowfield, two paths were taken; one seeking to understand whether the LSB could be used in commercial applications, and secondly, to develop an understanding of the flowfield from a scientific perspective. This development occured in the mid-1990s and first focused on using an enclosure to simulate a combustor wall and then moved to adapting the LSB to various real-world combustion devices. One early adaptation was the coupling of the LSB with a heat exchanger from a 15 kW Telstar spa heater to prove its stability and emissions performance [30]. This study utilized a 5 cm diameter LSB that could be run with an output range of 8 to 80 kW. While the bulk inlet velocities are not reported, a quick calculation determines that the operable range of the LSB in this study was from

approximately 2 to 20 m/s, assuming standard temperature and pressure for the air at the lowest ϕ tested of 0.6.

Subsequent experimental studies similarly focused on the flowfield affects when the LSB was confined in different enclosure diameters with varying exhaust back pressure to simulate conditions in commercial heating appliances. These tests utilized the same LSB from the Telstar experiments at similar conditions to understand the flowfield impacts. Results indicated little change between the LSB flames in the open compared to enclosed flames with varying downstream conditions [31]. Both of these early studies revealed that at sufficiently lean conditions, ultra-low NO_x emissions could be consistently achieved.

This successful work then moved to scaling the original LSB to larger sizes for use in industrial heaters. The LSBs studied were 10 cm in diameter and were operated with a bulk inlet velocity range of 6.2 to 24.8 m/s, significantly larger and with a higher output than any previous studies [32].

In order to utilize a design that could be used in commercial devices, a new iteration of the LSB was developed consisting of a fixed geometry vane swirler that can be seen in Figure 2.5. The advantage of the vane LSB is that no moving parts nor adjustments were required to achieve the correct flowfield aerodynamics. The design of the LSB is such that the vanes swirl the flow passing through the annulus and a plate is mounted in the center serving two purposes. The first purpose is to generate turbulence and the second is a means to provide a pressure drop to achieve the correct mass flow rate split between the swirling and non-swirling flow. This incarnation of the LSB, also known as the "Mechanical swirler for a low-NOx, weak-swirl burner" was issued a new patent for the design in 1999 under US Patent # 5,879,148.

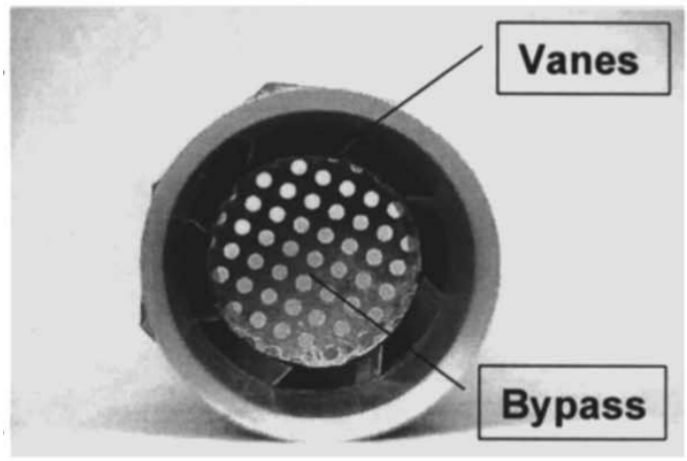

Figure 2.5: Vane LSB showing vanes to induce swirl in the annulus and the perforated plate in the center region [33].

This geometry was further studied at larger scales in the early 2000s with the LSB demonstrating and cementing its viability as a commercial burner. The conditions tested with the 10.16 cm diameter swirler ranged from a bulk inlet velocity of approximately 3 to about 25 m/s which represented an output of 73 kW to 280 kW

respectively [33]. Additional development was undertaken using a 5.2 cm diameter LSB with varying fuel feedstocks [34]. Further studies were performed at higher bulk inlet velocities (23 - 38 m/s) to test the LSB applicability to gas turbines [35].

Concurrent with the commercial development of the LSB, many studies were being performed to understand the LSB from a scientific perspective. Studies in the early to mid-2000s focused on understanding the fundamental flame and flowfield characteristics of the LSB, utilizing the 5 cm jet LSB. To understand the flame structure of the LSB and to measure the turbulent burning velocity over a wide range of inlet velocities additional experiments were performed [36–40].

Starting in 2006 and continuing until the present day studies focused on adapting the LSB to gas turbines in a partnership with Solar Turbines in San Diego, CA, among others. In this work, a large LSB was created with a diameter of 8 inches (203.2 mm) and operated at elevated temperatures and pressures to understand if the LSB could successfully be adopted for gas turbines. During this time, there was also a large amount of interest in understanding the fuel flexibility of the LSB. This was further explored by using a variety of fuels ranging from simulated landfill gas to hydrogen and many other mixtures [41–49]. These works utilized the LSBs with diameters ranging from 1.5" (38 mm) to the aforementioned 8" (203 mm) at bulk inlet velocities from 3 to 60 m/s. The work performed by Beerer et al. [47,48] is particularly relevant to the work presented in this thesis because they are the smallest LSB that has been extensively tested.

An open question at the time was how different combustor geometries (enclosures) would affect the flowfield evolution. The results indicated that the enclosure ultimately does not impact the flowfield [50]. All of these studies demonstrated that the LSB would be highly suitable as a gas turbine combustor with virtually any fuel.

With increasing computational ability, interest in testing numerical models, and a need for an in depth understanding of the LSB flowfield and flame structure, a series of numerical studies were undertaken starting in the mid 2000s and still continue to the present day. The most complex and time consuming but accurate modeling efforts were completed using Direct Numerical Simulation (DNS) which solves the Navier Stokes (N-S) equation without the use of any turbulence model. DNS produces the most accurate solution possible, however, it is extremely computationally expensive and thus rarely performed on full-scale burners at realistic operating parameters. Three of these studies were performed by the computational group at Lawrence Berkeley National Laboratory (LBNL) on a 50 mm diameter LSB with a velocity range of 6.2 to 31 m/s, seeking to understand the flow structure and turbulence/chemistry interaction with fuel feedstocks [51–53]. Furthermore, the computational group at California Institute of Technology in Pasadena, CA has recently been interested in using DNS to model the miniaturized LSBs in this dissertation due to the small size of the model.

Further studies were performed by the group at LBNL in cooperation with the Japan Aerospace Exploration Agency (JAXA) to further enhance the knowledge about flame structure with the hope of extending this knowledge to premixed flames in general [54, 55]. The work performed by Day et al. [54] is particularly interesting and relevant to the research in this dissertation because it discusses the transitional

nature of flowfield development at lower bulk inlet velocities. As a result of this, they authors choose to simulate only higher bulk inlet velocities due to the transitional nature.

There were also many studies performed by Lund University in Sweden along with other partner organizations that utilized more "conventional" computational fluid dynamics (CFD) methods, such as Large Eddy Simulation (LES) coupled with experimental data on their 50 mm LSB to validate models and understand the flame stability mechanisms [56–62]. Parallel to this work, numerous groups were studying the thermoacoustic instabilities of the LSB to gain an understanding of this phenomenon in the LSB. The first of these studies was performed by a team at the California Institute of Technology and the University of Iowa who used a LSB with a diameter of 2.54 cm at 4 m/s bulk inlet velocity [63,64]. These studies did not characterize the flowfield and were only seeking to measure to acoustic coupling mechanisms. Additional thermoacoustic studies were performed on the LSB by the National Energy Technology Laboratory (NETL), United Technologies Research Center (UTRC), LBNL, Siemens Energy Inc. and JAXA [26, 65–67]. The LSBs studied were all 50 mm in diameter or larger with bulk inlet velocities larger than 10 m/s.

One particular study that is pertinent to the work performed in this dissertation was performed by NETL in partnership with ANSYS Incorporated to develop a modeling method for the LSB. In this study, a small 15.8 mm LSB was manufactured specifically to minimize the computational cost of the simulation. Before the work presented in this dissertation, this was the smallest LSB ever tested. This work utilized the LSB in a quartz enclosure and provided some diagnostics, but the authors did not perform a full analysis on the flowfield properties [68].

Lastly, one particularly interesting study is the development of a liquid fueled LSB by JAXA [69]. This work demonstrated the applicability of the LSB for transportation applications. It is the opinion of the author that liquid fuels are the most promising of the future application of the LSB.

2.4 LSB Fundamentals

2.4.1 LSB Flowfield Properties

As mentioned previously, there are many features to the LSB that render it materially different than other LP burners. This section will describe the aerodynamic properties, parameters, and principals governing the LSB.

The LSB geometry is very similar to the HSI except that the center channel is not blocked, but instead occupied by a turbulence generator, such as a grid or perforated plate previously shown in Figure 2.5. A key burner parameter is the swirl number which was derived specifically for the LSB geometry by Littlejohn et al. [34] to be:

$$S = \frac{2}{3}\tan\alpha\frac{1-R^3}{1-R^2+[m^2(1/R^2-1)]R^2} \tag{2.11}$$

where R is the ratio R_c/R_b, R_c is the radius of the centerbody, and R_b represents

the radius of the burner. The angle of the vanes is represented by α, and m is the ratio of the mass flux through the center channel ($\dot{m}_c$) to the mass flux through the annulus ($\dot{m}_a$). Previous studies have noted that S for the LSB was targeted to be in the range of $0.4 < S < 0.55$ for natural gas [70], lower than $S > 0.6$ for HSIs. While S is a useful parameter often used to distinguish between the HSI and LSB, as well as comparing the properties of similar injector types, it does not provide any description of the flowfield and therefore not the most useful metric. The dimensions listed as well as the mounting configuration of the LSB are shown in Figure 2.6.

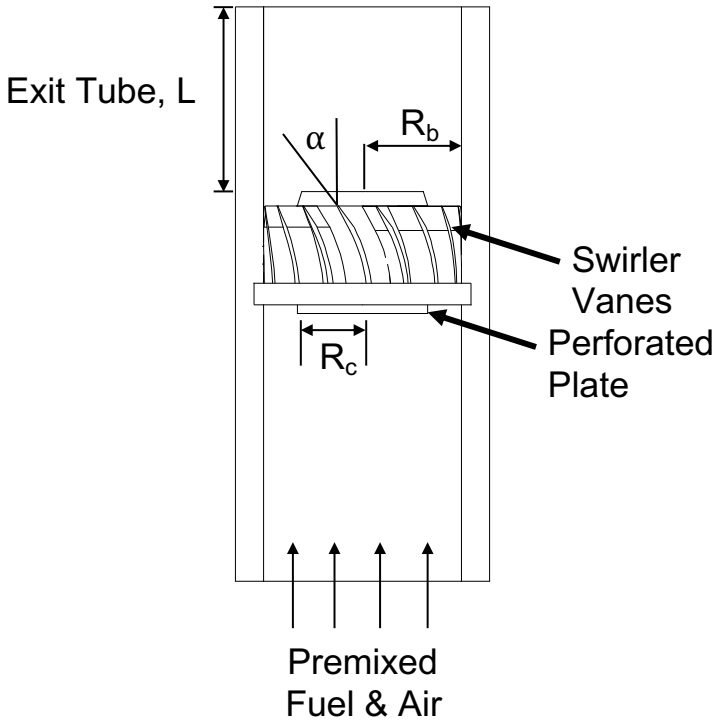

Figure 2.6: LSB schematics showing mounting position in a tube and dimensional parameters.

In order to provide a guideline in the design of the LSB for gas turbines, a parametric study performed in 2012 by the LBNL combustion group Therkelsen et al. [70] was performed to determine the appropriate ranges for the swirler dimensions. It was found that the exit tube length, L should be within the range of 1 to 1.5 * D, the outer diameter of the swirler (2 * R_b). This distance allows the interaction of the swirling annulus and non-swirling inner core. Additionally, α, the recommended vane angle for hydrocarbon fuels should be within the range of 30 to 42 degrees and between 30 and 35 degrees for high-hydrogen fuels. The parameter, R (the ratio of the center channel R_c to the injector radius, R_b) was optimally in the range of 0.5 to 0.7. It was also found that instead of using the swirl number directly as a design parameter, the ratio of S/α was a better metric to characterize the burner and should be in the range of 0.7 to 0.8.

As briefly described in the LSB history section, the LSB flame is lifted and not

attached to a body, such as in the case of the HSI. This feature is unique in that it provides optical access to the flame, but is also beneficial in practical systems as the flame does not degrade the surrounding hardware due to high temperatures. A visual image of the flame with coordinates employed in this work can be seen in Figure 2.7. The direction of the axial flow is denoted by x and the horizontal direction is defined by r. The velocity in the axial direction is defined by U and the velocity in the radial direction is defined by V. The root mean square (rms) axial and radial velocities are represented by u' and v' respectively.

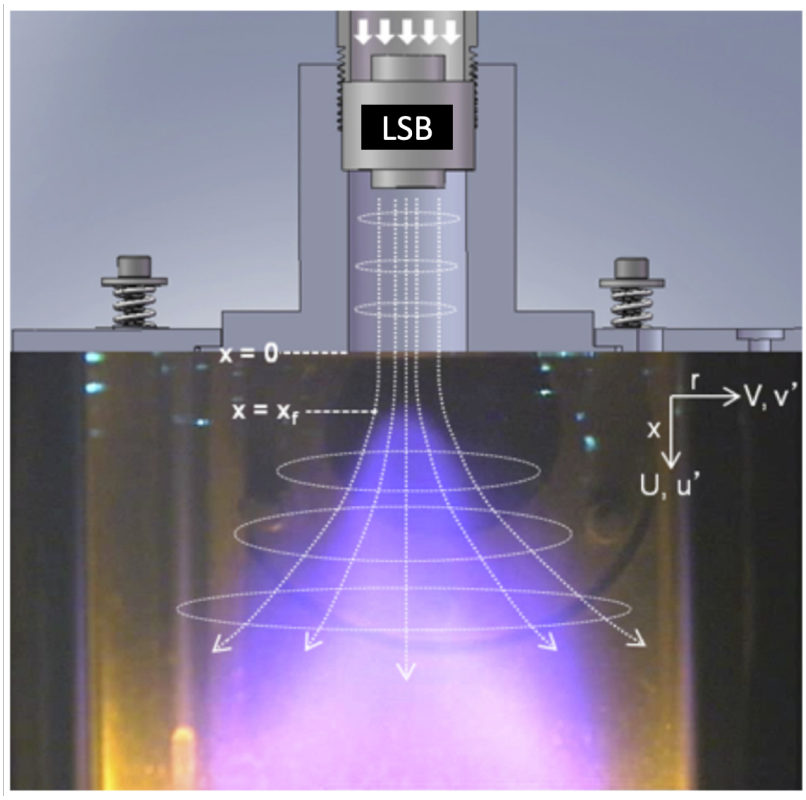

Figure 2.7: LSB flame with coordinates and streamlines through the flame front [48].

The LSB is stabilized only by aerodynamics and lacks a CRZ due to the lower swirl intensity and flow within the center channel that is absent on HSIs. Most importantly, the LSB geometry inhibits the vortex breakdown that is the cornerstone of HSI burners. The premise of the LSB flowfield is that the flame stabilizes at the location where the local axial reactant velocity matches the flame propagation or the local displacement turbulent flame speed, $S_{T\text{-}LD}$. The details and importance of the turbulent flame speed will be discussed in detail later in this section. The core flow of the LSB contains a central divergence zone (CDZ) which is a result of the swirling flow expanding radially when it discharges from the LSB mounting nozzle into a larger volume or the open air. Upon discharge, the velocity in the central core region of the LSB linearly decelerates as a result of this expansion. As in the case of the HSI, the ORZ does not have an influence on the flame stability.

In the development of the LSB for gas turbine applications, many rigorous studies

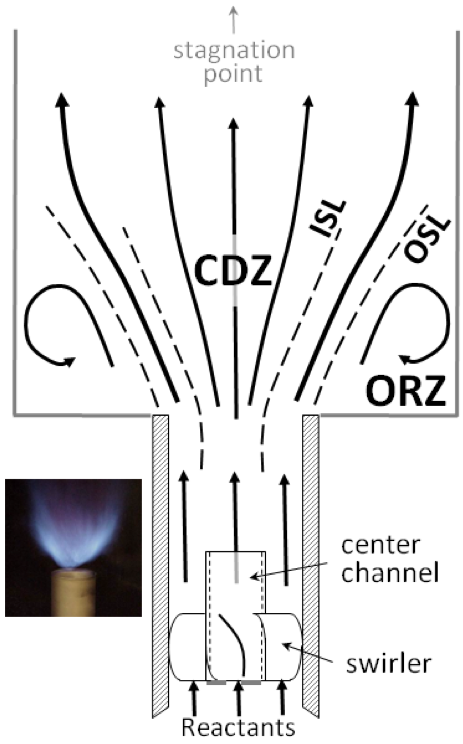

Figure 2.8: Flowfield and flame of a LSB [26].

were undertaken to fully characterize the flowfield under a variety of conditions. If the flow is normal to the flame front in the core region of the flame (or the centerline), it is evident that the following expression could be written for the axial location of the flame front, x_f.

$$U = S_{T-LD} \tag{2.12}$$

This equation simply states that the local axial velocity, U, is equal to the local displacement flame speed which is propagating against the velocity down ramp of the reactants. Earlier studies have shown that the flow linearly decelerates along the centerline. Therefore Equation 2.12 can be manipulated to utilize the linear deceleration, the axial stretch rate normalized by the bulk inlet velocity, $dU/dx/U_0$ also known as a_x, the bulk inlet velocity, U_0, the flame position, x_f, and the virtual origin, x_0. The virtual origin is the axial location in the flowfield where $u = U_0$ which is a negative value due to the fact that the zero axial location is the LSB nozzle exit or dump plane. We can therefore, based on these quantities, write the following expression:

$$U_0 + \frac{dU}{dx}(x_f - x_0) = S_{T-LD} \tag{2.13}$$

After which we can divide all terms by U_0 resulting in:

$$1 + \frac{dU}{dx}\frac{(x_f - x_0)}{U_0} = \frac{S_{T-LD}}{U_0} \tag{2.14}$$

This expression and definition of the terms discussed can best be visualized in Figure 2.9 below. The x-axis is the axial distance from the dump plane (x = 0) through the flame and the y-axis is the local axial velocity normalized to the bulk inlet velocity. The location of the flame front is shown as the turning point in the axial velocity from a deceleration to an acceleration which is caused by the presence of the flame. Furthermore, the slope of the curve leading up to x_f is defined as a_x, as previously discussed.

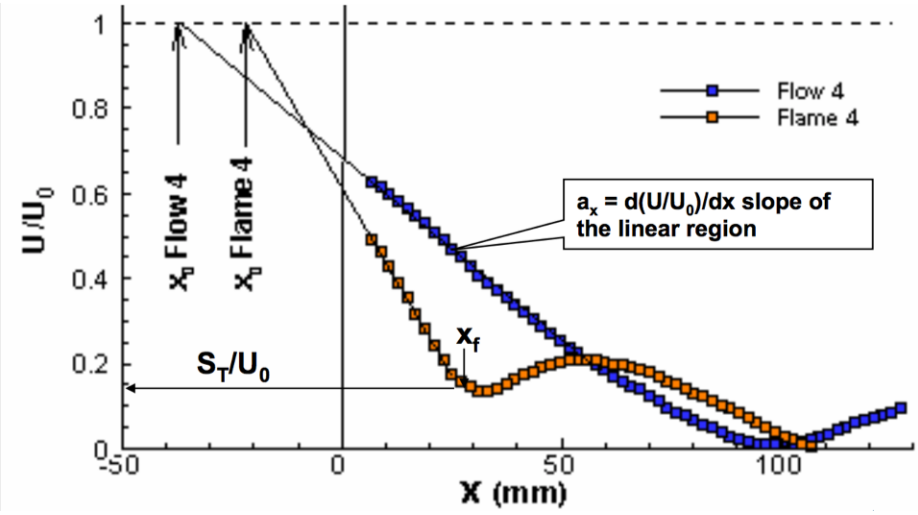

Figure 2.9: Description of the virtual origin, normalized axial divergence, and axial flame location [42].

Now, focusing on the right hand side (RHS) of Equation 2.14, an expression for the value of $S_{T\text{-}LD}$ can be obtained. In 1940, Damköhler presented a theoretical expression which related the laminar burning velocity to the turbulent burning velocity for a specific set of conditions known as the flamelet regime. This regime covers an area of combustion where chemistry is fast compared to transport processes [71]. In his analysis, Damköhler determined that wrinkled flames burn faster than laminar flames due to the increase in surface area of the flame front caused by velocity fluctuations. In other words, $S_T/S_L = A_T/A_L$ where the subscript T refers to the turbulent values and L refers to laminar values. In the flamelet regime, the flame is considered to propagate locally with the laminar flame speed. In subsequent studies, in order to match the abundance of experimental data collected in laboratories, the follow expression was written with an adjustable exponent [72, 73].

$$\frac{S_T}{S_L} = 1 + K\left(\frac{v'}{S_L}\right)^n \tag{2.15}$$

where K is a function of the length scales and n varies from 0.5 to 1. If n is less than

one, as v' increases, S_T will flatten or "bend". In the case of the LSB, the "bending" described by Peters [?] does not occur. The dependence of $S_{T\text{-}LD}$ on u' is linear which can be seen in Figure 2.10 where the slope of this curve is the term K in the equation above. For the LSB, K is only a function of the fuel group and n = 1 which points to a discrepancy between the information printed by Peters [?] and various works performed on the LSB by R.K Cheng [45] and others.

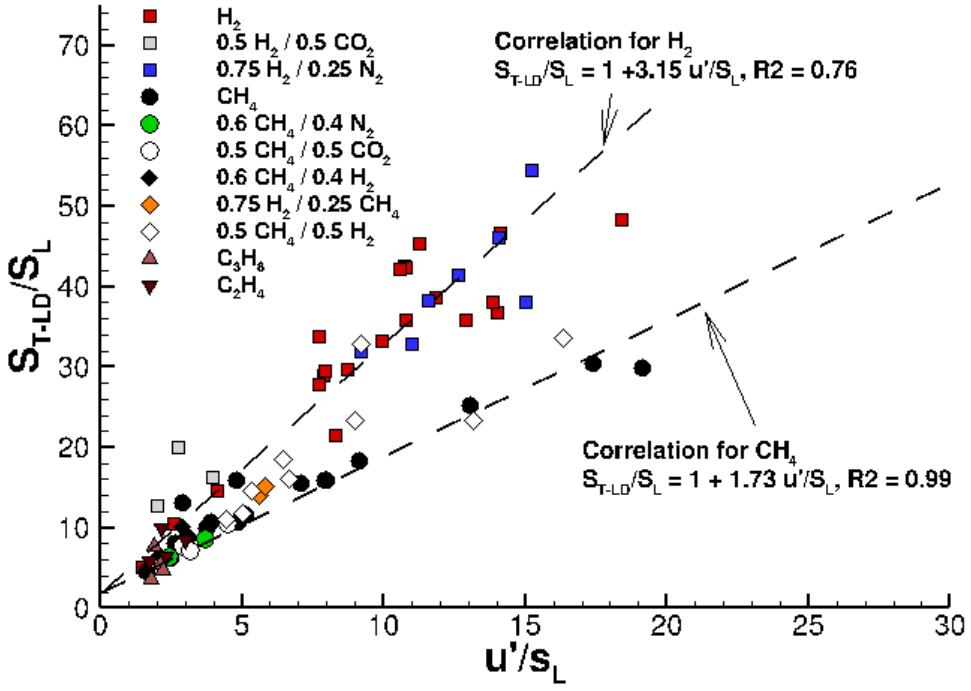

Figure 2.10: LSB Turbulent flame speed correlation for various fuel feedstocks [45]

Knowing the turbulent flame speed correlation, we can then manipulate Equation 2.14 with 2.15, with the result being the equation below.

$$1 + \frac{dU}{dx}\frac{(x_f - x_0)}{U_0} = \frac{S_{T-LD}}{U_0} = \frac{S_L}{U_0} + \frac{Ku'}{U_0} \tag{2.16}$$

Equation 2.16 was developed for the LSB by Robert K. Cheng as a simple analytical expression to relate the non-dimensional aerodynamic axial stretch rate, flame position, and virtual origin to the turbulent flame speed as a function of the laminar flame speed and turbulence intensity. What is very interesting to note is that for the LSBs previously tested across the works cited, at $U_0 > \approx 10$ m/s, all of the terms in the equation are constant. The exception being the S_L/U_0 which changes with stoichiometry. However, S_L is on the order of magnitude of 0.2 to 0.3 m/s for most hydrocarbon fuels and at moderately high ($U_0 > \approx 10$ m/s) this term becomes on the order of magnitude of O(0.01), whereas the far term on the RHS is on the order of magnitude (O)0.1. Only when pure hydrogen is burned at near stoichiometric conditions do the two terms become of the same order of magnitude. In this case, the flame shifts towards the burner outlet which is predicted by the equation.

Providing a little more background into the term on the far RHS of the equation which describes the normalized (by U_0) turbulence level of the flowfield. Even though experimental data has shown that turbulence decays linearly downstream from the centerplate (for grid based turbulence) [74, 75], this has not been observed in the LSB flowfield experimental data. The LSB shows near constant turbulence along the centerline which can be seen in Figure 2.11 where u' and v' are represented by the blue and red diamonds respectively. The fact that the turbulence does not decay indicates that the swirling flow of the LSB is likely influencing the centerplate flowfield.

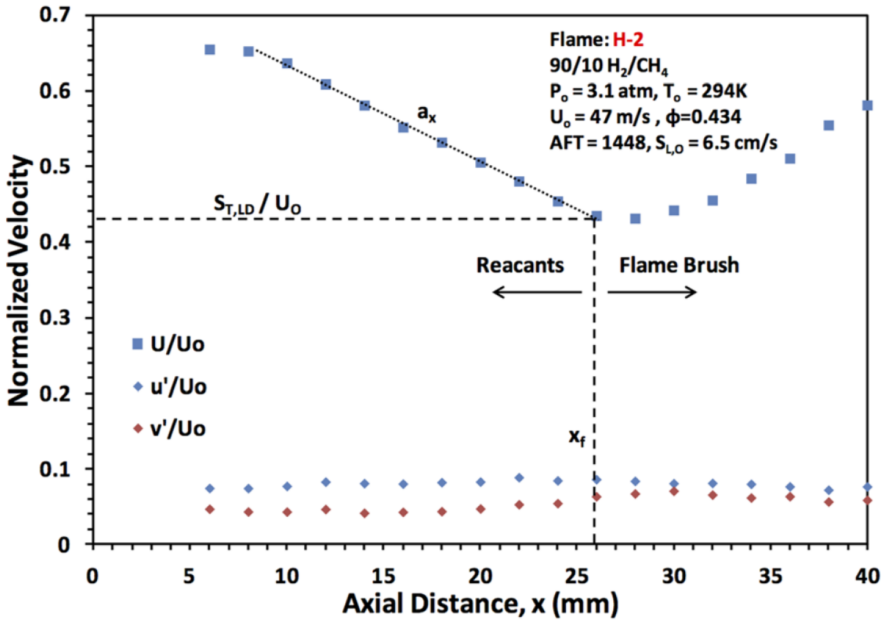

Figure 2.11: Centerline axial velocity profiles [48].

Focusing our attention to the left hand side (LHS) of the equation, the terms are predicting the location of the local velocity based on a linear decay from the highest velocity in the flowfield, U_0. As is the same on the RHS of the equation, the flame displacement (x_f - x_0) and axial divergence have little to no variation with changing load, fuels, and stoichiometry. The collapsing of the velocity profiles across a wide range of Reynolds numbers (calculated using burner diameter as the characteristic length) can be seen in Figure 2.12.

The collapsing of the centerline velocity profile and near constant flame displacement prove the existence of self-similarity in the nearfield of the LSB, which is a major finding. However, this self-similarity has only been shown to exist at modestly high U_0 on the larger LSBs tested in earlier studies. In one specific combined experimental and numerical investigation performed, a "developing" flow was observed in the experimental characterization of the flowfield, which resulted in the authors modeling only conditions with $U_0 > 10$ m/s [54]. The deduced parameters from the Particle Image Velocimetry (PIV) are shown in Figure 2.1 which show that at the 3, 6 and 10 m/s U_0 condition, the virtual origin position is not constant. The aerodynamic stretch rate, however, is nearly constant across all velocities.

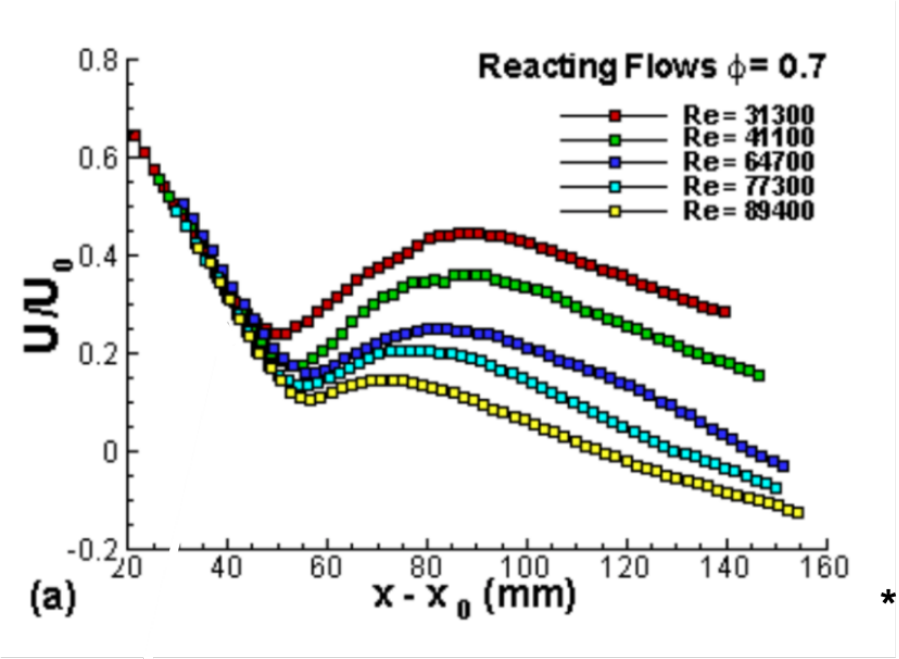

Figure 2.12: Normalized velocity profiles at the burner centerline across a range of Reynolds numbers [76].

U_0 (m/s)	x_0 (mm)	a_z (mm^{-1})
3	−48.4	−0.0075
6	−58.9	−0.008
10	−69.74	−0.0076
15	−81.4	−0.007
18	−81.4	−0.007

Table 2.1: Deduced flowfield parameters from centerline PIV data on 50 mm diameter LSB [54].

Additionally, the centerline profiles can be seen in Figure 2.13 where it is easily discernible that the lower velocities do not collapse onto a single curve and are not self-similar. However, all of the flowfields do show the typical characteristics of the LSB with a linearly decelerating axial velocity with flame generated acceleration at x_f. It can be noted that the location of flame can be seen shifting downstream at lower velocities (occurring at a higher displacement, x).

Even though all of the analysis up until this point has considered the existence of a flame, it is also possible to determine how the terms on the LHS of the equation change at various conditions. The flame changes a_x and x_0, however, observing and measuring the non-reacting flowfield also provides valuable insight and is performed in this dissertation. An example of how these values differ can be seen above in Figure 2.9.

One aspect of the flowfield that must be addressed is the manner in which the LSB is mounted and contained for experimentation and in real-world combustion systems.

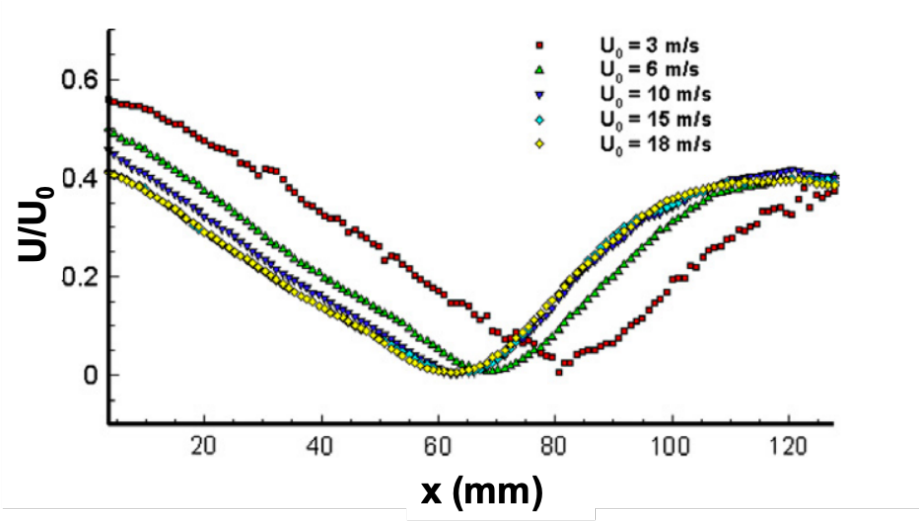

Figure 2.13: Centerline PIV data at varying U_0 for 50 mm diameter LSB [54].

During the initial LSB studies in the 1990s, the LSB was mounted in a nozzle and open to the room air because it was amenable to laser diagnostics. Later in the development of the LSB to determine its suitability for gas turbine applications, a study by Cheng and Littlejohn [50] was undertaken to determine the flowfield impact of mounting the LSB inside of an enclosure representing the combustor casing or walls. They used two different diameter quartz tubes and varied the bulk inlet velocities while measuring the flowfield using PIV. Their conclusion was that the nearfield was unchanged by the enclosure and all the LSB flowfield properties observed in the open still existed while enclosed. It was noted, however, that a recirculation zone downstream of the flame developed and was a function of the enclosure size. This type of large-scale recirculation zone can impact emissions and therefore is necessary to manage in commercial systems.

Similarly, a subsequent study determined that a portion of the acoustic signature of the LSB was due to the vortex shedding at the OSL which creates the ORZ that can be seen in Figure 2.7. In order to counteract this phenomenon, a divergent quarl structure was attached to the LSB nozzle which is essentially a "cone" with a specific angle. The resulting flame structure can be seen in Figure 2.14. The quarl acts as a physical guide to match the natural divergence of the flowfield and thus eliminates the sharp corners that would cause flow separation [77].

The addition of the quarl was a necessary step in order to allow the LSB to be adapted into a commercial product. The design of various quarls is included in this work as part of the microturbine combustor design in Chapter 4.

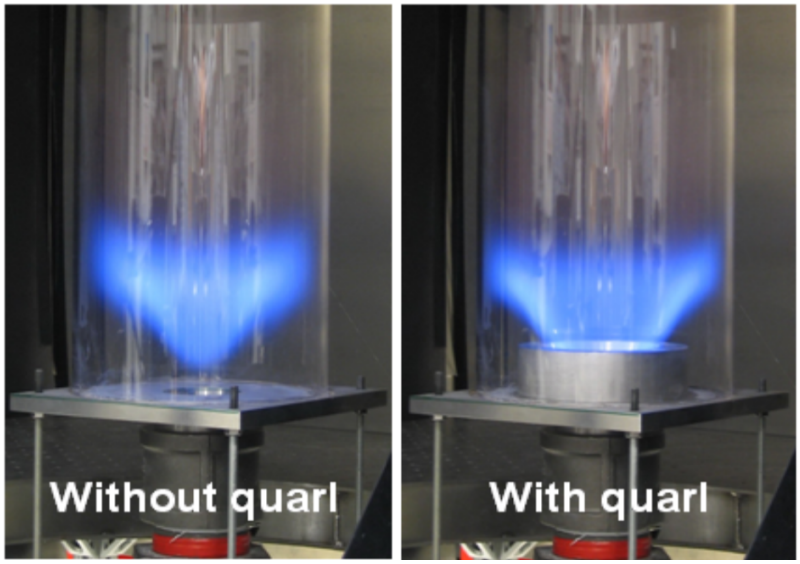

Figure 2.14: LSB flame with and without divergent quarl structure [77].

2.4.2 Unique LSB Properties

There are many aspects of the LSB that make it highly desirable for use in commercial applications. First, the ability of the burner to change bulk inlet velocities (load) without any changes in the flowfield properties (except at low U_0) enable a very high turndown ratio. This is important in many types of combustion systems from gas turbines to on-demand water heaters. Turndown ratios greater than 50:1 have been demonstrated in the laboratory [16].

Secondly, the ability of the burner to use a wide variety of fuel feedstocks due to the LSBs insensitivity to S_L is of great importance for a variety of systems. There have been many studies on the LSB with fuels ranging from biogas (CO_2 and CH_4) to 100% H_2 and all have followed the self-similarity discussed. Recently, there was a California Energy Commission (CEC) funded project performed by LBNL and University of California, Irvine (UCI) demonstrating real-time fuel switching between propane and biogas at a wastewater treatment facility in Rancho Santa Margarita, CA. Testing of the burner at LBNL and full scale testing at UCI revealed that emissions could easily be met as long as the adiabatic flame temperature, T_{AD} was maintained below a threshold value [78].

Third, the ultra low emissions that can be achieved by the LSB render it the perfect burner for current and future tightening emission regulations. In general, LP burners operating on gaseous fuels emit low levels of CO but struggle with NO_x emissions. As mentioned in the background section, NO_x emissions are a function of the time and temperature. Due to the lack of CRZ within the LSB flowfield, the products spend a considerably less amount of time at high temperatures compared to HSIs. Figure 2.15 shows the NO_x and CO emissions of a HSI compared to the LSB.

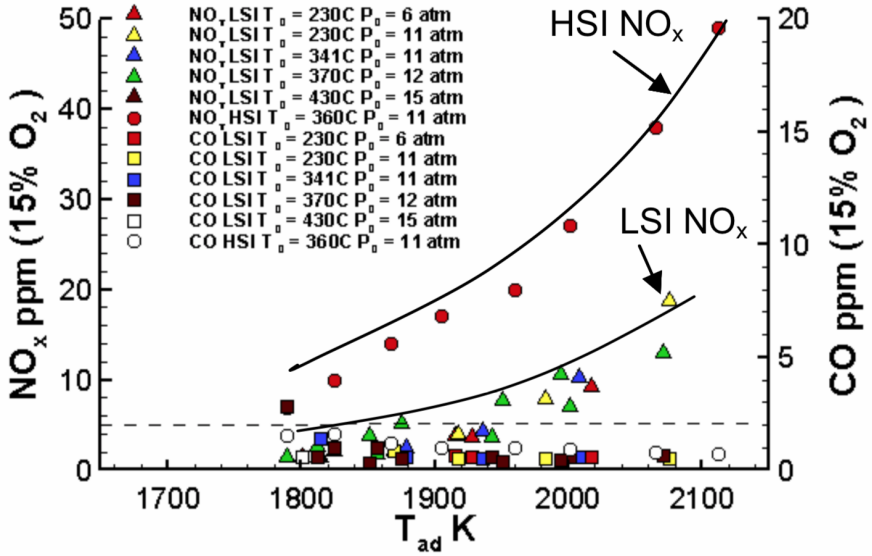

Figure 2.15: Comparison of HSI and LSB emissions of NO_x and CO [42].

2.4.3 Turbulent Flame Speed Definition and Importance

As previously discussed, the central hypothesis of the LSB is that the flame positions itself where the turbulent flame speed, S_T, matches the reactant velocity. This simple explanation provided the context to describe the self-similarity that was observed in the experimental studies and thus the importance of S_T is very clear. However, for many years, up until about the early 2000s, there were hundreds of studies that reported S_T, often with large discrepancies between them. The reason why this discrepancy exists is primarily due to the fact that flames studied in laboratories are assumed to be 1 dimensional (1-D) when in reality, a 1-D flame does not exist in any real-world burner. Furthermore, for most burners, the characteristics of the flowfield (for example, the size of the wrinkles) are dependent on the geometry of the device. What this means is that the measured S_T is specific only to a single burner with a specific dimension and will not translate to other types or sizes of burners. For example, a small diameter vs. a large diameter Bunsen flame will produce a different S_T. A visual image of how wrinkling, and therefore S_T can change with position in a Bunsen flame can be seen in Figure 2.16. In the case of a spherical flame, the degree of wrinkling changes with time as the flame propagates and expands into the volume.

In order to classify burner geometry into common groups to achieve consistent results, four definitions of premixed turbulent flames have been suggested by Cheng and Shepherd:

1. envelope flames: axisymmetric or 2-D Bunsen burners
2. oblique flames: V-flames
3. flat flames: low-swirl, counterflow, or diffusion burners

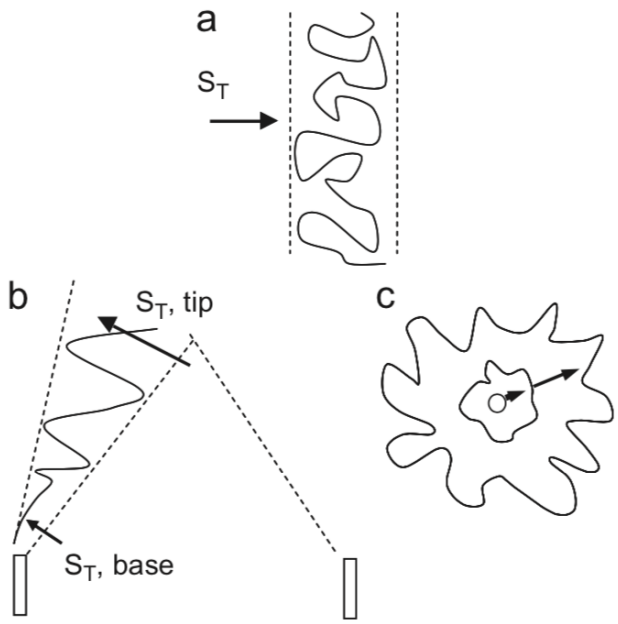

Figure 2.16: Schematic of (a) a hypothetical "geometry-independent" wrinkled flamlet structure and (b,c) realistic "geometry-dependent" wrinkled structures that cause the burning velocity S_T to depend on the distance (x) or the Bunsen geometry and time (t) for a spherical case [79].

4. spherical flames: fan-stirred chambers

Furthermore, and most important to the research presented in this dissertation, there are four unique definitions of how the S_T can be defined which depend on the specific type of flame configuration and the type of equipment used. The four types are [76, 79]:

1. $S_{T\text{-}GC}$, the global consumption speed $= \dfrac{\dot{m}}{\rho_R A_T}$
2. $S_{T\text{-}LC}$, the local consumption speed $= S_L I_0 \displaystyle\int_{-\infty}^{\infty} \Sigma d\eta$
3. $S_{T\text{-}LD}$, the local displacement speed $= (V_{flame} - V_{gas}) \cdot n_{LE}$
4. $S_{T\text{-}GD}$, the global displacement speed $= \dfrac{\partial r_f}{\partial t} - V_{gas}$

Now, it is very pertinent to note that these four definitions are not expected to provide the same results. They are only equal if a true 1-D flame exists, which is not possible. For a burner, the definition of S_T utilized will depend on the type of burner and available measurement diagnostics. For example, in the case of a Bunsen flame, the most appropriate definition would be $S_{T\text{-}GC}$ because the mass flow into the

device can be measured. Since all of the fuel is consumed, the flow rate of fuel can be used to determine the burning rate. In the case of the LSB, this measurement would not be acceptable because all of the fuel is not burned (some may escape around the flame in the open) and therefore the global consumption rate cannot be measured.

There are types of burner configurations that fit into each of the categories above, but for the purpose of brevity, only information relevant to the LSB will be discussed further. For the LSB, two turbulent displacement speeds can be determined, $S_{T\text{-}LD}$ and $S_{T\text{-}LC}$. The local consumption speed can be determined by measuring the flame surface density Σ through the use of laser diagnostics. This type of diagnostic was tested by Shepherd and Cheng [37] for the LSB and found to be quite different (by a factor of 2-3) than the local displacement flame speed. The exact cause of this difference is not completely understood because it could not be measured directly. It is postulated that a large source of this difference is due to the divergence in the flowfield causing the areas between the leading and trailing edges of the flame to be different. The local displacement uses the leading edge of the flame front to determine a velocity whereas the consumption used a location of a specified reaction progress variable, $c = 0.5$, thereby using a different area or position within the flame front for each calculation. However, later studies have attempted to minimize the divergence in the flowfield and still saw differences in the two values, leading to the belief that there could be other factors not fully understood [79].

In this dissertation, the local displacement turbulent burning velocity is deduced and reported. This measurement is fairly straightforward if the flame position and velocity field are known. As seen by the definition above, $S_{T\text{-}LD}$ is a function of the local reactant and flame velocity propagating normal to the flame front. In the case of the LSB, the flame is stationary and normal to the approach flow, so the reactant velocity at the leading edge of the flame front is therefore $S_{T\text{-}LD}$. Using laser diagnostics discussed in Chapter 3, the velocities can be measured to determine $S_{T\text{-}LD}$ over any range of conditions.

2.5 Open Questions and Research Area

The review of previous LSB studies notes the lack of data using swirlers smaller than 1.5" (38 mm) in diameter. There were two studies performed prior to this dissertation using small-scale LSBs. One by Strakey [68] used a 15.8 mm LSB, however, the purpose of this paper was to validate a numerical model and therefore there is little published information on the flowfield. The second study utilized a 1" LSB but did not report any flowfield results because the scope was only to understand the thermoacoustic coupling mechanism of LSB.

The remainder of the experimental and numerical developments prior to this dissertation have inlet Reynolds numbers (Re) greater than 40,000 where self-similarity has been shown to exist. This low Re regime is where this dissertation seeks to explore which can be seen in Figure 2.17. In this plot, three types of LSBs are shown, commercial burners operating at ambient temperature and pressure, gas turbine applications with elevated temperature and pressure, and lastly the liquid fueled gas

turbine application at elevated temperature and pressure. The 1" studies previously mentioned are not included in this plot as the data obtained was very limited in scope. The regime explored in this dissertation is indicated by the shaded region, representing smaller scales over a range of a range of bulk inlet velocities.

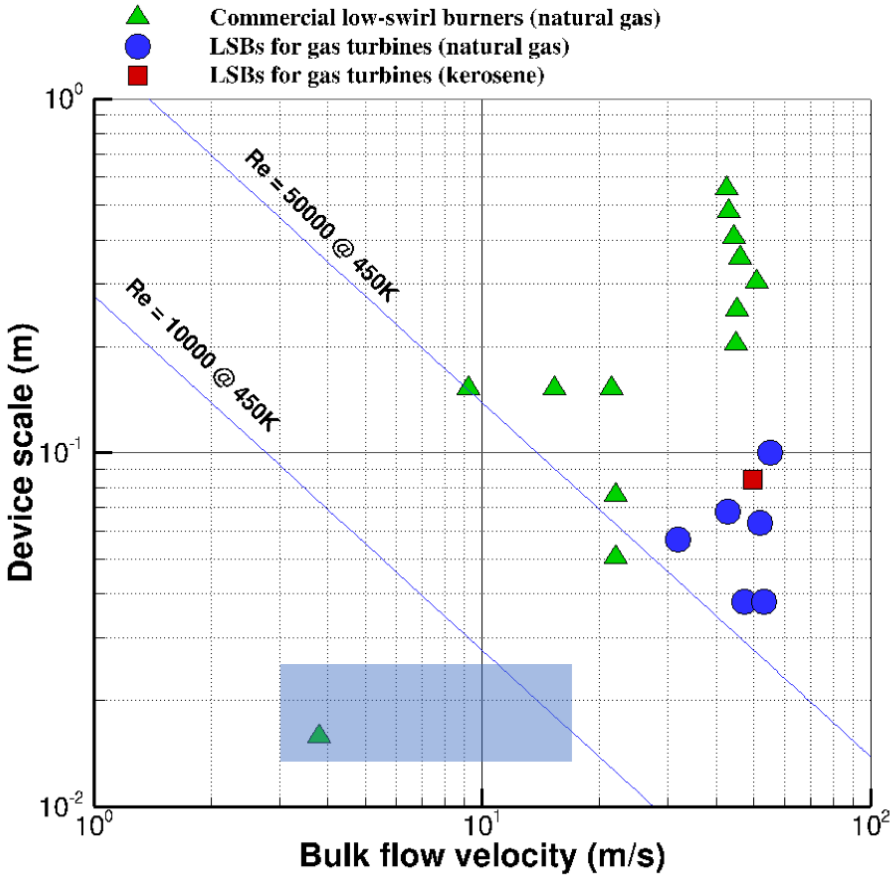

Figure 2.17: LSB regime diagram of device bulk inlet velocity vs device scale for all previous LSB developments. The work in this dissertation is the region contained in the shaded box.

At this point, a number of hypotheses were formulated about the operation about the miniaturized LSBs. First, it was suspected that small-scale LSBs would stabilize a flame and exhibit the same performance characteristics of large-scale LSBs in terms of emissions, flashback, and lean blowoff. Secondly, it was expected that scaling might impact the terms in Equation 2.16, however, self-similarity at a range of conditions would hold, similar to their large-scale counterparts.

The following questions were developed from these hypotheses to help direct the path of the research:

- Will a miniaturized LSB (< 1") be able to stabilize a flame?
- If a miniaturized LSB does stabilize a flame, will it exhibit the same operational

characteristics (LBO, pollutant emissions, flashback) as the larger scale LSBs have demonstrated?

- Is the LSB a suitable combustion technology for the future of downscaled energy systems?
- Does the miniaturized LSB produce similar flowfield characteristics (divergence, virtual origin, turbulent flame speed, flame position) as its larger scale counterparts?
- How does the laminar-to-transitional flow regime impact the LSB?
- Do the miniaturized LSBs exhibit the same self-similar behavior that is seen in larger LSBs at similar conditions?

The research presented in this dissertation will seek to answer these questions to shed light on the hypotheses above. The following chapter will discuss the experimental approach and setup to answer these questions. Chapter 4 delves into the experimental results of the miniaturized LSB performance and the interrogation of the flowfield. Chapter 5 discusses the conclusions from this work as well as possible future studies.

Chapter 3

Approach and Experimental Setup

The current chapter has two sections, the first discusses the approach to answer the questions that were presented in Chapter 2. The second part of the chapter details the experimental setup used to acquire the data to answer these questions.

3.1 Approach

The knowledge gap discussed in the prior chapter shows the lack of performance data for small-scale LSBs. It is of interest to develop and understand whether the LSB is an appropriate combustion technology for future downsized energy systems. Additionally, it is necessary to develop an understanding of the flowfield evolution for the miniaturized LSBs. In order to achieve these tasks, the following objectives must be met:

1. **Perform literature review of all LSB studies to understand the flowfield and operational characteristics that have been exhibited.**
2. **Design and manufacture hardware to measure the flowfield properties as well as operational characteristics of the downscaled LSB hardware.**
3. **Conduct experiments to determine applicability of the LSB to small-scale energy systems.**
4. **Collect data to test whether the flowfield exhibits self-similar behavior.**
5. **Analyze data and provide insight into the effects of scaling on the LSB.**

The details of these topics will now be discussed in detail.

1. ***Perform literature review of all LSB studies to understand the flowfield and operational characteristics that have been exhibited.***

In order to fully understand the background and governing equations of the LSB, a full literature search was performed and was detailed in Chapter 2. This was also necessary to understand the gaps in knowledge that exist.

2. ***Design and manufacture hardware to measure the flowfield properties as well as operational characteristics of the downscaled LSB hardware.***

There are two separate tasks that must be performed as part of the effort to understand the miniaturized LSB, one being to determine the feasibility of the LSB for small-scale combustion systems, and the second being to develop an understanding of the flowfield evolution. In order to achieve these goals, various LSB geometries were considered in order to balance the goals for each task which were quite different. In the case of the microturbine application, a parametric study of the LSB geometry must be performed in order to optimize LBO, pressure drop, emissions performance, while minimizing flashback. In the flowfield investigation portion of this work, visual access to the flame in the open air across a wide range of velocities and equivalence ratios will allow the collection of sufficient data.

For the two studies in this dissertation, the experimental setup and instrumentation required was carefully considered. In the case of the feasibility study, the ability to measure exhaust emissions, pressures across the combustor, LBO, while also providing visual access to the flame were the most important aspects. In the PIV setup, the primary consideration was focused on obtaining appropriate particle seeding for the miniaturized LSB across a range of velocities. In almost all experimental studies, only a very small range of operating conditions are studied whereas in this dissertation, a wide range of velocities and equivalence ratios were studied. This wide range requires very careful consideration in the selection of devices to measure the flow rates of fuel and air. Lastly, in order to measure the flame position, a system must be designed and constructed.

3. ***Conduct experiments to determine applicability of the LSB to small-scale energy systems.***

The initial studies of the miniaturized LSB were targeted for a specific application, a microturbine combustor for the GENSETS program. Considering the targets, multiple configurations with varying levels of instrumentation will be performed. After, experiments will be conducted to determine the feasibility of using the LSB in this application.

4. ***Collect data to test whether the flowfield exhibits self-similar behavior.***

In order to characterize the flowfield and determine if self-similarity holds, multiple LSB sizes were utilized across a range of velocity and equivalence ratios. Experiments were conducted using PIV to measure the flowfield properties along the centerline. In order to determine the flame position, non-refractory oil was used as a flame front marker where the flowfield properties could be extracted from the PIV results.

5. ***Analyze data and provide insight into the effects of scaling on the LSB.***

After data collection, the flame position and PIV data were analyzed to determine the effects of scale on the flowfield properties of the miniaturized LSBs. This was performed by post processing the flowfield data using various techniques to determine correlations and trends that exist as a function of scale. Results will be shown which detail whether the LSB is an acceptable device for future miniaturized combustion systems.

3.2 Experimental Setup

This chapter will discuss the LSB swirler and centerplate design, the experimental setup design, and considerations for accurate data collection.

3.2.1 LSB Design

Swirler Design

At the start of this study, it was unclear whether the LSB could stabilize a flame at scales smaller than ever previously explored. This started with using the best available swirler that had been developed previously. The geometry utilized was created by Therkelsen et al. [70] in cooperation with NETL which showed that the curved vane (CV) swirler was the most optimal design, offering the best LBO with the lowest pressure drop. The CV swirler used for this study had an $\alpha = 37$ degrees, R = 0.605, and 16 vanes in order to provide the most axisymmetric flowfield possible. In previous studies with fewer number of vanes, asymmetry in the flowfield was noted and special care had to be taken to ensure alignment of the swirler and perforated plate holes in order to provide results consistent with other studies [55]. By using a swirler with 16 vanes, this asymmetry was minimized.

Hardware development started with creating various geometries and finding vendors that could manufacture the swirlers. Since conventional machining is expensive and complicated due to the geometry configurations, 3-D printing was chosen to be the best option. Initially, the swirlers were printed by stereolithography apparatus (SLA) in polycarbonate material. Due to the fact that the LSB produces a lifted flame, all swirlers could be made of low temperature plastic to reduce part cost and lead time, rather than printing in metal. However, during operation of the LSBs, careful operation was necessary as a single flashback event would melt the swirler.

The swirlers were printed with diameters, D, ranging from 12 mm to 26 mm in 1 mm increments. Swirlers as small as 8 mm in diameter were designed, however, the smallest that was printable by any vendor was the 12 mm diameter unit. This was due to the very thin tip of the swirl vanes falling below the minimum part thickness the SLA can produce. Even if they were successfully printed, the vane tips would break off during the part extraction from the machine and support.

In parallel with the SLA manufacturing, swirlers were also printed using direct metal laser sintering (DMLS) from multiple vendors. Similar to SLA, the quality and consistency of parts produced varies widely between vendors but the surface roughness or misshapen parts is more easily seen in metal parts compared to plastic components. For printing the LSBs, it was found that a single machine manufactured by 3D Systems, the ProX320, was able to produce parts of this scale. This is due to the fact that the laser beam used to melt the metal powder to form the geometry is smaller than other machines, measuring 0.080 mm, whereas other manufacturers such as EOS have a beam thickness of 0.10 mm or greater. The swirlers were printed in various materials ranging from titanium (Ti64) to nickel superalloys (inconel 718). Being able to reliably produce swirlers in both plastic and metal is very important to the viability of small-scale LSBs.

Centerplate Design

After the swirler geometry was determined, the centerplate could then be optimized based on the data and knowledge from previous studies. Initially, in order to focus on a single LSB swirler and centerplate before moving to multiple sizes, a single swirler was chosen as a starting point. This swirler was intended to meet the GENSETS targets for a CHP microturbine with an electrical output of 1 kW. The heat output from the combustor, however, was required to be 3.33 kW using natural gas which considered a microturbine efficiency of 30%.

Additionally, the combustor must be able to meet the target pressure drop, achieve the emissions targets, and show no signs of flashback at the operating condition. In order to obtain low NO_x emissions, a sufficiently lean mixture had to be chosen. Based on the LSB data, the target operating condition was $\phi = 0.65$ which therefore determined the total mass flow rates of air and fuel into the LSB. Initially a target $U_0 \approx 9$ m/s was chosen based on the previous operational characteristics of LSBs.

Based on these parameters, a swirler diameter of 14 mm was chosen for the initial experimental studies to determine if this small-scale LSB could stabilize a flame. Multiple centerplates were designed in Autodesk® Fusion 360™ with varying open areas ranging from 25% to 32%. In order to save time and reduce cost, the centerplates were printed in polycarbonate material, however, after testing various configurations, it became clear that the flame was very sensitive to the LSB centerplate geometry and 3-D printing could not produce consistent results due to its large tolerance of finished parts. Centerplates were therefore only manufactured using conventional CNC machining in the machine shop at LBNL using grade 316 stainless steel.

Swirler and Centerplate Optimization

The 14 mm LSB and mounted centerplates were initially tested considering three parameters; flame liftoff position, x_f, LBO, and the flame shape. Two of these parameters, x_f and flame shape are deduced by visual inspection and require a trained eye. Under the guidance of Dr. Robert K. Cheng, the centerplates were tested at the target condition for the GENSETS application and aluminum tape was used to cover

holes in specific locations to achieve the desired "bowl-shape" flame that is typical of the larger-scale LSBs. The first set of centerplates contained full circles of holes and the flame, while stable, appeared to be "indented" in the center region meaning that the center core region was burning further downstream of the areas around it. This flame shape means that the local velocity is too high near the center and too low in the surrounding circumference which leads to poor LBO and flashback performance. By blocking selected holes in the center, the flow is decelerated locally and the desired flame shape was ultimately achieved.

Simultaneously, the flame liftoff distance, x_f, was optimized by testing centerplates of varying hole diameters (open areas). The open area of the centerplate changes the swirl number, S, and influences x_f. A higher open area allows more flow to pass through the center channel resulting in less flow passing through the swirling region, decreasing S. The higher the swirl number, the closer the flame will move towards the burner nozzle exit and vice versa. If the flame liftoff distance is too high, meaning that the flame is too far downstream, LBO will occur at too high of a ϕ whereas if the flame is too close to the burner exit, flashback is more likely to occur. Through visual inspection, this distance can be optimized based on experience but can also be measured with laser diagnostics which will be discussed in the results section. The final geometry can be seen in Figure 3.1.

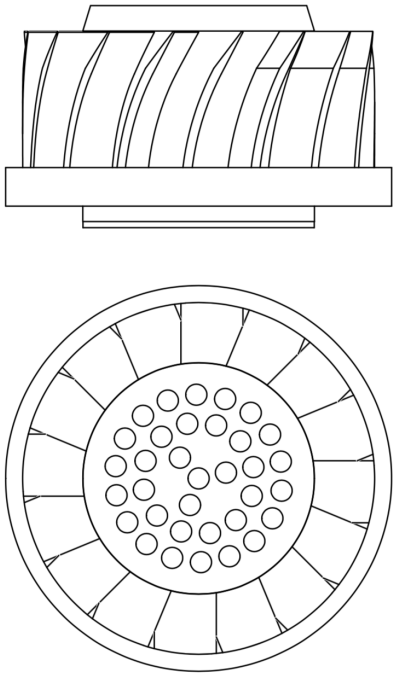

Figure 3.1: Side view and bottom view of the GENSETS LSB 14 mm diameter LSB with centerplate

In some of the earlier LSB developments, individual hole sizes were varied to achieve the proper flame shape but in order to simplify the design, the three holes around the center were deleted, allowing for easier manufacturing and identification.

The centerplate that was used for the GENSETS application features 34 equally-spaced holes each with a radius of 0.386 mm which results in an open area of 28.2%. The 3-D printed metal and plastic swirlers with centerplates are shown in Figure 3.2.

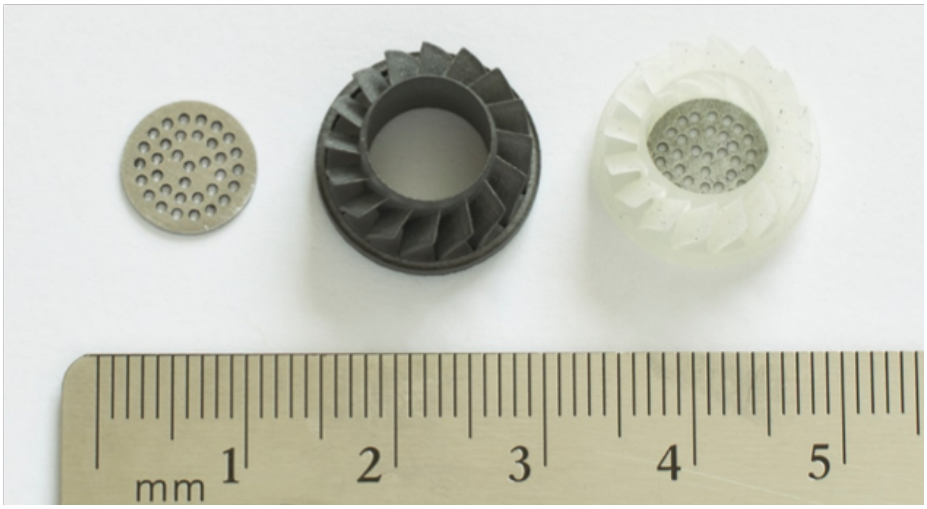

Figure 3.2: GENSETS 14 mm diameter swirler and centerplate geometry. From left to right; stainless steel center plate with 34 holes, 37 degree-16 vane titanium swirler, 16 vane polycarbonate swirler with attached centerplate.

The swirl number of the GENSETS LSB were measured by blocking the centerplate and swirler separately and measuring the pressure drop which can then be used to calculate the mass flux through each channel by using the Bernoulli equation. By then using the geometric properties of the LSB, the swirl number was calculated to be 0.54, within the expected range of the previous LSBs.

The geometry shown in Figure 3.2 was used for all of the gas turbine combustor development and testing. However, after initial PIV testing, it became clear that the centerplate needed to be modified to have a higher flame liftoff distance. The full details and investigation into the flowfield will be presented in Chapter 4. In order to increase the liftoff distance, the open area of the centerplates was increased to 30% (up 1.8%) from the centerplates shown in Figure 3.2. This modification would affect the performance of the LSB slightly by increasing the ϕ at which LBO occurs, however, for successful interrogation of the flowfield, this was a necessary modification.

In order to determine the impacts of scale on the flowfield development, of the swirlers manufactured, 3 diameters were tested, 12 mm, 14 mm, and a 25.4 mm, all with 30% open area centerplates. The diameters were chosen because they span the smallest LSB that could be manufactured (12 mm) up to the size of the LSBs previously tested (25.4 mm). The 3 swirlers were printed in Ti64 and are shown with their attached stainless steel centerplates in Figure 3.3.

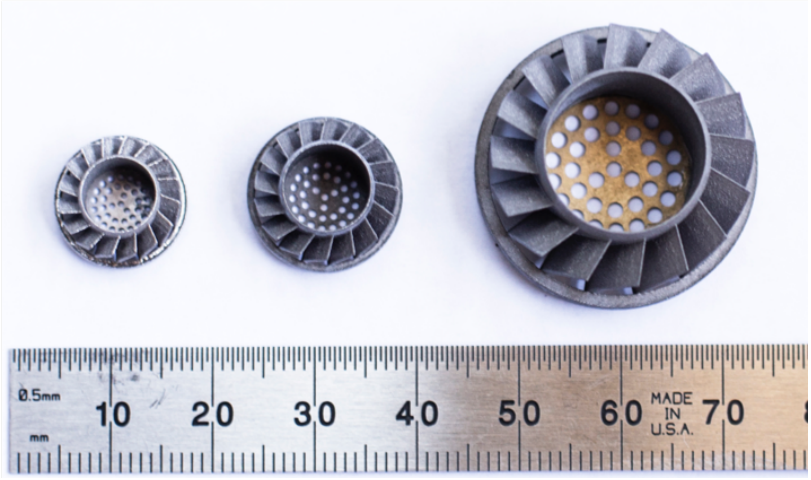

Figure 3.3: 16-vane, 37-degree titanium swirlers with attached 30 degree center plates for the experimental flowfield interrogation. From left to right, 12 mm, 14 mm, and 25.4 mm diameter swirlers.

3.2.2 PIV and Flame Position Experimental Setup

The atmospheric pressure test rig is located at Lawrence Berkeley National Laboratory in Berkeley, CA. When setting up the experiment in order to test the LSB performance characteristics (emissions, pressure drop, and LBO), many options and configurations were considered and are discussed below.

LSB mounting Configuration

In order to test the three LSBs with different diameters in a consistent manner, swirler mounts were manufactured to capture each LSB. Each holder attaches to the plenum shown below in Figure 3.4.

In this image, a 1" swirler mount is shown and a lip extends to directly meet the swirler. In the case of the smaller LSB mounts, they are inserted into the plenum exit and secured with three mounting screws. The mounts all have the swirler recess distance, L, equal to 1*D and each swirler is an interference fit into the holder.

The interior of the plenum has a contoured wall that expands from a 4 inch diameter at the base down to a 1 inch diameter at the top. The fuel and air are premixed upstream (below the bottom of the picture) and proper mixing is ensured by having a 3 inch thick layer of marbles that is contained and captured by a screen. In this design, there is no flame arrester as small-diameter screens are easily clogged with particle PIV seed.

Fuel and Air Controls

The fuel and air circuits of the experimental setup are straightforward. The fuel was provided by bottled 99.0% pure methane in K-size cylinders with a regulator providing 35 psia to the mass flow controllers (MFC). The mass flow rate was controlled by

Figure 3.4: Contoured wall plenum with 1" swirler mount shown on top in lighter stainless steel material.

Brooks® GF40 series MFCs of varying sizes. Due to the wide range of fuel flow rates, either of two GF40 MFCs were used depending on the velocity range and size of the burner being tested and the combustion air was provided by house air plumbed to the setup and reduced to 40 psi to supply the Brooks® model 5853 MFC. The details of the MFCs and flow ranges used for each set of conditions are shown in Table 3.1. Additionally, a fuel cutoff solenoid valve was attached after the fuel regulator and in case of emergency, the fuel could be shut off quickly by a switch mounted at the control computer.

Fluid Measurement	**MFC Name**	**Flow Range (SLPM)**
Methane	GF40 - 15	0 - 14
Methane	GF40 - 40	12 - 44
Air	5853E	14 - 600

Table 3.1: Mass flow controllers for experimental testing of the LSBs

Furthermore, all MFCs were calibrated at the start of this study by the manufacturer and were frequently checked for consistent flow rates over the duration of

the entire study. These checks were performed by measuring LBO at pre-defined set points for the same two LSBs. Any deviation greater than 0.03 would result in a discontinuation in use of that unit.

The experimental setup was controlled by a Dell OptiPlex model 9020 computer located adjacent to the experimental setup. The data acquisition (DAQ) hardware was controlled by an in-house Python graphical user interface (GUI) developed by Gary Hubbard which can be seen in Figure 3.5. This software uses National Instruments (NI) hardware to communicate with the MFCs in the form of analog signals that provide real-time control of the inputs and outputs of the system. There are two methods in which the MFCs can be controlled, either by setting a bulk inlet velocity and equivalence ratio or by manually entering the desired air and fuel flow rates. Logging of the inputs and outputs, including emissions can all be accomplished using this software.

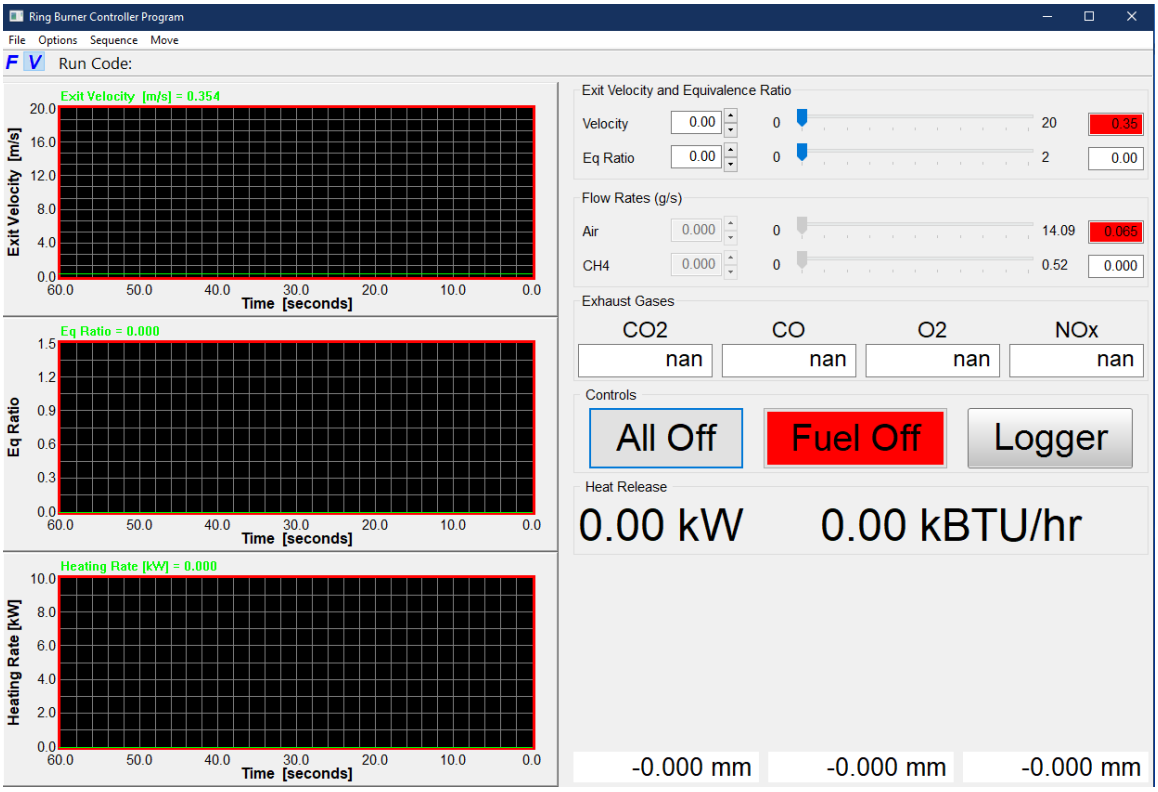

Figure 3.5: Burner control GUI in velocity control mode.

Emissions Measurement

The emissions measurement was accomplished by using a purpose-built emissions cart that contains two analyzers, an ice water sample bath, a power supply, a zero air generator (ZAG), and a vacuum pump to pull the sample. The cart contains two analyzers, one being a California Analytical Instruments (CAI) model 602P which measures CO_2, and CO using a non-dispersive infrared (NDIR) sensors and O_2 using

a paramagnetic sensor. The second analyzer is a CAI model 600 CLD which uses chemiluminescence to measure NO_x. Separately, during the infrequent measurement of total hydrocarbon (THC) emissions, a Horiba® FIA-510 FID analyzer was utilized. During measurement, the lowest range possible was used in order to ensure the most accurate value. All ranges for the analyzers were calibrated using bottle gases with multiple ranges and zeroed using nitrogen gas before the start of any emissions measurements.

Measurement of emissions were only performed with the flame enclosed by a quartz tube with the emissions probe inserted approximately one inch into the quartz tube. The emissions probe consisted of a bent section of 1/4" stainless steel tube connected to high temperature plastic tubing which then passes through an ice water bath in the emissions cart in order to condense and remove water from the sample. The sample is then split between the analyzers where it is sampled. In order to reduce the delay time between the sample probe in the quartz tube and the analyzer (a distance of approximately 6 feet), a vacuum pump with a high flow rate is used to pull the gases after which a portion is vented externally to the exhaust hood.

PIV System

The PIV system consists of many components including a laser, optics to shape the laser beam into a sheet, a computer to control the laser triggering and capture images, software to process and capture the images, a camera, and a cyclone particle seeder which entrains seed into the flow. The overall system layout is shown in Figure 3.6 and the details of the components will be discussed in more detail below.

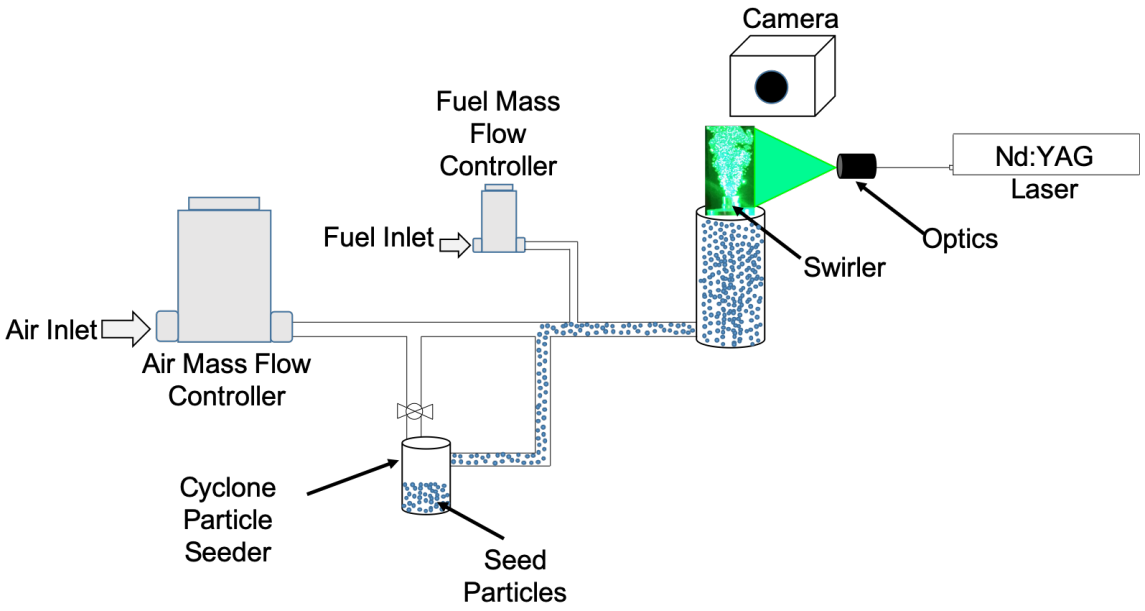

Figure 3.6: Schematic of the PIV burner experimental setup.

First, the laser utilized is a New-Wave Solo Nd:Yag laser with double 120 mJ

pulses at a wavelength of 532 nm. The optics shape the laser beam into an approximately 1 mm thick sheet which slices through the centerline of the LSB flowfield. An representation of the imaged region is shown in Figure 3.7 and is approximately 5 cm by 5 cm.

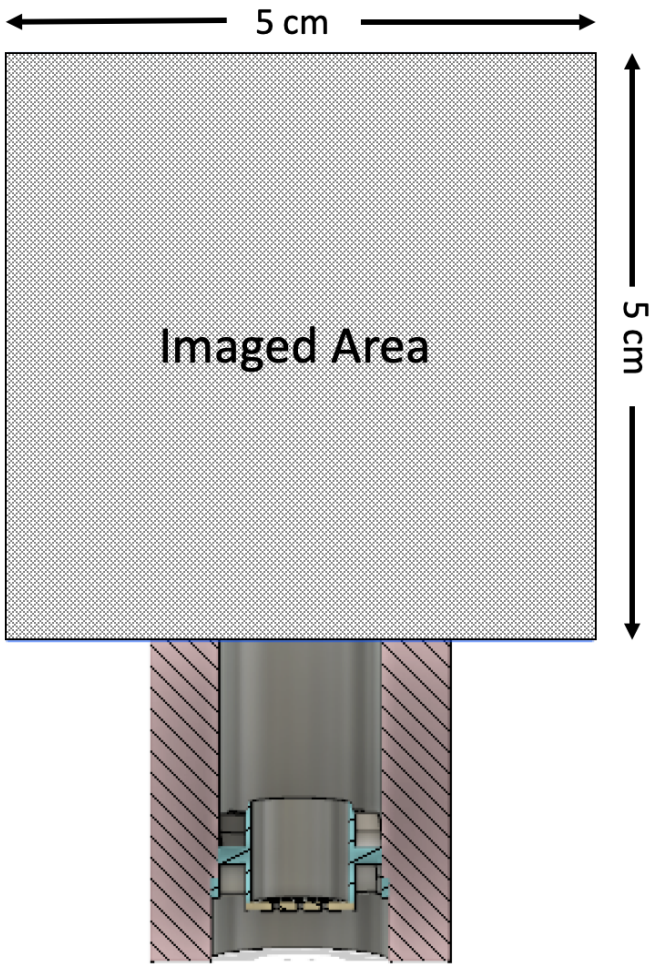

Figure 3.7: Cross section of the 14 mm LSB with the shaded region representing the camera viewing region.

The digital camera is a Kodak/Redlake model ES 4.0 that has a 2048 x 2048 pixel resolution that covers both the nearfield and the farfield of the flame with a 0.025 mm/pixel resolution. The camera lens utilized is a Nikon UV-105, 105 mm multispectral imaging lens set to a f-stop of 4.5 to ensure clear and focused images. Additionally, the laser and camera are operated in the so-called "flame straddling" mode during the acquisition meaning that short inter-frame times are used to capture the image pairs.

The PIV computer used to interface with the laser and camera is separate from the Dell computer that controls the MFCs and records data. The QES PIV computer runs a program developed and supplied by Mark Wernet at NASA [80], PIVPROC, which controls the triggering of laser and the capturing and saving of the images. An

additional program, PIVAVG, processes the image pairs, deduces individual vector fields and then averages all of the vector fields into a single file with all flowfield statistics. For all of the studies in this dissertation, 350 image pairs were recorded for each condition.

Before the start of data collection for this dissertation, multiple sensitivity studies were performed to understand the impact of specific parameters on the flowfield results. More specifically, the centerline velocity, u' and v' were probed since they are the parameters that are primary studied in this work. One such study was to determine the minimum number of image pairs to produce a statistically stable result. In order perform this test, multiple sets of image pairs were taken ranging from 200 to 600 on the 12 mm and 25.4 mm LSBs shown above at a U_0 of 3 and 18 m/s, covering the entire range of intended operation. It was found that obtaining more than 300 image pairs would produce a statistically stable result with deviations in centerline velocity, u', and v' less than 5% of the highest number of images, 600.

The second sensitivity study was performed to optimize the subregion processing size in the cross-correlation method used to develop vectors from the image pairs. There are a variety of region processing size options that are available in the PIVPROC software that can be utilized to provide the most representative set of vectors from the images. These tests are done by loading individual image pairs and visualizing the resulting vectors from that set of images. For all the LSBs tested in this work, subregion sizes of 128 x 128 pixels with 25% overlap were used to ensure that the vector field was accurately captured.

The third study performed aimed to optimize the inter-frame time between the image pairs taken during the frame-straddling mode. The inter-frame time needs to be small for two reasons, first to minimize the number of particles that leave the plane of view (due to the swirling flow) between the image pairs and secondly, the particles should only travel a certain number of pixels in order to track them accurately. Obviously, the bulk inlet velocity affects the particle displacement so the full range of conditions had to be considered. This distance is governed by the "1/4 rule" which states that the particle should not move more than 1/4 of the subregion size [81].

Another portion of the PIV system that required a great deal of consideration was the design and operation of the particle seeder system which was not optimized for using the small flow rate of air utilized in this dissertation. A cyclone feeder system was used with an angled seed swirling system that was held in a single position. In order to adjust for the low flow rates of the small-scale LSBs, the air supply was diverted into two streams, one which directly enters the air plenum, bypassing the seeder, and the second stream is plumbed into the seeder. Both of these streams have ball valves to control the flow rate of air entering the seeder. At low velocities on all of the LSBs, 100% of the air enters the seeder and at higher velocities, only a small portion enters the seeder. The positions of these two valves is manually adjusted while lasing to the desired seeding density and then data is collected. The seeding density is set moderately high and within the guideline of number of particles per pixel [81].

The seeding particles used were Aerosil® fumed silica particles. The use of these

particles have a high refractive index that are easily viewed by the PIV system. The particles have a mean diameter of approximately 12 nm [82] and by using the Basset Equation and the analysis provided in [83], the frequency response that the particles can track is up to 10,000 Hz.

The Aerosil® particles track the flowfield well but the small swirlers were shown to be very prone to buildup of particles which can be seen in Figure 3.8.

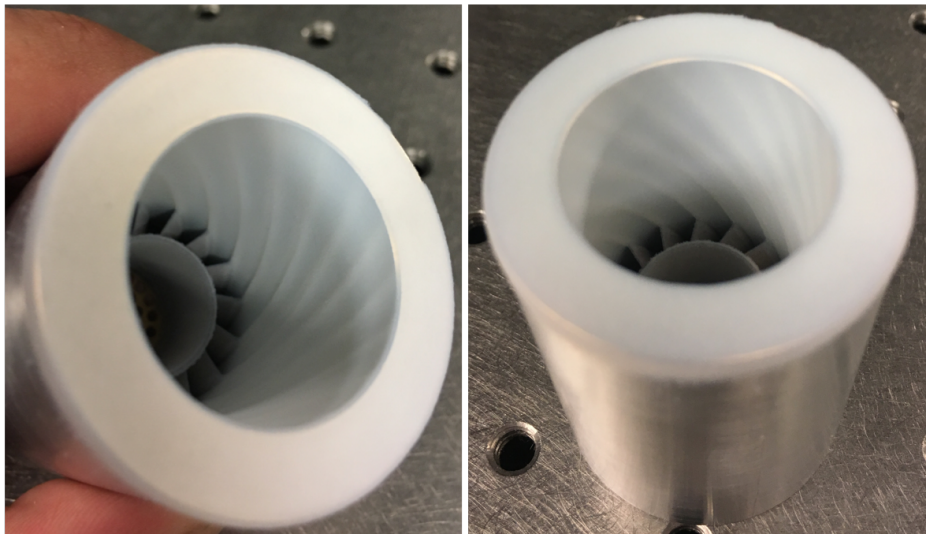

Figure 3.8: 25.4 mm LSB after about 5 minutes of running showing buildup of aerosil® on the swirler and walls of swirler mount

As a result, in order to ensure the most accurate results, the flow was stopped after each data set was collected which represented approximately 3 minutes of flow time. A compressed air nozzle was then used to blow out the swirler and centerplate to ensure no buildup was present. This was repeated for every set of data to ensure accurate and consistent data collection.

In addition to the clogging of the swirlers and centerplates, the plenum would clog as well and disrupt the uniformity of the flowfield. An example of which can be seen in Figure 3.9 and as a result, the plenum was disassembled and cleaned with soap and water after every 45 minutes of total run time on the system. In addition to physically checking the system, centerline data was also periodically compared on the same hardware running the same conditions to ensure consistency of the results.

3.2.3 Flame Position Measurement

In order to measure the position of the flame front, x_f, a system was devised to capture individual flame images, determine a flame front location, and obtain a probability density function for each condition. Ideally, the flame front position would have been captured with a planar laser-induced fluorescence (PLIF) technique similar to what has been done in many of the previous works [36, 38, 54, 64, 68]. However, the equipment needed to perform this experiment was not available at LBNL so a new system was devised.

Figure 3.9: Contoured wall plenum with seeder material buildup on both halves. The swirler is mounted at the end of the bottom figure

The same experimental setup shown in Figure 3.6 was used, except the flow was seeded with non-refractory particles instead of Aerosil®. In this case, silicon oil from Sigma-Aldrich which vaporizes in the flame front was used so that the flame location can be visualized. The raw images that the silicon oil produces can be seen in Figure 3.10.

The silicon oil could not be used to determine the flowfield vectors as the seeding density is too high to be used for the PIV data acquisition so the silicon oil was used to capture only the flame front location and the Aerosil® was used to determine the velocity data.

At first, it was necessary to ensure that silicon oil would provide equivalent results to the previous studies. This was accomplished by examining the previous studies performed which required the visualization of the leading edge (LE) of the flame front.

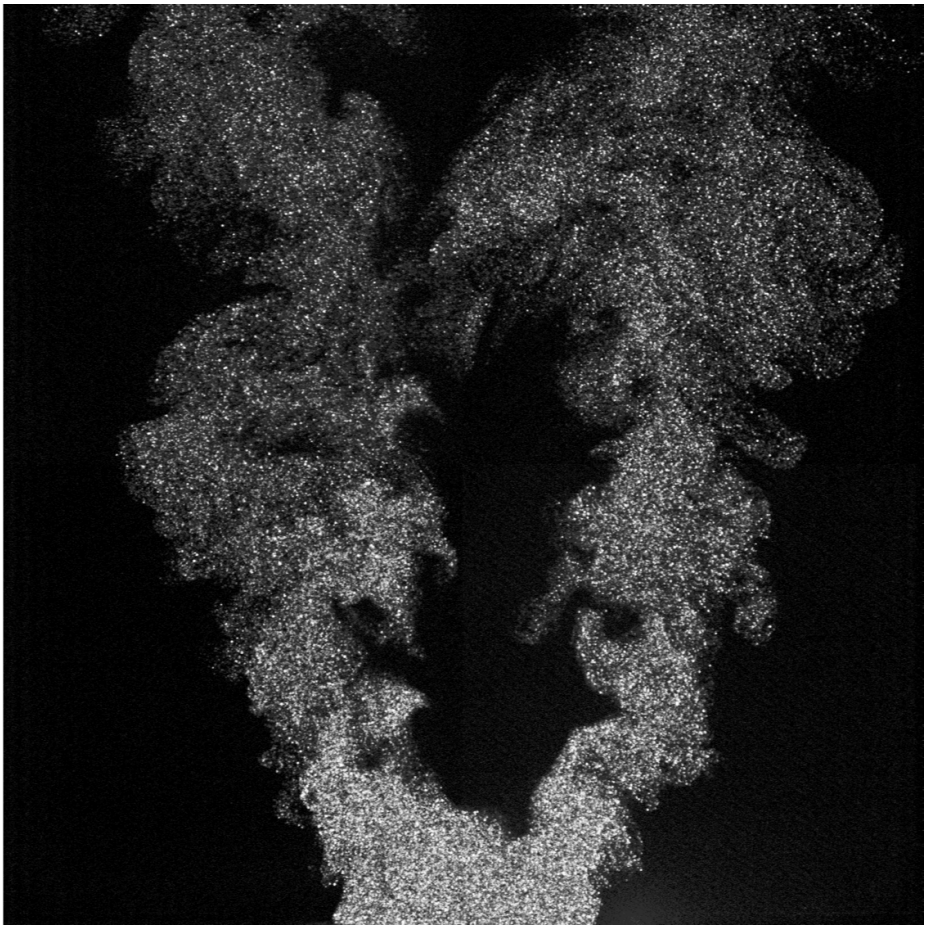

Figure 3.10: Typical image of silicon oil seeding with the flame visible in the center where the oil has been vaporized.

The flame front can be defined by a progress variable, c, which is defined by Equation 3.1.

$$c = \frac{T - T_{\mathrm{R}}}{T_{\mathrm{P}} - T_{\mathrm{R}}} \tag{3.1}$$

where T represents the temperature, $\mathrm{T_R}$ is the unburnt reactant mixture, and $\mathrm{T_P}$ is the burned products temperature.

By using the properties of the silicon oil which vaporizes at a temperature of $\sim$ 415 K which corresponds to a $c = 0.05$ - 0.07 depending on the stoichiometry of the mixture which in this work is methane at $0.8 < \phi < 1.0$. This value is consistent with the spread seen the previous data sets using $c = 0.02$ [36, 84] and a constant temperature of 600 K [39] which has a similar range of progress variable ranges in this work.

Knowing that the methodology of using silicon oil to locate the position of the LE of the flame front was sound, a system was designed to seed the reactant flow with silicon oil. In order to accomplish this, three nebulizers by Meinhard®, model TQ-30-A3 Quartz concentric, were setup in parallel to vaporize the oil. The three

units were required to provide enough particles for all the conditions studied in this dissertation. The nebulizer requires a separate supply of airflow which was calibrated with the house air for a sweep of pressures. It was determined that a pressure of 30 psi would result in a flow rate of 1 SLPM of air for each nebulizer. In order to account for this airflow in the total mass flow rate of air, the Python DAQ code was modified to account for the nebulizer flow rate separately of the MFCs.

Secondly, a methodology to determine the flame front location from the images was required. A program was developed in Python by Darren Sholes of Fraunhofer EMI which reads the images and determines the location along the centerline with the highest gradient between the burnt and unburnt mixture representing the LE of the flame front. This location is reported as a pixel number which can then be converted into a physical distance based on the physical scales of the images. The code performs the following operations to each individual image:

1. Perform thresholding binarization to either turn all pixels to 0 (black) or 255 (white) using Otsu's method.

2. Perform Gaussian blur to aide in the edge detection with a region processing size of 13 x 13 pixels (x and y directions).

3. Remove any "holes" of discontinuity that may have resulted from the Gaussian blur by performing a morphology close operation which essentially fills in any holes that exist within a continuous portion of the image.

4. Perform additional thresholding operation so that a clear boundary exists between the burnt and unburnt portions of the image.

5. Detect the axial pixel location along the centerline where the pixel changes from black to white and report this vertical (y) location.

An example set of processed output images is seen in Figure 3.11 where the left image shows the location algorithm pointing to the minimum x and y location, and the location of the flame front along the centerline. The right image shows the processed image after the first four operations listed above.

The processing of the images has some level of error or uncertainty and in this case, it is largely a function of the blur kernel size of 13 pixels in the 2-D plane space. When converting the pixel space to physical dimensions, for this experimental setup, approximately 40 pixels represent 1 mm of physical space, therefore 13 pixels (in both positive and negative directions) would represent about 0.65 mm of error in the flame location. This value is low compared to the displacement distances that are being measured.

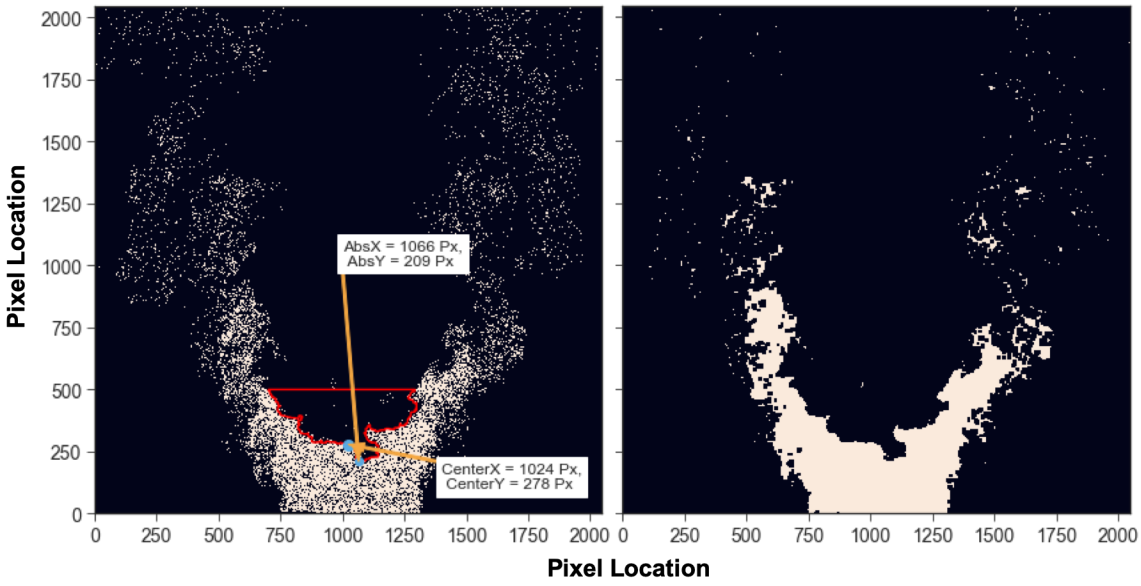

Figure 3.11: Images of processed flame front location images. Left is a processed image pointing to the global minimum flame location, and right showing the processed image with a closed surface.

Chapter 4

Experimental Results

This chapter has two main sections. The first section discusses the performance characteristics of the miniaturized LSB and the second delves into deep detail about the flowfield interrogation results.

4.1 GENSETS Microturbine Combustor Results

The first step to determine whether the LSB would be suitable for downscaled combustion systems was to understand whether the LSB could stabilize a flame at scales smaller than previously tested. The initial testing was performed using the GENSETS conditions, a U_0 of 9 m/s with a target $\phi = 0.65$. This was first accomplished by performing a visual examination of the flame shape to determine if the flowfield produced by the swirler is capable of stabilizing a flame. First, the LSB was fired into the open air which can be seen in Figure 4.1 in order to view the flame shape and liftoff distance.

A properly designed LSB will generate a bowl-shaped flame that has an LBO < 0.60 without exhibiting blowoff or flashback. In this case, the metal swirler and centerplate shown previously in Figure 3.2 has a lean blow off limit of $\phi = 0.58$ (using CH_4 and air) at $U_0 = 9$ m/s without flashback.

In previous studies, it was shown that the quarl serves as a flowfield divergence assistance mechanism while also helping to mitigate flame instabilities in the trailing edges of the bowl-shaped flame. It was demonstrated to not have an effect on flashback and flame stability. At the start of this study, it was unclear what quarl angle would be optimal for the miniaturized LSBs, and as a result, four units were fabricated with angles ranging from 20 to 35 degrees in 5 degree increments which can be seen in Figure 4.2. All of the quarls were fabricated with a fixed angle and have an inner diameter of 14 mm and extend to 2 * D (28 mm) at the outer edge. They therefore have a different height or depth since the angle determines the rate at which the geometry reaches the 28 mm outer diameter.

The performance metric for determining the optimal quarl angle was the ϕ at which LBO occurs. The testing procedure was as follows:

1. Start at sufficiently rich condition $\phi >$ LBO.

Figure 4.1: GENSETS LSB fired in the open air (no enclosure or quarl) at $\phi = 0.75$ showing a highly-stable, short, bowl-shaped flame.

2. Reduce fuel flow rate, hereby reducing ϕ in 0.01 increments, wait 30 seconds to determine if flame is stable.

3. If flame is stable, reduce ϕ by 0.01 to determine if new condition is stable.

4. Repeat above steps until flame is no longer stable and report the lowest ϕ at which flame can remain lit for the duration of the test.

The quarl with the best LBO performance (meaning leanest setting) at $6 < U_0 < 12$ m/s was found to be the 30 degree unit which can be seen in Figure 4.3. However, it was noted that LBO performance worsened (higher ϕ) with the addition of the quarl, which has never been seen before in testing of the LSB. Typically, the flame can be operated at the same ϕ with and without a quarl. A photograph of the flame with the 30 degree quarl is shown in Figure 4.4.

Finally, in the development of the miniaturized LSB, it was fired into a quartz tube that is 10 cm long and 4.2 cm in diameter with the quarl attached, simulating the enclosure of an engine combustor for emissions sampling which can be seen in Figure 4.5. The quartz cylinder helps stabilize the flame due to the hot wall boundary condition and in this configuration, LBO was measured to be $\phi = 0.55$ at $u_0 = 9$ m/s. This LBO value is similar to what is typically measured in the large-scale LSBs previously tested.

The next step in developing the miniaturized LSB was to determine the emissions performance using the experimental setup discussed in Chapter 3. Emissions were measured at a fixed fuel flow rate of CH_4 at a heat output of 3.33 kW from the burner. By varying U_0 from 7 to 10 m/s, the corresponding ϕ was 0.59 to 0.86. Expectedly, THC emissions were unmeasurable, even at the lowest range of 10 ppm on the Horiba FID analyzer. Figure 4.6 shows NO_x and CO emissions for the seven test points. At

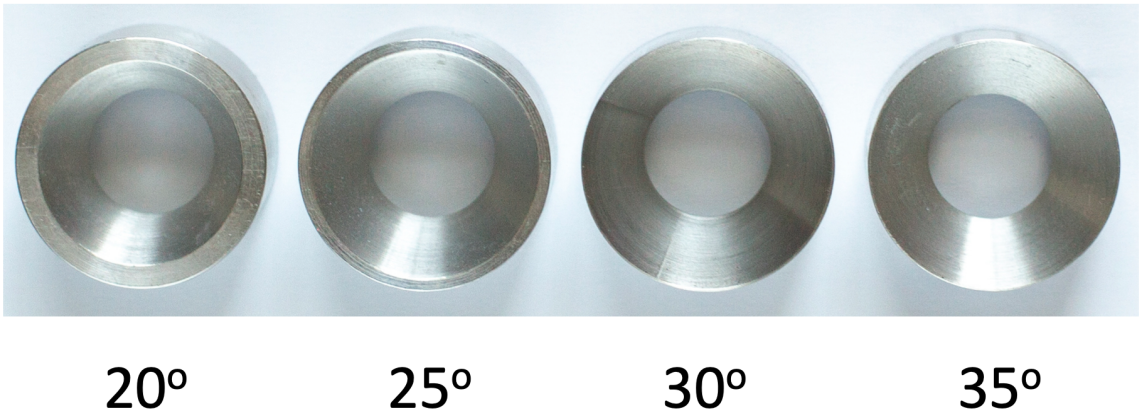

Figure 4.2: GENSETS 14 mm stainless steel quarls with divergent angles ranges from 20 to 35 degrees

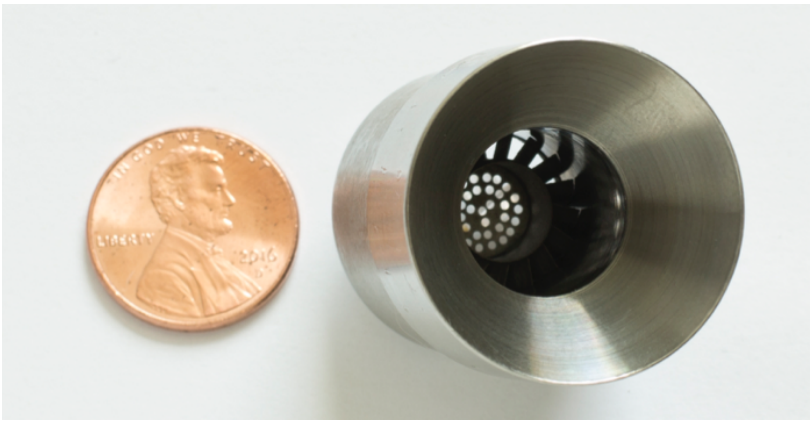

Figure 4.3: GENSETS 14 mm LSB assembly with interchangeable quarl, swirler, and center plate.

the targeted operating point of 9 m/s with $\phi = 0.65$, both NO_x and CO emissions are well below the targets. The emissions conversion to lb/MW-hr conservatively assumes that all NO_x emissions are in the form of NO_2 and the fuel is pure CH_4 with a heating value of 50.048 MJ/kg.

The burner emissions are extremely low and consistent with all previous tests of the LSB. For all data points shown in Figure 4.6, NO_x emissions are below 4 ppm and CO emissions are below 8 ppm (corrected to 15% O_2). In this measurement configuration, because the quartz tube is uncooled, NO_x emissions will be higher than it would be in an installed application (with a cooled wall) due to the elevated temperature of the combustion products. CO emissions are expected to be lower in this configuration than when operated with cooled wall due to the lack of wall quenching effects hereby cooling the products and generating more incomplete combustion products.

The Reynolds number of the LSB at these conditions was calculated to be 4725 (using the swirler diameter as the characteristic length) which is on the low end of the turbulent flow regime for pipe flow, which is estimated to start at Re = 4000. The

Figure 4.4: GENSETS 14 mm LSB fired in the open with a 30-degree quarl at $\phi = 0.75$ showing a highly stable, diverging flow field.

laminar regime extends until Re = 2300, while the transitional regime is considered to fall between 2300 < Re < 4000 [85]. While this LSB is at the low end of the turbulent regime, it is still considerably lower than any Re previously tested.

The visual test results, LBO data, and emissions performance of the miniaturized LSB indicate that while the operational flow conditions for the GENSETS LSB are in a regime that has not been well characterized, the fundamental principle governing the LSB appears to hold at this miniaturized scale. However, one phenomenon observed during testing is the addition of a quarl did not help stabilize the flame but instead destabilized the flame. This has never been observed before and opened the question of whether the heat loss of the flame to the quarl could be affecting LBO. In order to test this hypothesis, a second 30 degree quarl was manufactured in aluminum which has a significantly higher thermal conductivity, k, than stainless steel. If heat transfer, in the form of radiation or convection were affecting the flame, LBO would be different between the two material quarls. When tested, the LBO was identical between the two units. This result is expected because the flame does not physically touch the quarl and, therefore, the quarl material should not impact the flame in any regard. This indicates that the flowfield for the miniaturized LSB may be different than its large-scale counterparts.

Lastly, the pressure drop of the LSB was measured by inserting a pressure tap downstream of the swirler. Pressure drop was measured to be 0.19% which was far below the 3% target pressure drop required for the GENSETS program. This result is in agreement with the ultra-low pressure drop measured with the CV swirler developed in previous studies.

Furthermore, an open question that has not been answered in this dissertation is how the GENSETS LSB will perform at microturbine conditions with an elevated inlet temperature and pressure. It is expected that NO_x emissions will be significantly

Figure 4.5: 14 mm GENSETS LSB with quarl and quartz enclosure at $\phi = 0.75$ showing a highly stable and short flame.

higher due to the elevated temperature and it is also unclear if the LSB will perform when the Re is within the fully laminar regime. For the GENSETS conditions, the Re is calculated to be approximately 700. While the LSB was not tested at these conditions, it was fully integrated into the microturbine combustor and the results are shown in Appendix A with the filed provisional patent documents shown in Appendix B.

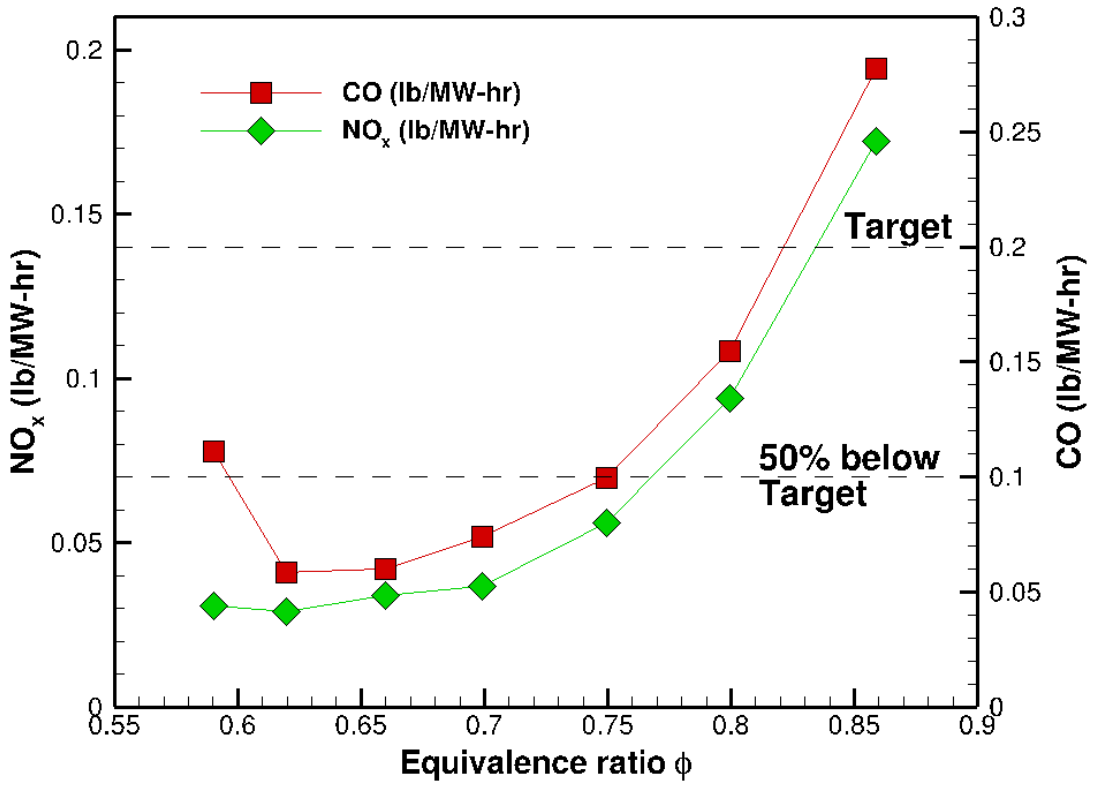

Figure 4.6: GENSETS LSB emissions at varying velocity and ϕ.

4.2 Experimental Results for LSB Flowfield Interrogation

The hardware that was tested for the GENSETS microturbine application had to be slightly modified to provide a greater flame standoff distance in order to interrogate the flowfield. As previously mentioned, the open area of the centerplate was modified to 30% and the three swirlers and centerplates shown in Figure 3.3 were used. In order to test the widest possible range, the conditions run are shown in Table 4.1.

The bulk inlet velocity is calculated using the total combined reactant flow rate of air and methane. The bulk inlet velocity range was chosen to extend from the lowest value that could sustain a flame at $\phi = 1$ without flashing back up to the highest limits that could be run. The equivalence ratio ranges from a lower lean limit of 0.8 up to 1.0. At low U_0, flashback is often an issue while collecting data, therefore at some conditions, the lowest velocity that was measurable was greater than 4 m/s. Likewise, due to LBO at higher U_0, certain data sets had to be operated at less than 16 m/s.

Run ID	ϕ	U_0 (m/s)	Heat Release (kW)
LSB12-0	0	4 - 16	0
LSB12-9	0.9	4 - 13	1.40 - 4.54
LSB12-1	1.0	5 - 16	1.94 - 6.21
LSB14-0	0	4 - 16	0
LSB14-8	0.8	4 - 9	1.69 - 3.80
LSB14-9	0.9	4 - 16	1.90 - 7.61
LSB14-1	1.0	5 - 16	2.64 - 8.45
LSB254-0	0	4 - 16	0
LSB254-8	0.8	4 - 16	5.56 - 22.25
LSB254-9	0.9	5 - 16	7.82 - 25.03
LSB254-1	1.0	6 - 16	10.43 - 27.82

Table 4.1: Summary of experimental conditions

4.2.1 Non-reacting PIV Flowfield Results

While the equations and analyses that have been shown in the background section were developed for conditions when a flame is present, it is also useful to examine the non-reacting flowfield of the LSB. More specifically, to understand how the terms on the LHS of Equation 2.16 change with varying U_0 and scale. Therefore, the first set of analysis that was performed was on the non-reacting flowfield.

The tests are represented by the three Run IDs: LSB12-0, LSB14-0, and LSB-254-0. The flowfield was examined in two manners. First, the velocity vectors and turbulence kinetic energy (TKE), q', were plotted in for all conditions and compared against legacy LSB data for larger scale burners. This qualitative analysis served as a check to visually interpret the flowfield outside of performing a quantitative analysis of the centerline data.

The TKE shown in this plot is defined as:

$$q' = \frac{1}{2}(u'^2 + v'^2)^{1/2} \tag{4.1}$$

While many comparisons were performed, a single plot of velocity vectors with an overlay of q' (color contours) for the non-reacting flow at $U_0 = 10$ m/s is shown in Figure 4.7. It can be seen that all three LSBs show a central zone of low q' caused by the decelerating flow downstream of the center plate. This region also has low TKE due to the low velocity (compared to the swirling flow). In this figure, the axial direction (y - axis) and radial direction (x - axis) are normalized by the burner diameter, D. Note, the axis scales in the figure are different for each case in order to show the entire velocity field for each size burner. Conversely, the highest q' exists in the regions of highest velocities located in the swirling region, consistent with all larger scale LSBs tested.

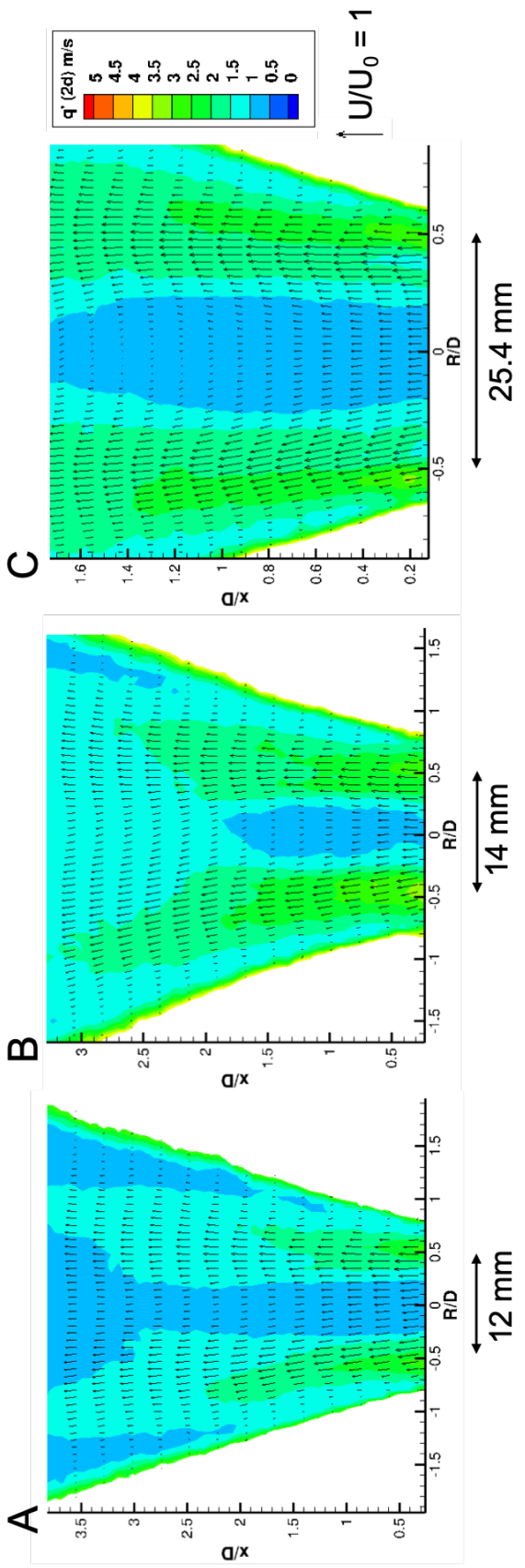

Figure 4.7: Mean velocity vectors superimposed on contours of 2-D turbulent kinetic energy for 12 mm (A), 14 mm (B), and 25.4 mm (C) LSBs. For all cases $U_0 = 10$, $\phi = 0$.

At high (>10 m/s) U_0, there is no sign of recirculation zone in any of the non-reacting cases, proving consistent with all previous observed experiments on the LSB. These same trends were observed at all velocities in the non-reacting flowfield. At a qualitative level, the miniaturized LSBs exhibit the same flowfield characteristics as their larger scale counterparts.

After the flowfield was inspected visually, the centerline profiles at each condition were extracted and post processed for analysis. An example of the centerline axial velocity profile vs. axial distance is shown in Figure 4.8 for the three different diameter LSBs at U_0 = 10 m/s. All of the burners show the linear deceleration in the nearfield that is expected for the LSB. It can be noted that the slope for the 12 and 14 mm LSBs are similar, but the 25.4 mm LSB has a lower slope meaning that the flow is decelerating at a slower rate than the smaller LSBs.

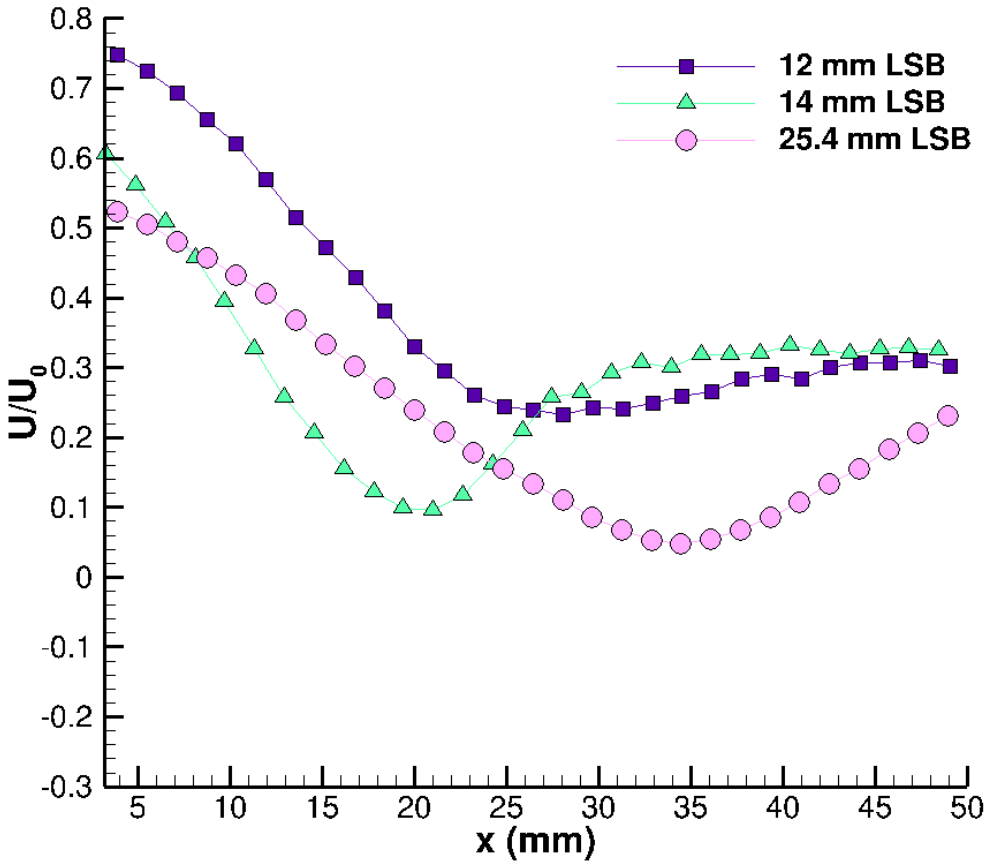

Figure 4.8: Extracted centerline data for U/U_0 vs. axial distance at U_0 = 10 m/s, ϕ = 0.

In addition to examining the centerline velocity, the TKE was also plotted for the same condition as above, which can be seen in Figure 4.9. In past works on

larger scale LSBs, q'/U_0 was constant in the nearfield and the miniaturized LSBs exhibit the same behavior with q'/U_0 being almost constant for x < 20 mm for all burners. Additionally, the value of q'/U_0 is within the range reported in previous LSB developments from approximately 0.03 to 0.07 in the nearfield [50].

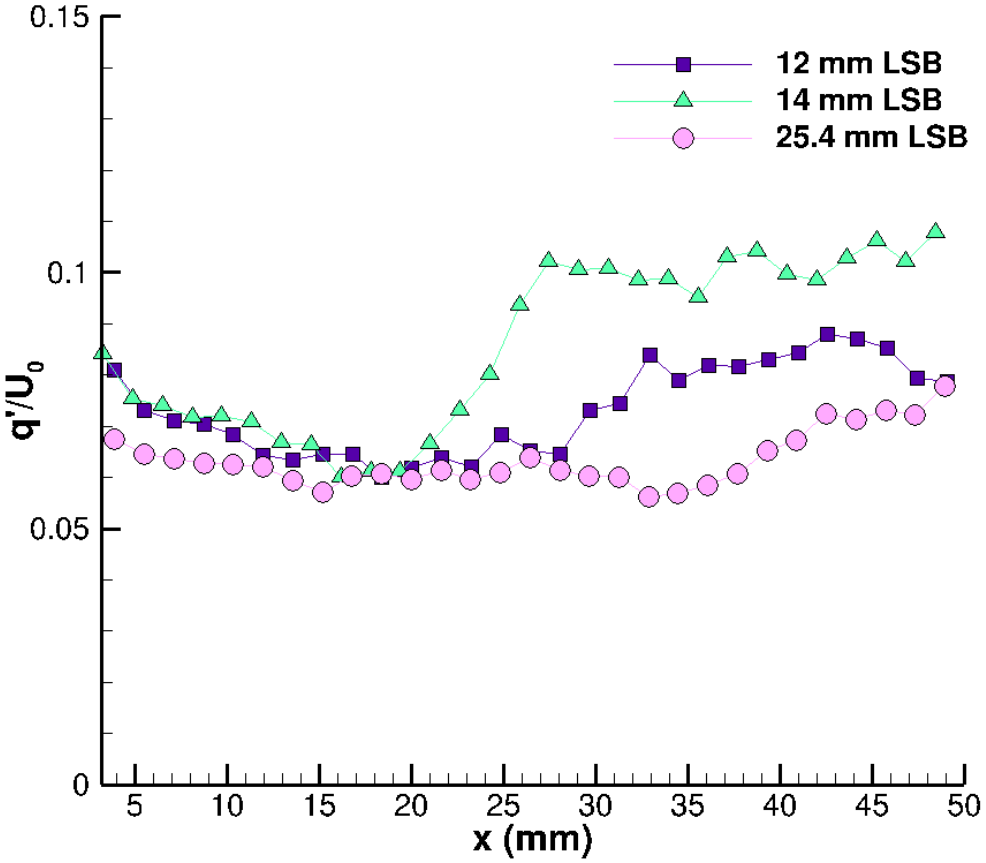

Figure 4.9: Extracted centerline data for TKE vs. axial distance at U_0 = 10 m/s, ϕ = 0.

This analysis used a best fit line in the nearfield for all data sets and the R-squared value was required to be over 0.95. From this analysis, two parameters were extracted, the normalized rate of axial divergence, $dU/dx/U_0$, (a_x), and the y-intercept which could then be used to calculate the virtual origin position, x_0, or the point where the axial velocity is equal to the bulk inlet velocity ($U = U_0$). The extracted values of a_x are shown in Figure 4.10.

For the three LSBs, it is clear that the effects of scaling have an impact on the flowfield because the rate of divergence is different. While the 12 mm and 14 mm LSB are grouped together closely, the 25.4 mm unit has a lower (less steep) rate of deceleration. It can also be noted that the value of a_x decreases (becomes more

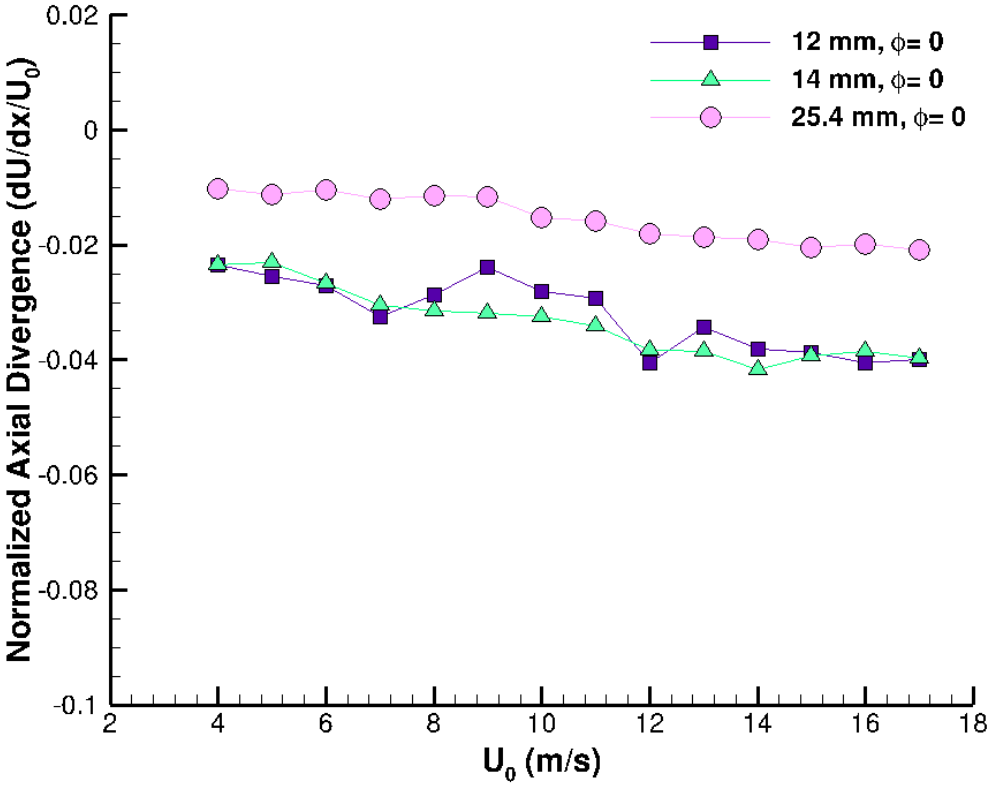

Figure 4.10: Extracted centerline data for normalized axial divergence rate, a_x, vs. velocity for $\phi = 0$.

negative) with increasing U_0. This trend has been seen in previous works [42, 54] but with smaller differences across a similar operating range.

The virtual origin position, x_0, was also deduced from the non-reacting centerline data and can be seen in Figure 4.11. The virtual origin position magnitude is a function of the burner diameter so it is expected that the larger LSBs will have a smaller (more negative) position. The negative value of x_0 is due to the fact that the zero position is defined at the burner dump plane and the virtual origin is located behind this position by this convention. For the 12 and 14 mm LSBs, it can be seen that x_0 remains somewhat constant across the U_0 range, whereas for the 25.4 mm unit, x_0 starts off smaller and then increases before flattening out as U_0 increases. In the previous works, more specifically the work by Day and Cheng [54], the opposite trend was noted at low U_0, however, the same flattening of x_0 with increasing U_0 was noted.

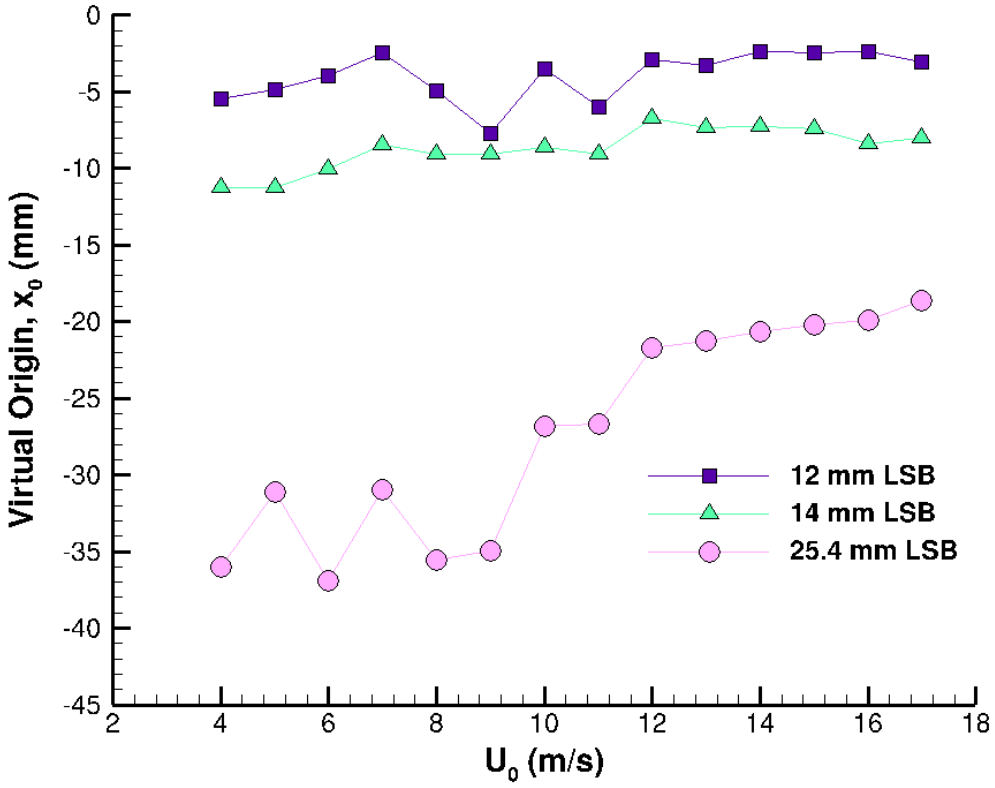

Figure 4.11: Extracted centerline data for virtual origin position, x_0, vs. velocity for $\phi = 0$.

Conclusions from non-reacting flowfield analysis

Based on examining the non-reacting flowfield qualitatively by viewing velocity vectors and TKE, few differences exist between the miniaturized LSBs and their larger scale counterparts. Furthermore, by performing a full analysis of the flowfield by extracting the centerline parameters, the effects of scale can be seen in a_x which appears to scale with the size of the burner, an observation that has not been seen in past studies. The virtual origin position expectedly scales with burner size and exhibits similar behavior seen in larger burners. While small differences are noted, overall, the non-reacting flowfield on the miniaturized LSBs is consistent with all LSBs tested at larger scales.

4.2.2 Reacting PIV Flowfield Results

After the full analysis of the non-reacting flowfield was performed, the reacting cases were tested. First, all of the flames were examined in the open at the full range of conditions. Figure 4.12 shows the three LSBs at the same condition as the non-reacting cases of $U_0 = 10$, $\phi = 0.80$. The biggest takeaway from this image is the large

scale difference between the three LSBs. When viewing only the LSB hardware, the size difference between them is not evident, however, when examining the flame size, the scale is obvious. An interesting observation to note is that in this single image, the flame position appears constant between 12, 14, and 25.4 mm LSBs which could be a consequence of the linear scaling of the geometry between the three swirlers.

Figure 4.12: Images of 12 mm, 14 mm, 25.4 mm (from left to right) LSB Operating with $U_0 = 10$ m/s, $\phi = 0.80$.

Next, the LBO was measured in the open by the procedure described in the approach and experimental setup section. The LBO measured for the three LSBs can be seen in Figure 4.13. The curves for LBO are not as initially anticipated for multiple reasons. First, all of the previous LSBs tested at larger scales, across a wide range of U_0 (4 - 120 m/s), had a virtually constant LBO. In the case of small-scale LSBs, the LBO exhibits a parabolic shape across the U_0 range tested. This implies that at both high and low U_0, a higher heat release rate (HRR) is required to sustain a flame. Based on these LBO curves, it is not evident as to why this would occur, but external air entrainment is suspected as a possible cause. The second observed deviation in the data set occurs between the three diameter LSBs. It is clear that the scale of the LSB affects LBO significantly. At smaller scales, a larger HRR is required to sustain a flame. This difference is very evident even between the 12 and 14 mm and again, external air entrainment is suspected as the cause, but cannot be proven based on this data.

Additionally, in order to study the dynamics of the flame, a high speed camera by Photron was used to visually asses the motion of the flame. This camera was briefly used to capture the flame dynamically at a rate of 4,000 frames per second (fps) with a 1 megapixel resolution. Two frames of the video can be seen in Figure 4.14. The main observation from this video is that the axial flame position appears to be moving at a scale equivalent to the burner diameter, which is significantly larger than other LSBs. The use of these video images, however, are not quantitative and merely offer a glimpse into the structure and properties of the flame.

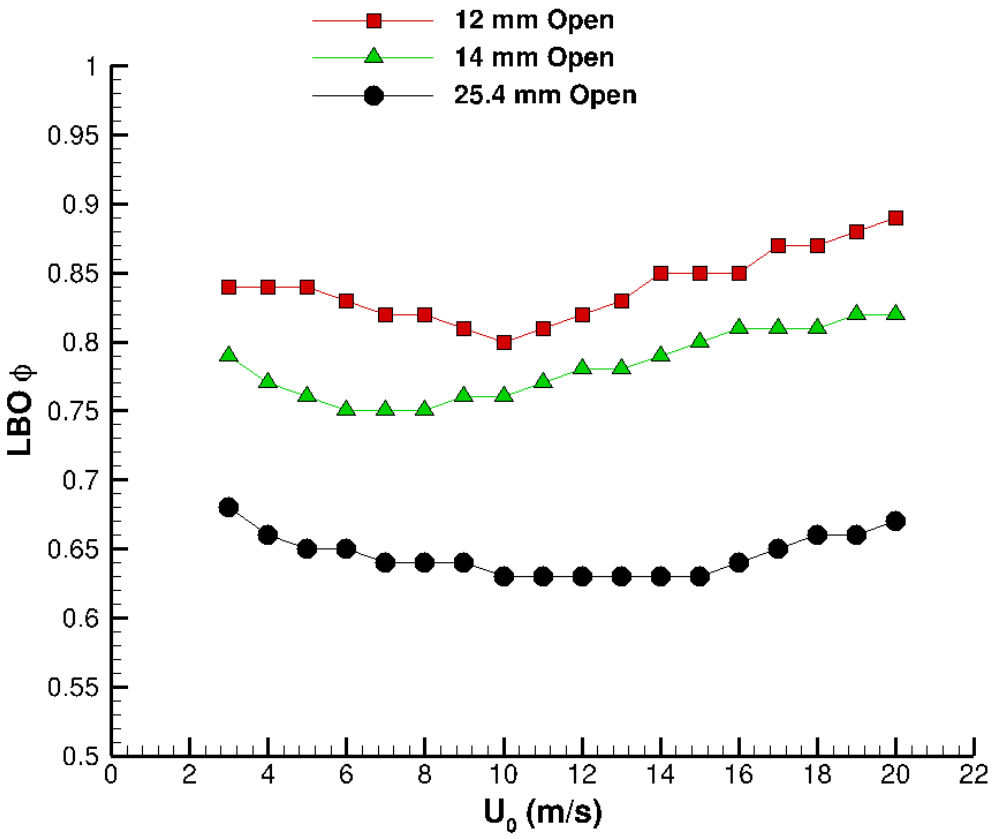

Figure 4.13: Measured LBO in the open for the 12, 14, and 25.4 mm LSBs at varying U_0.

After the qualitative analysis of the flame was performed by the high speed video, a visualization of vectors with an overlay of TKE was plotted and can be seen in Figure 4.15 at $U_0 = 10$ m/s, $\phi = 0.90$. Note that $\phi = 0.90$ had to be used instead of 0.80 due to the high LBO of the 12 mm LSB. The plots appear similar to the non-reacting cases shown in Figure 4.7, although a more detail interrogation uncovers noticeable differences. First, the width of all the flowfields are noticeably larger in the radial direction due to the expansion of the burned gas. Secondly, the white line indicates an area of zero axial velocity, showing the presence of a recirculation zone. For both the 12 and 14 mm LSB, the recirculation zone occurs in approximately the same location, 1 * D, however in the 25.4 mm LSB, the recirculation zone shifts downstream to about 1.6 * D. While the recirculation zone is downstream of the flame in all cases (results for the flame location will be discussed later in this section), the recirculation zone is close to the flame front for all three LSBs. The fact that the recirculation zone exists further upstream (closer to the flame front) than has been seen in larger scale LSBs indicates that scale is impacting the LSB flowfield. However, the fundamental properties of the LSB flowfield are still present.

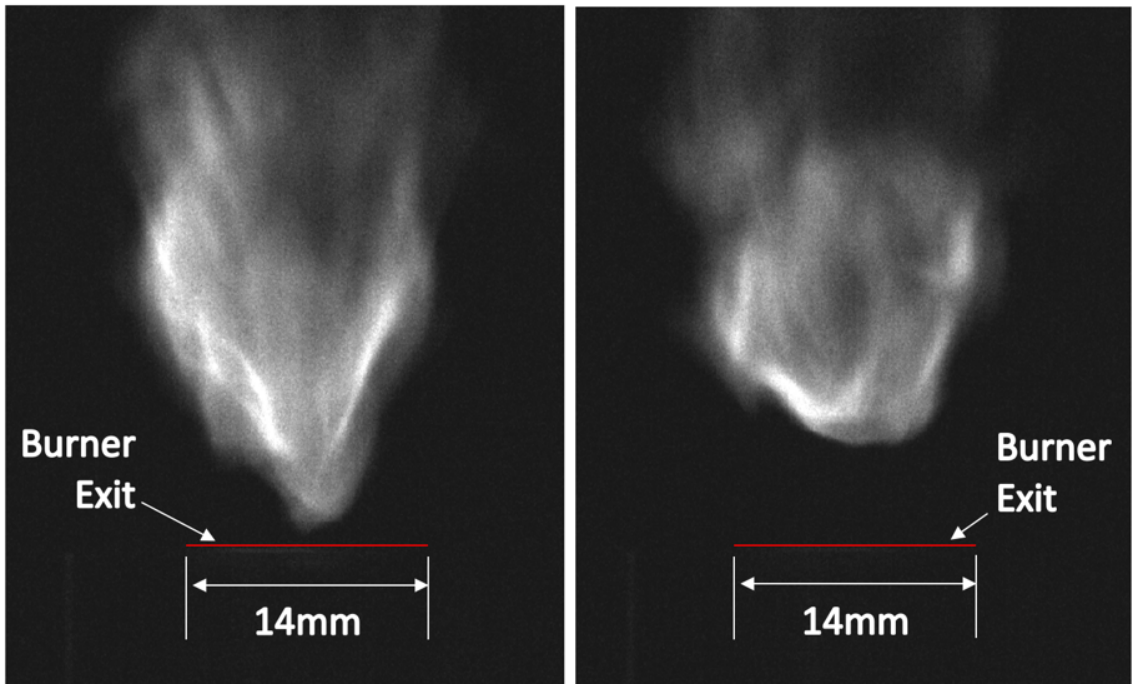

Figure 4.14: Still frames from a high-speed camera video of a 14 mm diameter LSB. $U_0 = 10$ m/s, $\phi = 0.80$.

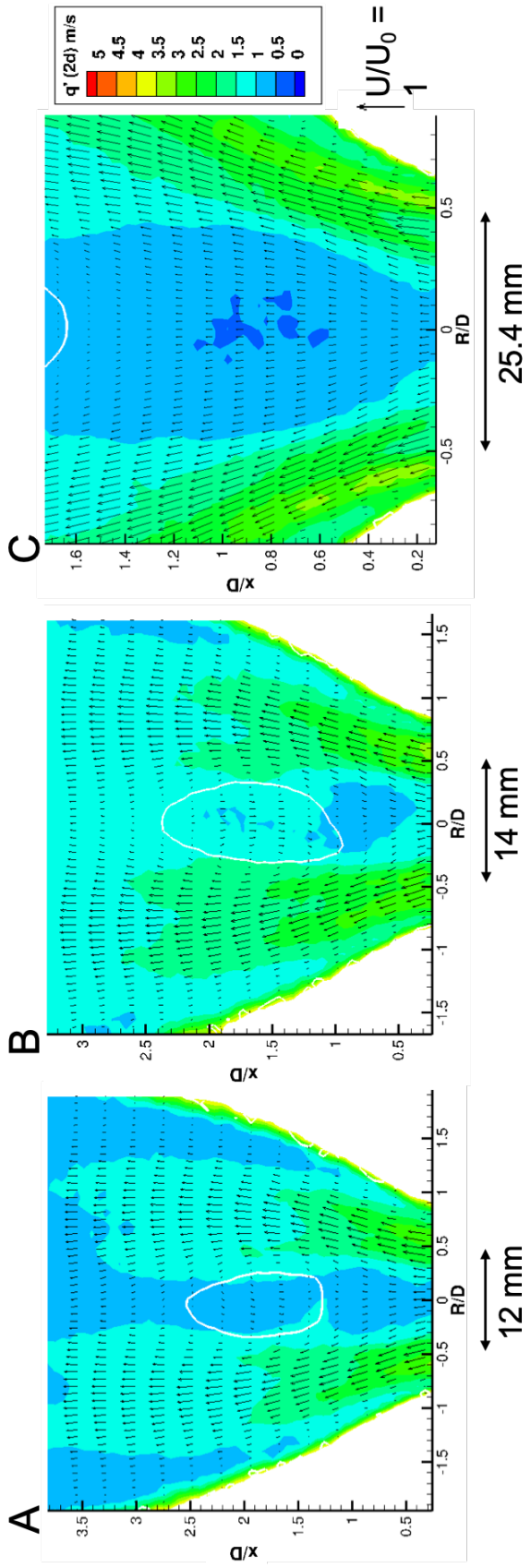

Figure 4.15: Mean velocity vectors superimposed on contours of 2-D turbulent kinetic energy for 12 mm (A), 14 mm (B), and 25.4 mm (C) LSBs. For all cases $U_0 = 10$, $\phi = 0.90$. White coloring indicates location of zero axial velocity.

Similar to the analysis performed for the non-reacting flow cases, the centerline profiles at all conditions were plotted and examined. Results from $U_0 = 10$ m/s, $\phi = 0.90$ are shown in Figure 4.16. Similar to the $\phi = 0$ case, the linear deceleration in the nearfield is clearly visible. However, the presence of the flame (in the form of a change in slope) in the nearfield is now observable. When processing the value of a_x, the linear data is fitted up to this location for all conditions. It is apparent that the smaller LSBs (12 and 14 mm) are less influenced by the flame generated acceleration, whereas the 25.4 mm LSB shows a large acceleration due to the flame. The lack of flame generated acceleration in the smaller LSBs could be due to the very small heat release that is exhibited at these conditions. Furthermore, the recirculation zone that was visible in Figure 4.15 can be seen in the negative U/U_0 in the farfield. The flowfields in this analysis are consistent with their larger scale counterparts in the nearfield leading up to the flame front.

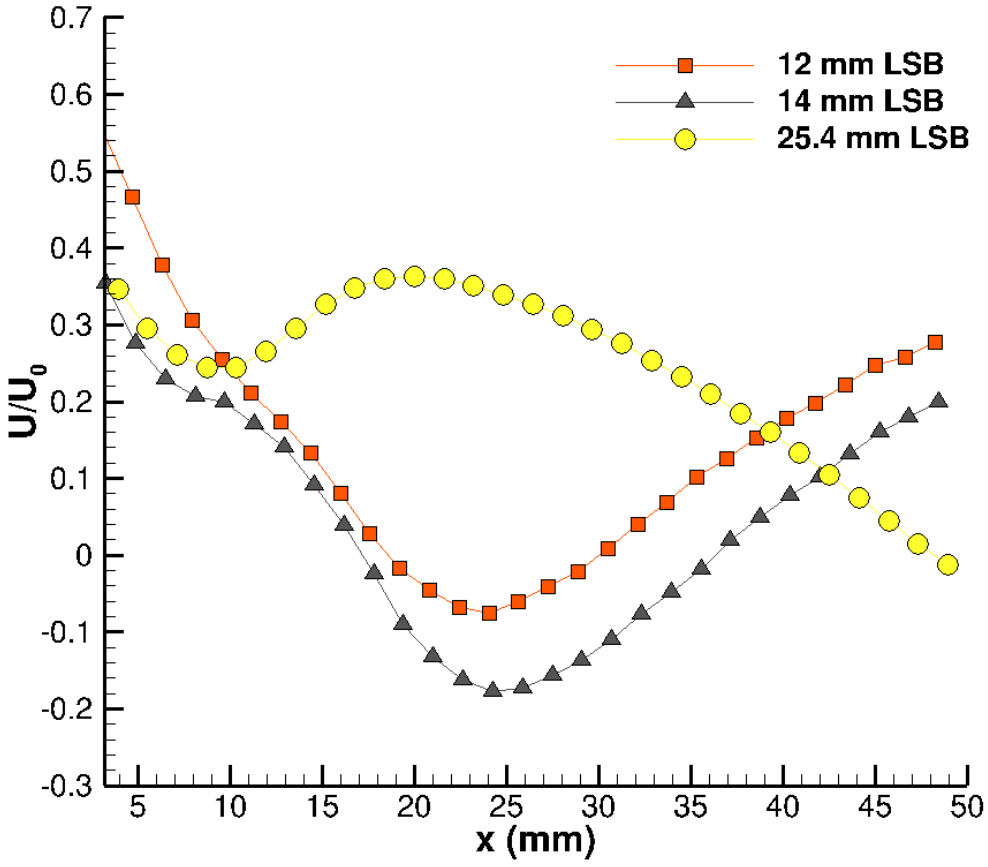

Figure 4.16: Extracted centerline data for U/U_0 vs. axial distance at $U_0 = 10$ m/s, $\phi = 0.90$.

In addition to the centerline velocity, the values of q'/U_0 along the centerline

can be seen in Figure 4.17. In this plot, the value of q'/U_0 is similar between the three different diameter LSBs in the nearfield, but show slightly different trends. The 14 mm LSB shows a decreasing value whereas the 12 and 25.4 mm LSB show an increasing value. These trends, however, have both been seen in previous LSB studies [42, 50]. Furthermore, the value of q'/U_0 is within the same range of all LSBs tested at various scales.

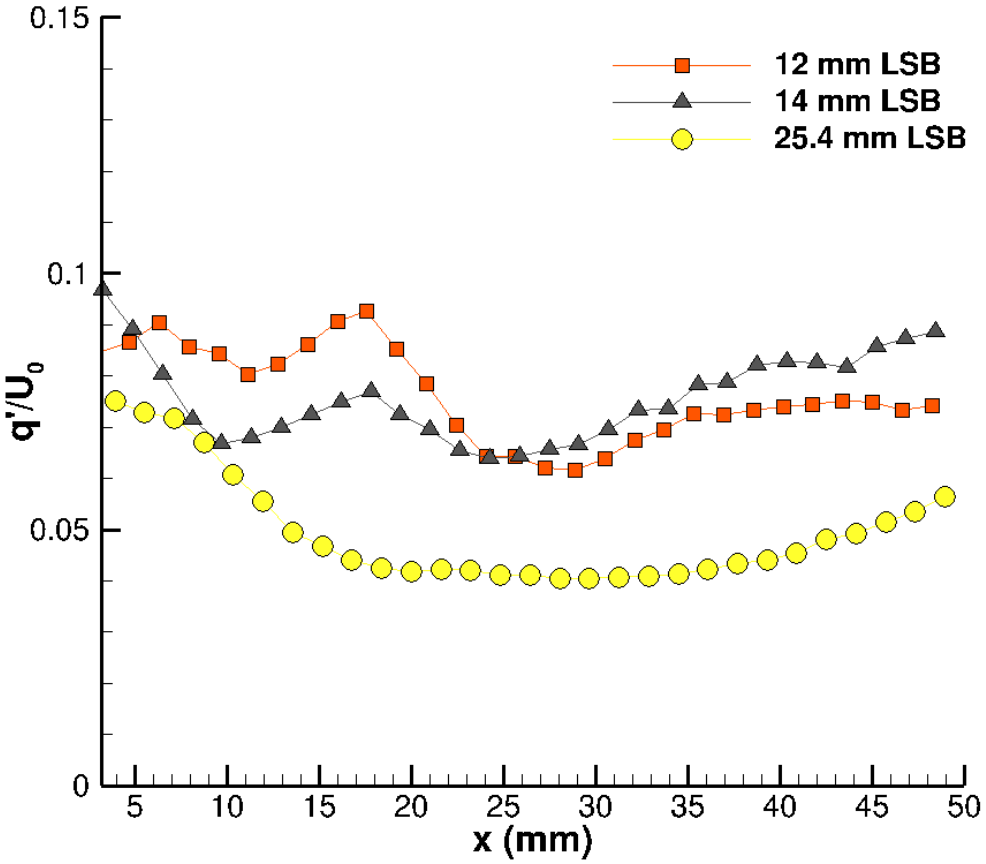

Figure 4.17: Extracted centerline data for TKE vs. axial distance at U_0 = 10 m/s, ϕ = 0.90.

The normalized axial divergence was also calculated for all of the reacting flow conditions and can be seen in Figure 4.18. The trends observed in the non-reacting flow are present in all of the reacting cases. As U_0 increases, the rate of divergence decreases (becomes more negative) across the range tested. The magnitude of the divergence overall is higher with the presence of the flame, a trend that has been seen in all past LSB developments. We can again see the effects of scaling, with the smallest LSB exhibiting the highest rate of deceleration and the largest LSB having the smallest divergence rate, whereas in large-scale LSBs, the divergence is usually

constant. Additionally, as previously mentioned, the range of U_0 varies for each LSB depending on ϕ due to flashback at high U_0, and LBO at low U_0. While the divergence rate does show some variation with U_0, the trends that the small LSBs exhibit are similar to what has been seen in large-scale LSBs.

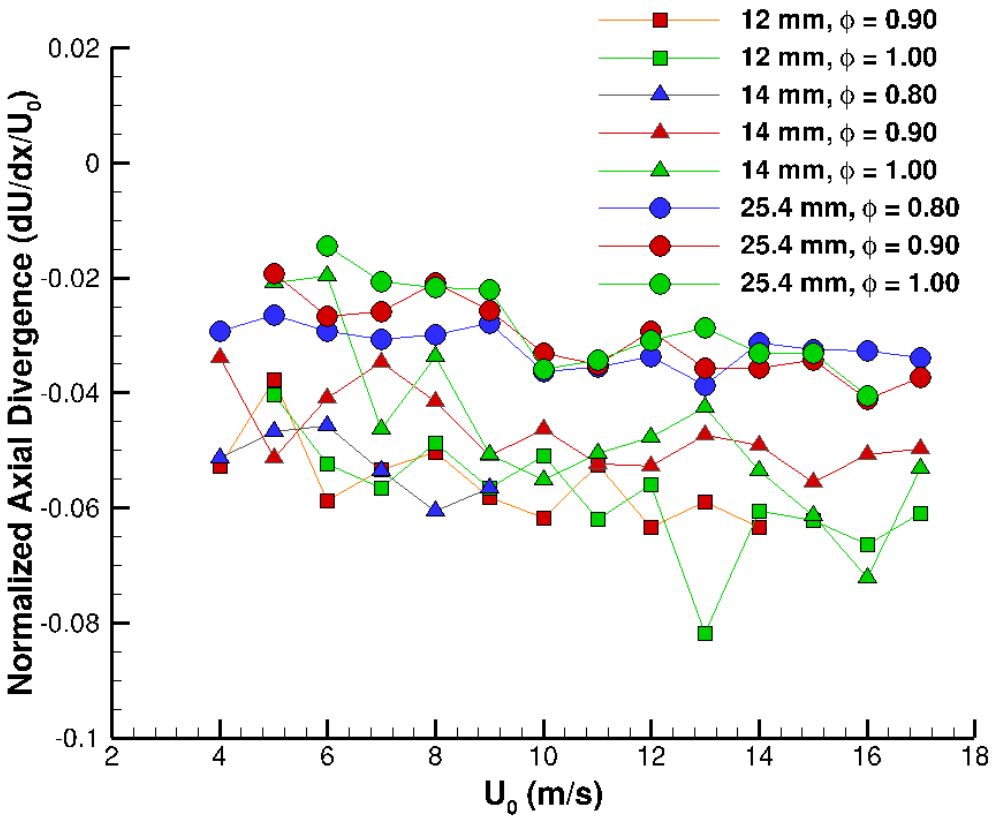

Figure 4.18: Extracted centerline data for normalized axial divergence rate, a_x, vs. velocity.

The virtual origin was again post processed for the reacting cases at each condition. As expected, x_0 scales with the burner diameter. The 12 mm LSB shows a fairly constant value across the entire range of U_0, however, the 14 mm and 25.4 mm diameter LSBs show more scatter at $U_0 < 9$ m/s. The variation in the low U_0 cases could be due to the fact that the flame position is very close to the LSB dump plane and therefore the post processing can only be done for a very short distance. While there is little difference in the divergence rate between all cases as shown in Figure 4.18, the difference in x_0 between the LSBs is more noticeable. Additionally, the same trends that existed in the non-reacting flowfield exist in all of the reacting cases for all burners, indicating that the results are consistent between the two data sets.

Up until this point, all of the data shown has been collected using the PIV system, and seeded with Aerosil® particles which helps gain an understanding of the terms on the LHS on Equation 2.16. Understanding how the terms behave at various scales

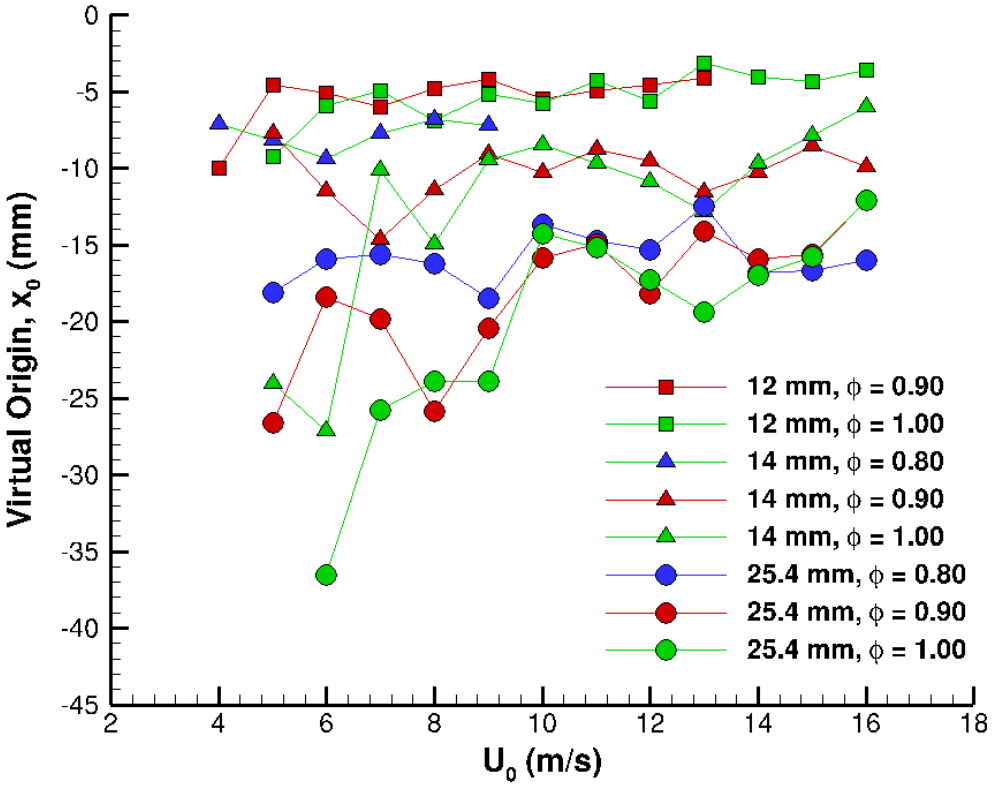

Figure 4.19: Extracted centerline data for virtual origin position, x_0, vs. U_0.

and velocities gives key insight into how the flowfield is evolving. It is also pertinent to further break down the terms on the RHS of Equation 2.16 to understand the burning rate. However, in order to determine a burning rate, the flame front location, x_f, is required. In order to determine x_f, 1000 images were captured for each individual condition (U_0 and ϕ) and a probability density function (PDF) was developed in addition to a cumulative density function (CDF). The CDF value is represented by $\overline{c}$ or the mean progress variable.

When analyzing the data, it was found that the bin size utilized was very important in determining the peak value of the PDF. A bin size of 40 pixels which represents 1 mm of physical space was utilized for all analysis. While the peak value of the PDF, representing the most probable flame location is a useful metric, it is dependent on the bin size. As a result, $\overline{c} = 0.5$ was considered to be the mean flame front location. An example $\overline{c}$ for three conditions is shown in Figure 4.20.

The post processed mean flame position results for all conditions studied is shown in Figure 4.21. There are many observations that can be made from the data that help us gain insight into the flowfield properties. First, if we examine the impact of equivalence ratio on flame position, for all three LSBs, the leaner conditions produce a higher (further away from swirler) axial flame position, and conversely, the richer

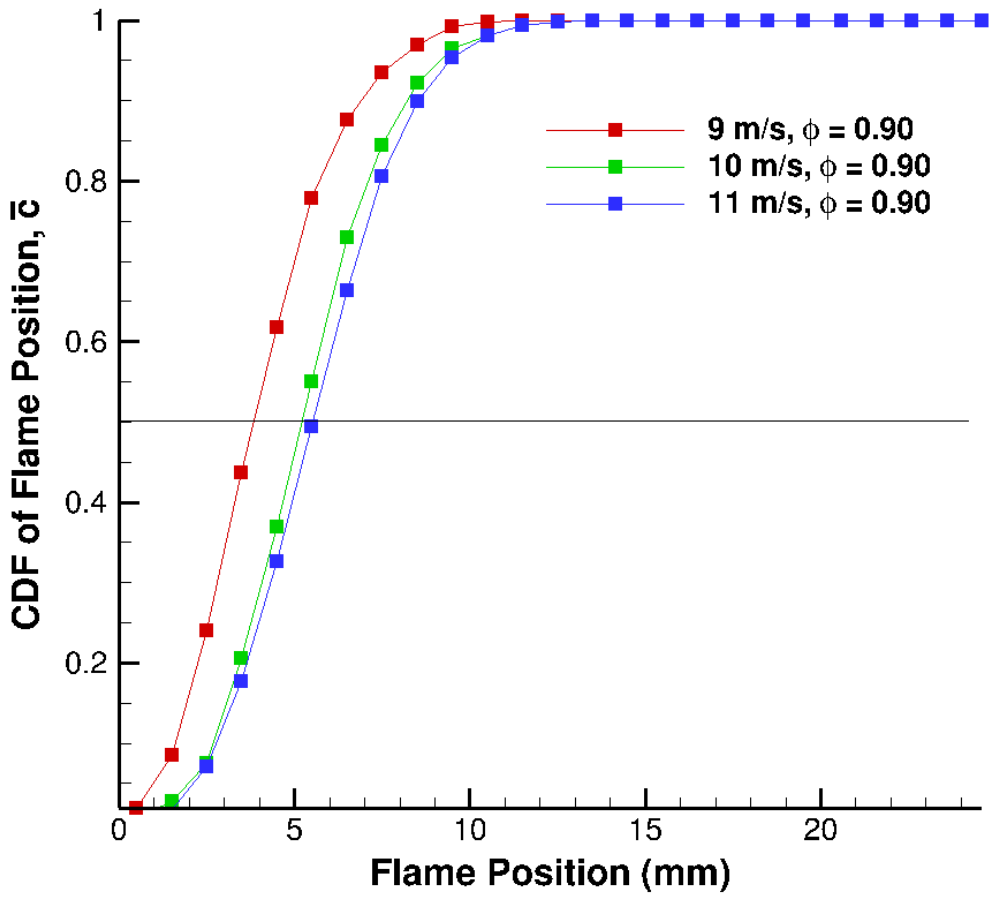

Figure 4.20: $\bar{c}$ of the axial flame position for 3 conditions run with the 14 mm diameter LSB

conditions have a flame position closer to the LSB dump plane. This is an expected result since high equivalence ratios have a higher flame speed, and at low U_0, the flame speed can be a significant contributor to the turbulent burning velocity. Secondly, all three LSBs show the same trend with increasing U_0, an increasing flame position. This is not necessarily an expected result, because in larger LSBs, the flame position is typically constant across the operating range. However, very few studies have been performed at low U_0 and at small scales, resulting in a smaller Re than previously tested.

Additionally, it is expected that the flame position magnitude would be a function of the burner diameter, however, the 12 mm and 14 mm LSBs are switched, with the 14 mm LSB having the flame position that is closest to the burner dump plane of the three LSBs tested. While not completely conclusive, this is an indication that the burner scale is impacting the reacting flowfield.

While the flame position itself provides useful insight, a better metric is how the

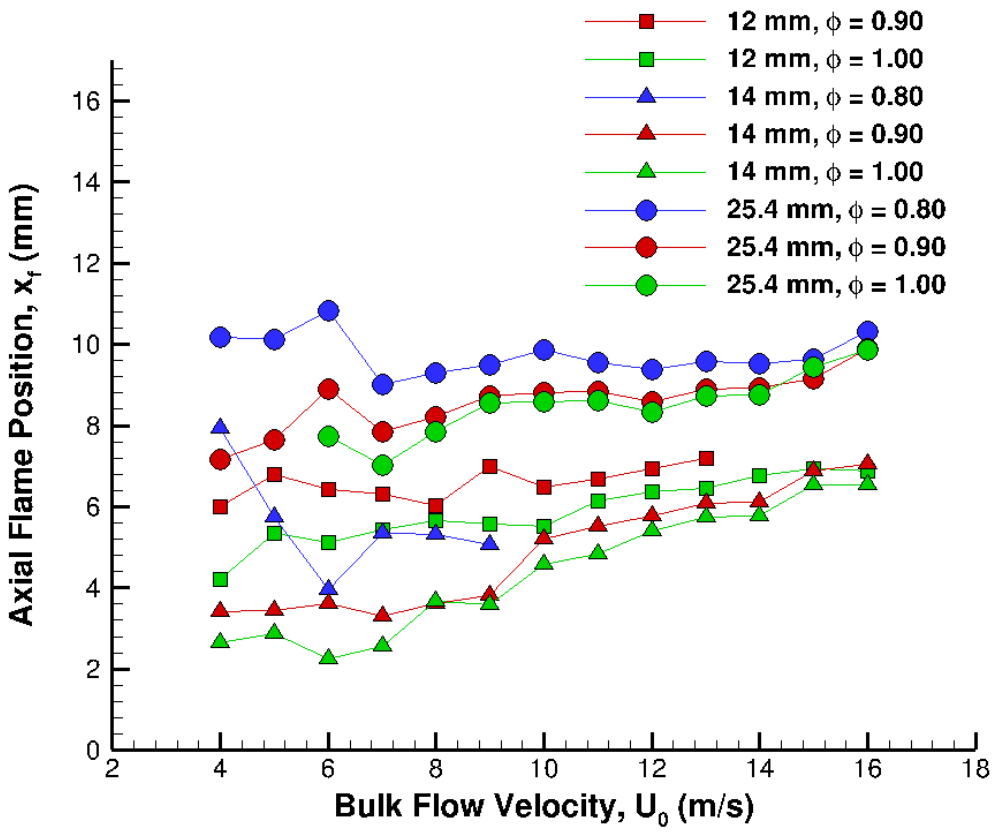

Figure 4.21: Mean axial flame position for the miniaturized LSBs at varying U_0 and ϕ. Values are obtained from silicon oil images.

flow structure shifts axially in the burner. More specifically, it is necessary to track the value of the flame displacement (x_f - x_0) which considers the shift in virtual origin in conjunction with the flame position. This term also directly appears in Equation 2.16. The results for the flame displacement are shown in Figure 4.22.

There are many observations that can be deduced from this data. First, the scale of each burner is now in the "correct" order with the 12 mm LSB having the smallest displacement and the 25.4 mm LSB having the largest displacement. This contrasts the reversing of the 12 and 14 mm LSBs shown in the axial flame position plot. Additionally, it can be noted that outside of a few low U_0 points for the 25.4 mm and 12 mm LSB, the flame displacement is mostly constant across the U_0 range tested. This indicates that the flow structure is shifting within the burner.

Furthermore, in addition to the mean flame position, it is very important to gain an understanding of the evolution of the flame position, which provides insight to the flowfield properties. This can be best expressed by the flame brush thickness, δ_T, which is defined as $0.10 < \bar{c} < 0.90$. This definition is consistent with the work performed by Bell et al. in [86] and describes how the flame deviates from the mean position.

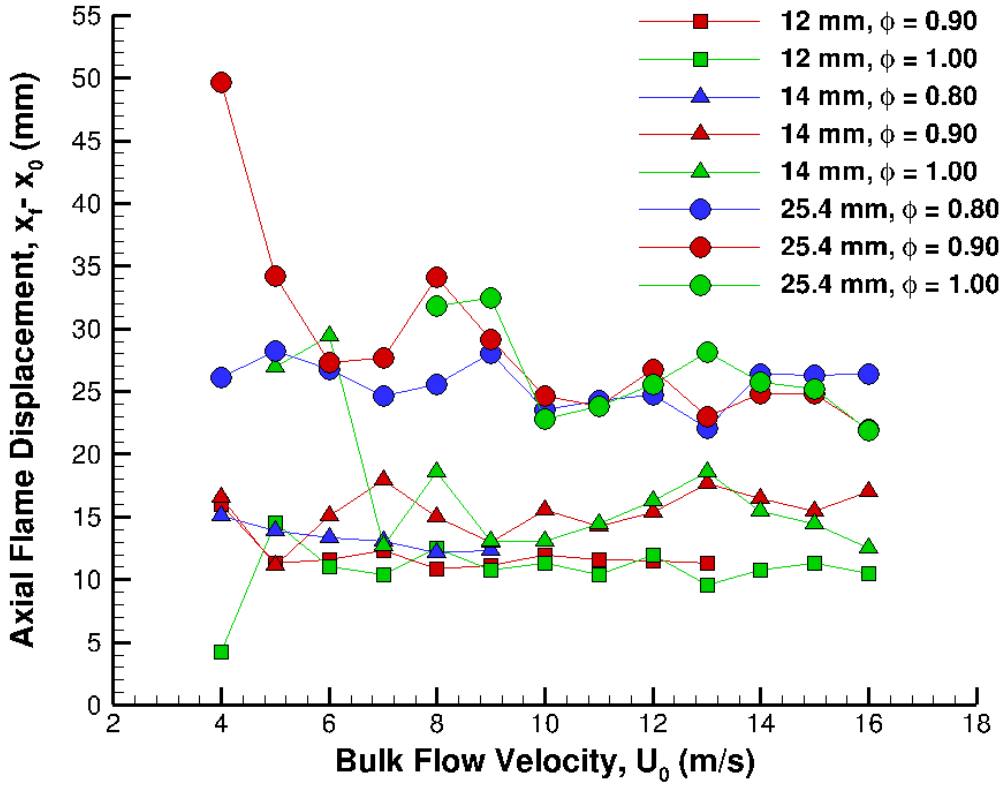

Figure 4.22: Mean axial flame displacement for the miniaturized LSBs. Values are obtained for a combination of PIV and silicon oil images.

During the visual inspection process and analysis of the high speed video, it was expected that the miniaturized LSBs would have a large flame brush thickness compared to burner diameter. Additionally, at low U_0, it was suspected that the flame brush would become larger because visually, the flame appears to move a greater distance axially. However, the results for δ_T are shown in Figure 4.23 and for all the conditions studied, the flame brush remains relatively constant. Additionally, δ_T scales with the burner diameter. Both of these conclusions are consistent with large-scale LSBs previously tested.

Up until this point in the data analysis, there has been little deviation in the flowfield properties between the miniaturized LSBs and their larger scale counterparts. However, as noted in Figure 4.13, the LBO curves appear to be a function of the burner scale and possibly other phenomenon. Now, we will focus our attention on the local displacement turbulent flame speed, $S_{T\text{-}LD}$. As discussed in the background section, for all larger-scale LSBs tested, $S_{T\text{-}LD}$ has been shown to have a linear correlation with the turbulence intensity, which was seen in Figure 2.10. The turbulent burning velocity and the rms velocity statistics were extracted from the averaged PIV results at the mean flame position, $\bar{c} = 0.5$. The values of $S_{T\text{-}LD}$ for the three different

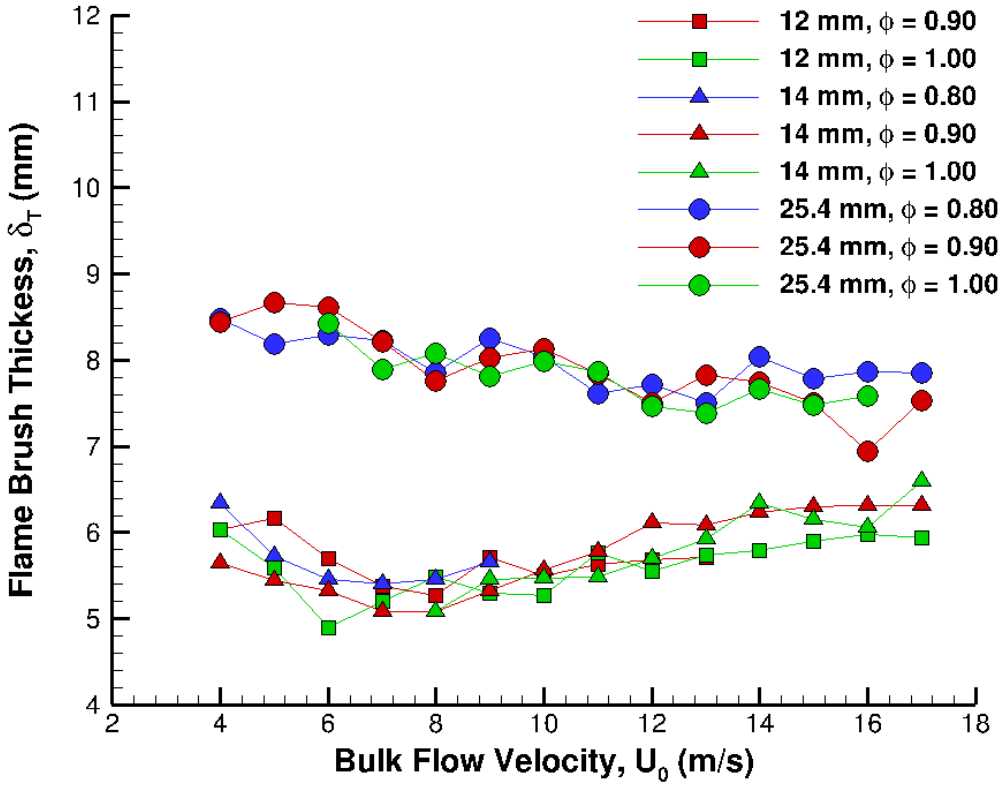

Figure 4.23: Flame brush thickness vs $U_f$or the miniaturizes LSBs.

diameter LSBs is shown in Figure 4.24 with a correlation line indicative of previous large-scale LSB data. It can be seen that at low turbulence intensities (low U_0), the data is consistent with the legacy data, yet at higher u', the data shows the "bending" phenomenon described by Peters [72].

While the "bending" phenomenon has been widely observed in the past in all types of burners besides the LSB, there has surprisingly been no proven explanation as to why this occurs. The leveling-off of the burning rate with increasing u' indicates that the flame cannot keep up with the turbulence and is therefore not able to burn at a high enough speed to match the reactant burning velocity. Driscoll [79] and others have suggested that "bending" can occur for a variety of reasons. First, getting into a little of the background, the burning velocity is proportional to the flame surface density Σ and δ_T. It is predicted that as u' increases, δ increases as well, and bending occurs as the flame surfaces merge when the turbulence level reaches a threshold value. There are also other factors including geometry dependence, that affect the flame surface density, Σ, and δ_T simultaneously. However, one of the problems in past studies is the lack of rigorous documentation of all parameters needed to accurately describe S_T.

In the search to understand why the miniaturized LSBs exhibited "bending" of

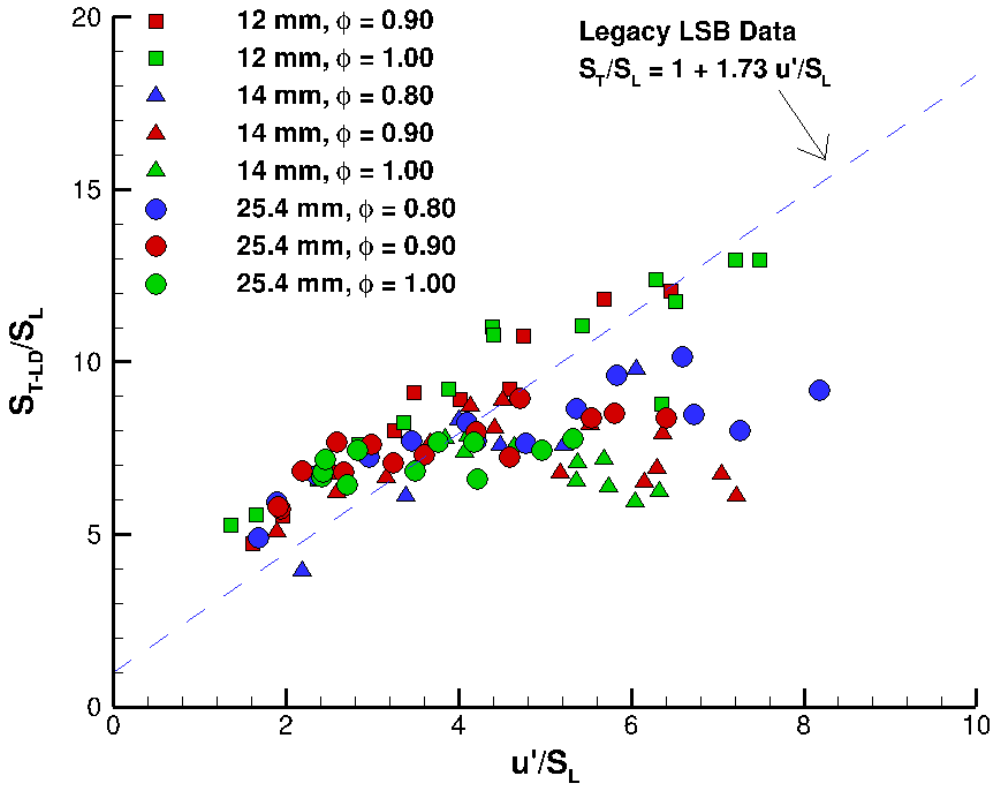

Figure 4.24: $S_{T\text{-}LD}$ vs u' both normalized to S_L for miniaturized LSBs across a range of U_0 and ϕ.

$S_{T\text{-}LD}$, the LBO curve was examined further as a possible answer. It was suspected that the miniaturized LSBs could be entraining a proportionally larger volume of air at the trailing edges of the flame. In other words, as the LSB scales down, the turbulent core becomes proportionally smaller than the outer area of the flame.

In order to test this hypothesis, LBO was test in two configurations, first, when fitted with a 30 degree quarl which can be seen in Figure 4.25 and secondly with a quarl and quartz tube.

The LBO with the quarl produces very different results than LBO measured in the open. The LBO for the 25.4 mm LSB is very similar at $U_0 < 8$ m/s, however, at $U_0 > 8$ m/s, the LBO linearly increases to a ϕ higher than measured in the open. The 12 and 14 mm LSB have the same trend as the 25.4 mm LSB, linearly increasing as U_0 increases. This is consistent with the air entrainment hypothesis since the quarl opens the flame angle further than when the flame is fired in the open, hereby causing more air entrainment and a high ϕ at which LBO occurs.

The last test performed involved the elimination of air entrainment by enclosing the LSB in a quartz tube with the quarl. The quartz tube was 3 * D for all three different diameter LSBs and the results can be seen in Figure 4.26. For all three LSBs,

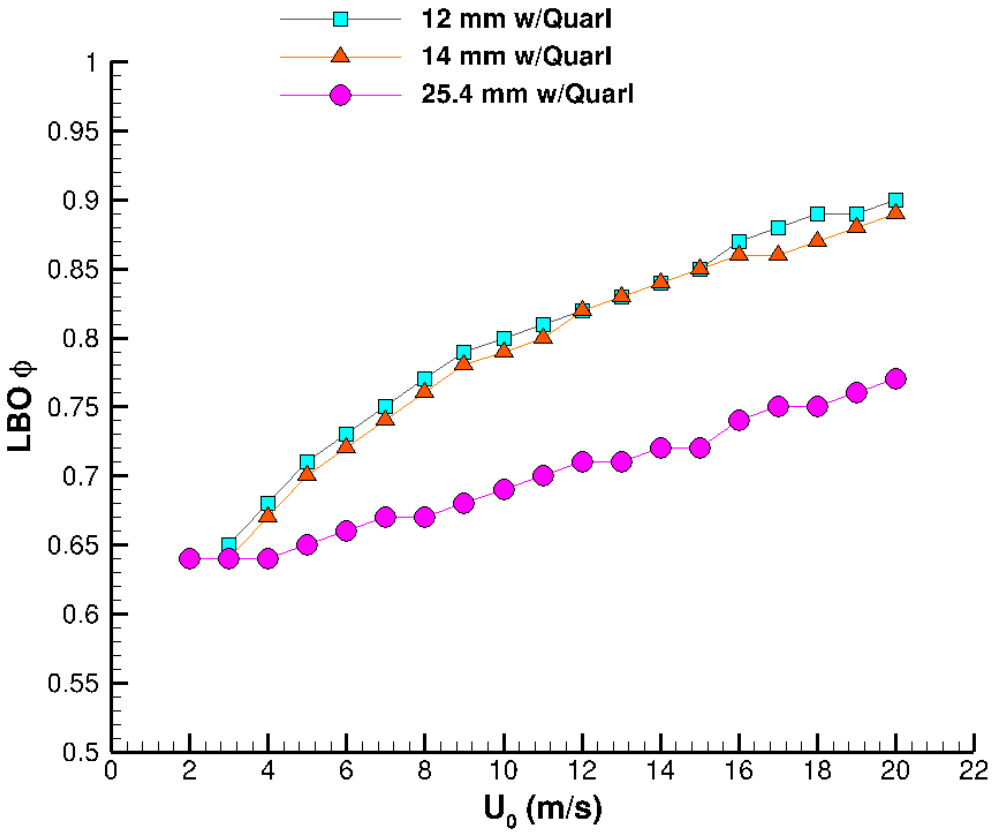

Figure 4.25: Measured LBO in the open with a quarl for the 12, 14, and 25.4 mm LSBs at varying U_0.

LBO is nearly the same and leaner than all measurement methods. When performing these measurements, special care was taken to ensure that the affect of the hot wall did not effect the LBO measurement. In each case, the quartz was allowed to fully cool before each measurement was started and the flame was ignited at the leanest condition possible instead of stepping down in ϕ as described in the earlier procedure.

The results of this test indicate that air entrainment is the cause of the "bending" that is seen in S_T. The only way to completely verify this conclusion would be to perform a measurement with a quarl made of quartz with an attached quartz tube, however, this measurement would be nearly impossible to perform at this scale. Even at large scales, a very limited number of experiments were performed with only a quartz tube (not a quartz quarl) and due to the particle adhesion to the wall, consistent results were a challenge [50]. At small scales, particle adhesion is an even larger challenge than in larger-scale systems. Additionally, another huge challenge is line of sight access through highly curved surfaces that would be required if a quartz quarl and small diameter quartz tube were used.

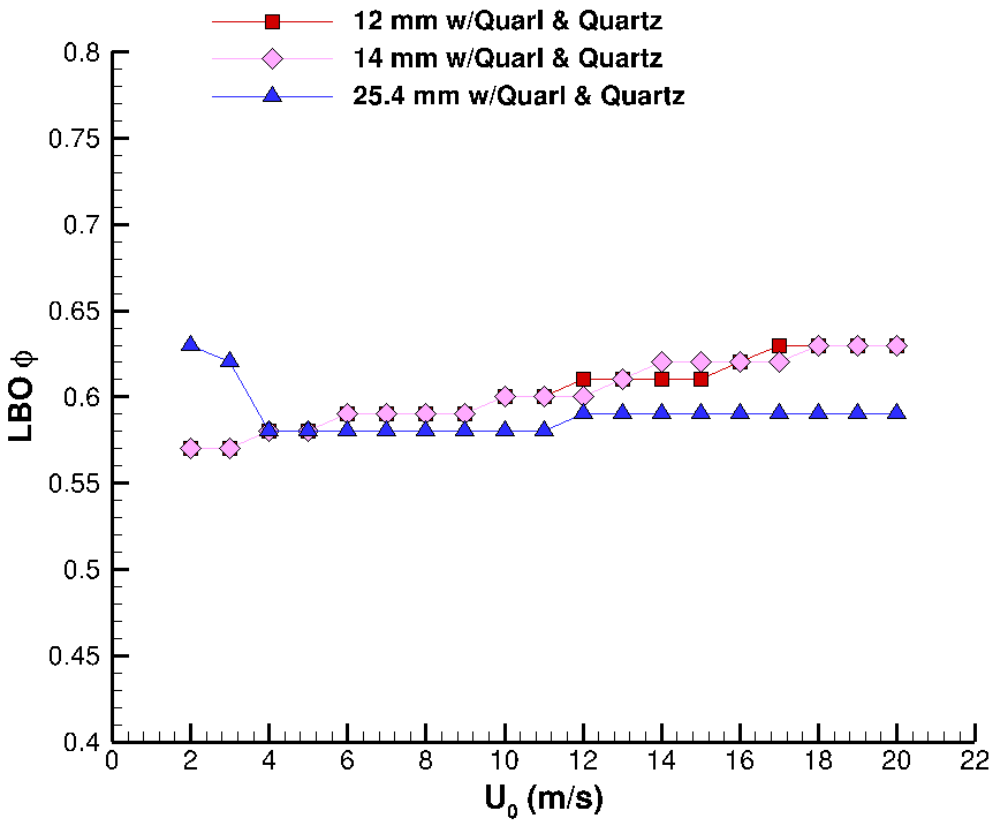

Figure 4.26: Measured LBO with a quarl and quartz tube for the 12, 14, and 25.4 mm LSBs at varying U_0.

Chapter 5

Concluding Remarks

This chapter summarizes the results and knowledge gained from the experimental results. Possible future research directions in the field of low swirl burners are also suggested.

5.1 Conclusions

Based on the experimental studies that were performed on the LSB, the following conclusions can be drawn:

- From an operational perspective and as a combustion system for future small-scale systems, the miniaturized LSBs exhibit all of the behaviors seen in large-scale LSBs. The miniaturized LSB can achieve ultra low NO_x and CO emissions, ultra low pressure drop, and show no signs of flashback. This indicates that the LSB is an acceptable technology for future small-scale energy systems.

- When interrogated in the open, a requirement for laser diagnostics, from a non-reacting flow perspective, the effects of downscaling do have an impact on the flowfield evolution but do not alter the governing principals of the LSB. The nearfield shows a linear deceleration, a hallmark of the LSB. Post processed results for the normalized axial divergence and the virtual origin are consistent with larger LSBs previously tested.

- When interrogated in the open with a flame present, noticeable differences in the flowfield exist on the miniaturized LSBs. First, the ϕ at which LBO occurs shows a significant effect of scaling, specifically at high U_0, requiring higher heat release rates to sustain a flame. Post processed parameters for the flame position, normalized axial divergence, and virtual origin for the small-scale LSBs are largely similar to their large-scale counterparts. However, the measured turbulent burning velocity no longer scales linearly with the rms velocity.

- The non-linear dependence of S_T on u' is likely caused by air entrainment on the trailing edges of the flame, which also cause the elevated LBO ϕ. While these results are inconsistent, the elimination of air entrainment in the form of a quarl and quartz tube show a near constant LBO across the range of U_0 tested on all miniaturized LSBs.

- The observation that air entrainment plays such a large role on the burning rate of the miniaturized LSBs indicates that measuring $S_{T\text{-}LD}$ in the open using laser diagnostics is not optimal.

5.2 Future Work

- While interrogation of the flowfield with a quarl fabricated from quartz and an enclosure may not possible, it is suggested to model the miniaturized LSBs both in the open and with the enclosure to fully understand the flowfield at these conditions. Because of the small size, modeling with LES or DNS may be possible without a huge computational burden.

- There is currently only one study proving the viability of operating the LSB on liquid fuels. It would be beneficial to demonstrate the operability of small-scale LSBs on liquid fuels for transportation applications, such as drones or range extenders for automobiles.

- All of the testing performed in this dissertation was at atmospheric temperature and pressure. However, many of the applications of future downsized energy systems are recuperated cycles which typically require high combustor inlet temperatures at low pressures. This poses a problem for two reasons; first, from a turbulence perspective, and secondly from a NO_x emissions aspect. At the GENSETS microturbine condition (T = 950 K, P = 3 atm) the Reynolds number is approximately 700 which is in the fully laminar flow regime. The open question is whether the LSB can operate at this condition with essentially no turbulence. Secondly, NO_x emissions are a strong function of temperature and a heated inlet result in a very high combustion temperature. It is not yet clear if the emissions targets can be met at these conditions.

Bibliography

[1] International Energy Agency, "Market Report Series: Gas 2017, Analysis and Forecasts to 2022," tech. rep., International Energy Agency, 2017.

[2] Department of Energy, "GENSETS Program Overview," tech. rep., Advanced Research Projects Agency - Energy, 2014.

[3] S. Murugan and B. Horák, "A Review of Micro Combined Heat and Power Systems for Residential Applications," *Renewable and Sustainable Energy Reviews*, vol. 64, pp. 144–162, 2016.

[4] M. Ara, T. Takaishi, and K. Togawa, "An Introduction of Micro Combined Heat and Power Generation Unit for Residential Use," in *International Gas Union*, 2003.

[5] W. P. J. Visser, S. Shakariyants, M. de Later, A. Haj Ayed, and K. Kusterer, "Performance Optimization of a 3 kW Microturbine for CHP Applications," in *Proceedings of ASME Turbo Expo 2012*, (Denmark), pp. 1–10, American Society of Mechanical Engineers, 2012.

[6] E. S. Barbieri, P. R. Spina, and M. Venturini, "Analysis of Innovative Micro-CHP Systems to Meet Household Energy Demands," *Applied Energy*, vol. 97, pp. 723–733, 2012.

[7] J.-C. Zhao, "An Introduction to the ARPA-E GENSETS Program," in *WADE DistribuGen Conference*, 2015.

[8] E. Sher and I. Sher, "Theoretical Limits of Scaling-down Internal Combustion Engines," *Chemical Engineering Science*, vol. 66, pp. 260–267, 2011.

[9] P. Therkelsen and D. Dunn-Rankin, "Small-scale HCCI Engine Operation," *Combustion Science and Technology*, vol. 183, no. 9, pp. 928–946, 2011.

[10] R. Deam, E. Leema, B. Mace, and R. Collins, "On Scaling Down Turbines to Millimeter Size," *Journal for Gas Turbine and Power*, vol. 130, no. 5, pp. 1–9, 2008.

[11] A. C. Fernandez-Pello, "Micropower Generation Using Combustion: Issues and Approaches," *Proceedings of the Combustion Institute*, vol. 29, pp. 883–899, 2002.

[12] N. I. Kim, S. Aizumi, T. Yokomori, S. Kato, T. Fujimori, and K. Maruta, "Development and Scale Effects of Small Swiss-roll Combustors," *Proceedings of the Combustion Institute*, vol. 31 II, pp. 3243–3250, 2007.

[13] R. Keogh, "40 kW Turbo-Alternator Hybrid-Electric Range Extender," tech. rep., Metis Design, 2015.

[14] A. A. Shah, "Unique Gas Turbine Engine Powers Quieter, More Reliable Drones," 2018.

[15] Aerco, "Turndown Vs. Valve Position," 2019.

[16] V. H. Rapp, "How the Low-Swirl Burner Can Improve Residential Water Heating," tech. rep., Lawrence Berkeley National Laboratory, 2017.

[17] S. Mcallister, J.-Y. Chen, and A. C. Fernandez-Pello, *Fundamentals of Combustion Processes*. New York: Springer, 2011.

[18] Y. Ju and K. Maruta, "Microscale Combustion : Technology Development and Fundamental Research," *Progress in Energy and Combustion Science*, vol. 37, no. 6, pp. 669–715, 2011.

[19] J. Warnatz, U. Maas, and R. Dibble, *Combustion: Physical and Chemical Fundamentals, Modeling and Simulation, Experiments, Pollutant Formation*. Springer, 4th editio ed., 2006.

[20] I. Glassman, R. A. Yetter, and N. G. Glumac, *Combustion*. Academy Press, fifth edit ed., 2015.

[21] J. A. Miller and C. T. Bowman, "Mechanism and Modeling of Nitrogen Chemistry in Combustion," *Progress in Energy and Combustion Science*, vol. 15, pp. 287–338, 1989.

[22] A. Frank and M. J. Castaldi, "CFD Analysis of Municipal Solid Waste Combustion Using Detailed Chemical Kinetic Modelling," *Waste Management and Research*, vol. 32, no. 8, pp. 745–754, 2014.

[23] S. R. Turns, *An Introduction to Combustion, Concepts and Applications*. McGraw-Hill, second edi ed., 2000.

[24] M. R. Johnson, D. Littlejohn, W. A. Nazeer, K. O. Smith, and R. K. Cheng, "A Comparison of the Flowfields and Emissions of High-swirl Injectors and Low-swirl Injectors for Lean Premixed Gas Turbines," *Proceedings of the Combustion Institute*, vol. 30 II, no. 2, pp. 2867–2874, 2005.

[25] N. Syred, "A Review of Oscillation Mechanisms and the Role of the Precessing Vortex Core (PVC) in Swirl Combustion Systems," *Progress in Energy and Combustion Science*, vol. 32, no. 2, pp. 93–161, 2006.

[26] P. L. Therkelsen, J. E. Portillo, D. Littlejohn, S. M. Martin, and R. K. Cheng, "Self-induced Unstable Behaviors of CH4 and H2/CH4 Flames in a Model Combustor with a Low-swirl Injector," *Combustion and Flame*, vol. 160, pp. 307–321, 2013.

[27] C. K. Chan, K. S. Lau, W. K. Chin, and R. K. Cheng, "Freely Propagating Open Premixed Turbulent Flames Stabilized by Swirl," in *Twenty-Fourth Symposium (International) on Combustion/The Combustion Institute,*, pp. 511–518, 1992.

[28] B. Bedat and R. K. Cheng, "Experimental Study of Premixed Flames in Intense Isotropic Turbulence," *Combustion and Flame*, vol. 100, no. August 1994, pp. 485–494, 1995.

[29] R K. Cheng, "Velocity and Scalar Characteristics of Premixed Turbulent Flames Stabilized by Weak Swirl," *Combustion and Flame*, vol. 101, no. 94, pp. 1–14, 1995.

[30] D. T. Yegian and R. K. Cheng, "Laboratory Study of a Low NOx Hot Water Heater with a Weak-swirl Burner," tech. rep., Lawrence Berkeley National Laboratory, 1995.

[31] D. T. Yegian and R. K. Cheng, "Development of a Lean Premixed Low-swirl Burner for Low NOx Practical Applications," *Combustion science and technology*, vol. 139, no. 1, pp. 207–227, 1998.

[32] D. T. Yegian, R. K. Cheng, R. L. Hack, M. Miyasato, A. Chang, and G. Samuel, "Scaling the Weak-Swirl Burner from 15 kW to 1 MW," tech. rep., Lawrence Berkeley National Laboratory/University of California, Irvine, 1998.

[33] R. K. Cheng, D. T. Yegian, M. Miyasato, G. Samuelson, C. Benson, R. Pellizzari, and P. Loftus, "Scaling and Development of Low-swirl Burners for Low-emission Furnaces and Boilers," in *Proceedings of the Combustion Institute*, vol. 28, pp. 1305–1313, 2000.

[34] D. Littlejohn, A. J. Majeski, S. Tonse, C. Castaldini, and R. K. Cheng, "Laboratory Investigation of an Ultra Low NOx Premixed Combustion Concept for Industrial Boilers," in *Proceedings of the Combustion Institute*, vol. 29, pp. 1115–1121, 2002.

[35] R. Cheng, S. A. Fable, D. Schmidt, L. Arellano, and K. O. Smith, "Development of a Low Swirl Injector Concept for Gas Turbines," *Proceedings of IJPGC 2001*, 2001.

[36] T. Plessing, C. Kortschik, N. Peters, M. Mansour, and R. Cheng, "Measurements of the Turbulent Burning Velocity and the Structure of Premixed Flames on a Low-swirl Burner," *Proceedings of the Combustion Institute*, vol. 28, no. 1, pp. 359–366, 2000.

[37] I. G. Shepherd and R. K. Cheng, "The Burning Rate of Premixed Flames in Moderate and Intense Turbulence," *Combustion and Flame*, vol. 127, no. 3, pp. 2066–2075, 2001.

[38] R. K. Cheng, I. G. Shepherd, B. Bédat, and L. Talbot, "Premixed Turbulent Flame Structures in Moderate and Intense Isotropic Turbulence," *Combustion Science and Technology*, vol. 174, pp. 29–59, 2002.

[39] I. G. Shepherd, R. K. Cheng, T. Plessing, C. Kortschik, and N. Peters, "Premixed Flame Front Structure in Intense Turbulence," in *Proceedings of the Combustion Institute*, vol. 29, pp. 1833–1840, 2002.

[40] C. Kortschik, T. Plessing, and N. Peters, "Laser Optical Investigation of Turbulent Transport of Temperature Ahead of the Preheat Zone in a Premixed Flame," *Combustion and Flame*, vol. 136, pp. 43–50, 2004.

[41] W. A. Nazeer, K. O. Smith, P. Sheppard, R. Cheng, and D. Littlejohn, "Full Scale Testing of a Low Swirl Fuel Injector Concept for Ultra-Low NOx Gas Turbine Combustion Systems," in *ASME Turbo Expo 2006: Power for Land, Sea, and Air*, pp. 1–9, 2006.

[42] R. K. Cheng, D. Littlejohn, W. A. Nazeer, and K. O. Smith, "Laboratory Studies of the Flow Field Characteristics of Low-swirl Injectors for Adaptation to Fuel-flexible Turbines," in *Proceedings of GT2006 ASME Turbo Expo 2006: Power for Land Sea and Air*, pp. 1–14, 2006.

[43] D. Littlejohn and R. K. Cheng, "Fuel Effects on a Low-swirl Injector for Lean Premixed Gas Turbines," *Proceedings of the Combustion Institute*, vol. 31, pp. 3155–3162, 2007.

[44] R. K. Cheng and D. Littlejohn, "Laboratory Study of Premixed H2-Air and H2–N 2-Air Flames in a Low-Swirl Injector for Ultralow Emissions Gas Turbines," *Journal for Gas Turbine and Power*, vol. 130, no. May 2008, pp. 1–9, 2008.

[45] R. K. Cheng, D. Littlejohn, P. A. Strakey, and T. Sidwell, "Laboratory Investigations of a Low-Swirl Injector with H2 and CH4 at Gas Turbine Conditions," *Proceedings of the Combustion Institute*, vol. 32, pp. 3001–3009, 2009.

[46] D. Littlejohn, R. K. Cheng, D. R. Noble, and T. Lieuwen, "Laboratory Investigations of Low-Swirl Injectors Operating with Syngases," *Journal of Engineering for Gas Turbines and Power*, vol. 132, no. 1, pp. 011502–011502–8, 2009.

[47] D. Beerer, V. McDonell, P. Therkelsen, and R. K. Cheng, "Flashback, Blow out, Emissions, and Turbulent Displacement Flame Speed Measurements in a Hydrogen and Methane Fired Low-swirl Injector at Elevated Pressures and Temperatures," in *Proceedings of ASME Turbo Expo 2012*, pp. 1–12, 2012.

[48] D. Beerer, V. McDonell, P. Therkelsen, and R. K. Cheng, "Flashback and Turbulent Flame Speed Measurements in Hydrogen / Methane Flames Stabilized by a Low-Swirl Injector at Elevated Pressures and Temperatures," *Journal of Engineering for Gas Turbines and Power*, vol. 136, no. March 2014, pp. 1–9, 2014.

[49] A. Colorado and V. Mcdonell, "Emissions and Stability Performance of a Low-Swirl Burner Operated on Simulated Biogas Fuels in a Boiler Environment," *Applied Thermal Engineering*, vol. 130, pp. 1507–1519, 2018.

[50] R. K. Cheng and D. Littlejohn, "Effects of Combustor Geometry on the Flowfields and Flame Properties of a Low-Swirl Injector," in *Proceedings of the GT2008 ASME Turbo Expo 2008: Power for Land Sea and Air*, pp. 1–16, 2008.

[51] J. B. Bell, R. K. Cheng, M. S. Day, V. E. Beckner, and M. J. Lijewski, "Interaction of Turblence and Chemistry in a Low-swirl Burner," *Journal of Physics: Conference Series*, vol. 125, 2008.

[52] J. B. Bell, M. S. Day, and M. J. Lijewski, "Simulation of Nitrogen Emissions in a Premixed Hydrogen Flame Stabilized on a Low Swirl Burner," *Proceedings of the Combustion Institute*, vol. 34, no. 1, pp. 1173–1182, 2013.

[53] J. B. Bell, R. K. Cheng, M. S. Day, and I. G. Shepherd, "Numerical Simulation of Lewis Number Effects on Lean Premixed Turbulent Flames," in *Proceedings of the Combustion Institute*, vol. 31, pp. 1309–1317, 2007.

[54] M. Day, S. Tachibana, J. Bell, M. Lijewski, V. Beckner, and R. K. Cheng, "A Combined Computational and Experimental Characterization of Lean Premixed Turbulent Low Swirl Laboratory Flames, I. Methane Flames," *Combustion and Flame*, vol. 159, pp. 275–290, 2012.

[55] M. Day, S. Tachibana, J. Bell, M. Lijewski, V. Beckner, and R. K. Cheng, "A Combined Computational and Experimental Characterization of Lean Premixed Turbulent Low Swirl Laboratory Flames II. Hydrogen Flames," *Combustion and Flame*, vol. 162, pp. 2148–2165, 2015.

[56] P. Petersson, J. Olofsson, C. Brackman, H. Seyfried, J. Zetterberg, M. Richter, M. Aldén, M. A. Linne, R. K. Cheng, A. Nauert, D. Geyer, and A. Dreizler, "Simultaneous PIV/OH-PLIF, Rayleigh Thermometry/OH-PLIF and Stereo PIV Measurements in a Low-swirl Flame," *Applied Optics*, vol. 46, no. 19, pp. 3928–3936, 2007.

[57] K. J. Nogenmyr, X. S. Bai, C. Fureby, P. Petersson, R. Collin, M. Linne, and M. Alden, "A Comparative Study of LES Turbulent Combustion Models Applied to a Low Swirl Lean Premixed Burner," in *46th AIAA Aerospace Sciences Meeting and Exhibit*, pp. 1–14, 2008.

[58] K. Nogenmyr, C. Fureby, X. S. Bai, P. Petersson, R. Collin, and M. Linne, "Large Eddy Simulation and Laser Diagnostic Studies on a Low Swirl Stratified Premixed Flame," *Combustion and Flame*, vol. 156, pp. 25–36, 2009.

[59] K. Nogenmyr, P. Petersson, X. S. Bai, C. Fureby, R. Collin, A. Lantz, M. Linne, and M. Alden, "Structure and Stabilization Mechanism of a Stratified Premixed Low Swirl Flame," in *Proceedings of the Combustion Institute*, vol. 33, pp. 1567–1574, 2011.

[60] P. Petersson, R. Wellander, J. Olofsson, H. Carlsson, C. Carlsson, B. B. Watz, N. Boetkjaer, M. Richter, M. Aldén, L. Fuchs, and X.-s. Bai, "Simultaneous High-Speed PIV and OH PLIF Measurements and Modal Analysis for Investigating Flame-flow Interaction in a Low Swirl Flame," in *16th Int Symp on Applications of Laser Techniques to FLuid Mechanics*, pp. 1–12, 2012.

[61] H. Carlsson, E. Nordström, A. Bohlin, P. Petersson, Y. Wu, R. Collin, M. Aldén, P.-E. Bengtsson, and X.-S. Bai, "Large Eddy Simulations and Rotational CARS / PIV / PLIF Measurements of a Lean Premixed Low Swirl Stabilized Flame," *Combustion and Flame*, vol. 161, pp. 2539–2551, 2014.

[62] H. Carlsson, E. Nordström, A. Bohlin, Y. Wu, B. Zhou, Z. Li, M. Aldén, P.-E. Bengtsson, and X.-S. Bai, "Numerical and Experimental Study of Flame Propagation and Quenching of Lean Premixed Turbulent Low Swirl Flames at Different Reynolds Numbers," *Combustion and Flame*, vol. 162, no. 6, pp. 2582–2591, 2015.

[63] D. M. Kang, F. E. C. Culick, and A. Ratner, "Combustion Dynamics of a Low-swirl Combustor," *Combustion and Flame*, vol. 151, pp. 412–425, 2007.

[64] Y. Huang and A. Ratner, "Experimental Investigation of Thermoacoustic Coupling," *Journal of Propulsion and Power*, vol. 25, no. 2, pp. 365–373, 2009.

[65] D. W. Davis, P. L. Therkelsen, D. Littlejohn, and R. K. Cheng, "Effects of Hydrogen on the Thermo-acoustics Coupling Mechanisms of Low-swirl Injector Flames in a Model Gas Turbine Combustor," in *Proceedings of the Combustion Institute*, vol. 34, pp. 3135–3143, The Combustion Institute, 2013.

[66] S. Tachibana, K. Kanai, S. Yoshida, K. Suzuki, and S. Tetsuya, "Combined Effect of Spatial and Temporal Variations of Equivalence Ratio on Combustion Instability in a Low-swirl Combustor," in *Proceedings of the Combustion Institute*, vol. 35, pp. 3299–3308, The Combustion Institute, 2015.

[67] A. Renaud, T. Yokomori, and S. Tachibana, "Study of a Thermo-acoustic Instability Triggering in a Low-swirl Burner Using Simultaneous Time-resolved Acetone and OH-PLIF," in *Proceedings of the Combustion Institute*, vol. 37, pp. 2627–2633, Elsevier Inc., 2019.

[68] P. A. Strakey and G. Eggenspieler, "Development and Validation of a Thickened Flame Modeling Approach for Large Eddy Simulation of Premixed Combustion," *Journal of Engineering for Gas Turbines and Power*, vol. 132, no. July 2010, pp. 1–9, 2010.

[69] M. Koyama and S. Tachibana, "Technical Applicability of Low-swirl Fuel Nozzle for Liquid-fueled Industrial Gas Turbine Combustor," *Fuel*, vol. 107, pp. 766–776, 2013.

[70] P. L. Therkelsen, D. Littlejohn, and R. K. Cheng, "Parametric Study of the Low-swirl Injector Geometry on its Operability," in *Proceedings of ASME Turbo Expo 2012*, 2012.

[71] N. Peters, "Laminar Flamelet Concepts in Turbulent Combustion," in *Twenty-first Symposium (International) on Combustion/The Combustion Institute*, pp. 1231–1250, 1986.

[72] N. Peters, *Turbulent Combustion*. Cambridge: Cambridge University Press, 2000.

[73] G. Damkohler, "The Effect of Turbulence on the Flame Velocity in Gas Mixtures," tech. rep., National Advisory Committee for Aeronautics, 1940.

[74] S. B. Pope, *Turbulent Flows*. Cambridge University Press, 1st ed., 2000.

[75] P. E. Roach, "The Generation of Nearly Isotropic Turbulence by Means of Grids," *International Journal of Heat and Fluid Flow*, vol. 8, no. 2, pp. 82–92, 1987.

[76] R. K. Cheng, "Fundamental Flame / Turbulence Interactions of Premixed Combustion," tech. rep., Keio University, Tokyo, 2017.

[77] P. L. Therkelsen, D. Littlejohn, R. K. Cheng, J. E. Portillo, and S. M. Martin, "Effect of Combustor Inlet Geometry on Acoustic Signature and Flow Field Behaviour of the Low Swirl Injector," in *Proceedings of the ASME Turbo Expo 2010: Power for Land, Sea, and Air*, pp. 1–12, 2010.

[78] R. K. Cheng, A. Frank, P. L. Therkelsen, and V. H. Rapp, "Demonstration of Industrial System with Real-time Response to Fuel Stock Variability," tech. rep., California Energy Commission, 2018.

[79] J. F. Driscoll, "Turbulent premixed combustion: Flamelet structure and its effect on turbulent burning velocities," *Progress in Energy and Combustion Science*, vol. 34, no. 1, pp. 91–134, 2008.

[80] M. Wernet, "Fuzzy Logic Enhanced Digital PIV Processing Software," in *18th International Congress on Instrumentation for Aerospace Simulation Facilities*, (Toulouse), 1999.

[81] C. Mercer, ed., *Optical Metrology for Fluids, Combustion and Solids*. Springer, 2003.

[82] Degussa, "AEROSIL® Fumed Silica and AEROXIDE® Fumed Metal Oxides for Toners," tech. rep., degussa, 2006.

[83] A. Melling, "Tracer Particles and Seeding for Particle Image Velocimetry," *Measurement Science and Technology*, vol. 8, pp. 1406–1416, 1997.

[84] C. J. Lawn and R. W. Schefer, "Scaling of premixed turbulent flames in the corrugated regime," *Combustion and Flame*, vol. 146, no. 1-2, pp. 180–199, 2006.

[85] Y. A. Cengal and J. M. Cimbala, *Fluid Mechanics - Fundamentals and Applications*. McGraw-Hill, 2006.

[86] J. B. Bell, M. S. Day, I. G. Shepherd, M. R. Johnson, R. K. Cheng, J. F. Grcar, V. E. Beckner, and M. J. Lijewski, "Numerical Simulation of a Laboratory-scale Turbulent V-flame," *PNAS*, vol. 102, no. 29, pp. 10006–10011, 2005.

[87] A. Frank, P. Therkelsen, M. Sierra Aznar, V. H. Rapp, R. K. Cheng, and J.-y. Chen, "Investigation of the Down-Scaling Effects on the Low Swirl Burner and its Application to Microturbines," in *Proceedings of the ASME Turbo Expo: Power for Land, Sea and Air*, (Oslo), 2018.

Appendix A

Development of a Microturbine CHP Combustor

This section is based on the publication by Frank et al. [87].

A.1 Application of the LSB to the Microturbine

The LSB that was developed for the 1 kW microturbine and described in the results section was also adopted and integrated into the MDC hardware which has a unique set of requirements that are different than the LSB alone. Pertinent parameters for the development of the combustion system for the MDC gas turbine are the packaging constraints and the cycle conditions. Table A.1 shows the required combustor inlet and outlet conditions as estimated by MDC.

	Inlet	**Outlet**
Temperature (K)	946.5	1175
Pressure (atm)	2.93	2.23
Total Air Mass Flow Rate (g/s)	10.28	
Total Fuel Mass Flow Rate (g/s)	0.06	

Table A.1: Combustor target inlet and outlet conditions

In this system, the recuperator feeds the combustor with hot air limiting the temperature rise across the combustor to 228.5 K. This low temperature rise in combination with high mass flow rate poses a challenge to the development of the combustor because even at lean conditions, well below stoichiometric ($\phi < 0.75$), the temperature rise from combustion surpasses 1300 K which therefore requires a large mass flow rate of bypass air. Additionally, the combustor in order to fit within the design space cannot exceed 150 mm in length and 63.5 mm in diameter. As a result, a single can style combustor that utilizes a single stream of recuperator discharge air and supplies the turbine with a single stream of heated air was designed.

After successfully validating the LSB as a viable microturbine combustor (performance shown previously in the results section), it was then necessary to integrate the

stand-alone LSB into a can-style combustor for the microturbine. There were several challenges on the path to achieving this goal, one being that since there is only one air inlet to the combustor, it was necessary to have the air split between the primary and secondary air streams. While a valve could have been used to control the flow rate split, a passive system utilizing flow areas as a tuning parameter for the flow split was utilized. The resulting geometry yielded a 15.4% of the total mass flow reaching the burner while the remainder is diverted through the dilution holes downstream. Another design challenge was the effect of the secondary air dilution on the LSB stability and also the possibility of quenching of the post flame hot combustion gases by the cool secondary air that could possibly generate high emissions.

Figure A.1 shows a sectional analysis with a schematic of the flow paths for the can combustor. In this design, as the total mass air flow enters the combustor it then splits between the primary (combustion) and bypass (secondary) air streams. The primary air is immediately mixed with the fuel via a cross flow mounted injector where the air/fuel mixture then flow to the LSB swirler. The size and location of these holes as well as vertical positioning were determined via the use of computational fluid dynamics in order to provide the best possible fuel/air mixing. The fuel nozzle features 10 (5 on each side) 0.30 mm diameter holes drilled into a 0.1515 mm stainless steel tube. The fuel/air mixture then flows to the LSB swirler and through a 14 mm long tube before reaching the quarl which then expands to the combustor wall diameter of 44.45 mm. The length of the combustor liner was sized in order to allow sufficient time for burnout to occur before the secondary air is injected. The secondary air flows around the combustor, both cooling the wall and then combining with the primary flow downstream through twelve 8 mm diameter holes. The outside diameter of the lower portion of the combustor is 50.8 mm whereas the upper, wider portion measures 60.5 mm. Lastly, the overall length of this combustor measures 184 mm. The prototype fabricated combustor is shown in Figure A.2 which is made of stainless steel. The final combustor will be entirely fabricated out of Hastelloy X for high temperature durability and cost effectiveness.

The experimental setup previously shown in Figure 3.6 was modified in order to test the developed combustor. Instead of a mass flow controller to set the air flowrate, a Hoffer 1.5" turbine meter was used due to the large flow rate. Since turbine meters only measure the flow and do not control it, a large ball valve was installed and the flow was manually adjusted to the desired flow rate.

Emissions (Figure A.3) were measured in the experimental apparatus for the can combustor for varying fuel flow rates with a constant air flow rate mimicking the microturbine conditions. It can be seen that NO_x and CO emissions meet the target at the design point of 3.33 kW, however the margin to target is lower than was seen in the LSB alone. The values at the design condition are 0.175 lb/MW-hr (62.16 ppmdv @ 15% O_2) and 0.089 lb/MW-hr (6.35 ppmdv @ 15% O_2) for CO and NO_x respectively. This increase can be attributed to two separate effects. One being that the equivalence ratio within the combustor is no longer a known parameter and can only be inferred from the exhaust O_2 measurements since the airflow split between the two flow paths cannot be measured. For the points measured, the exhaust O_2 value showed that the combustor was running approximately 0.10 higher (richer)

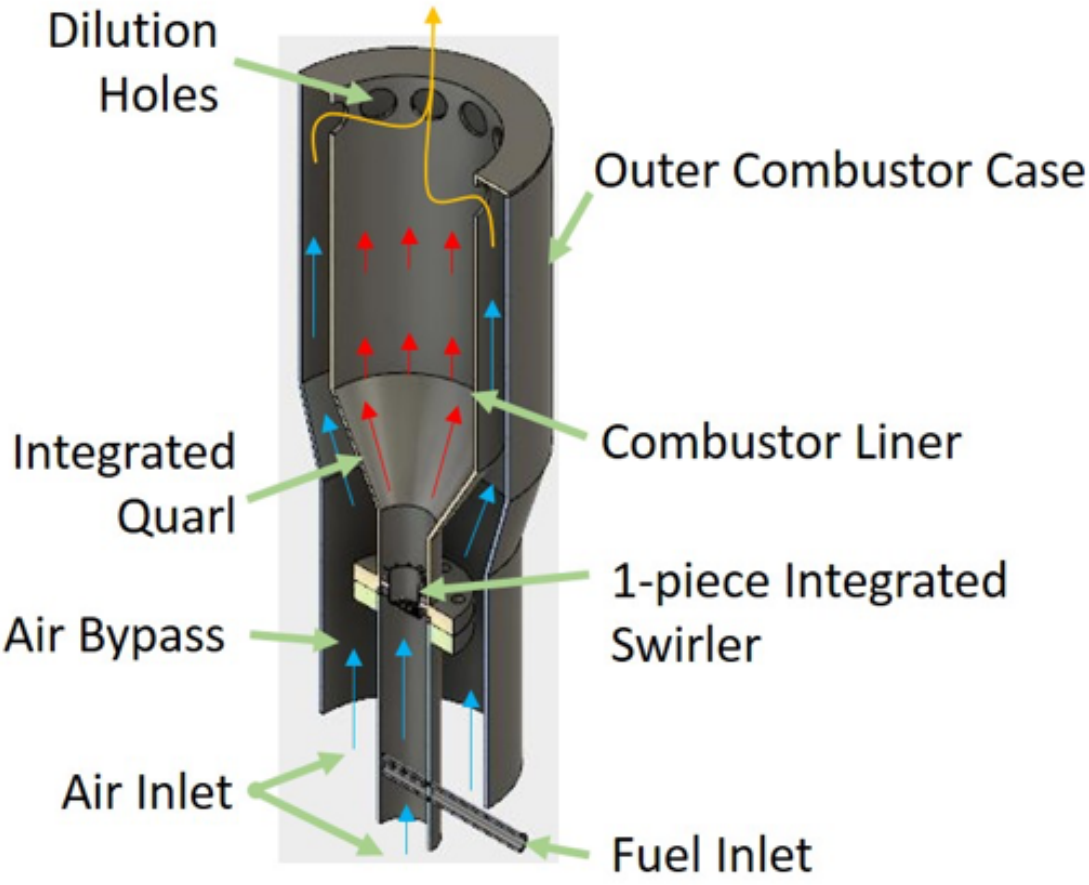

Figure A.1: Section analysis of the microturbine can combustor.

in equivalence ratio. Secondly, quenching from the cooled wall is believed to create higher CO emissions. Future work will involve optimizing the equivalence ratio within the combustor to further reduce emissions. Lastly, the pressure drop of this entire system was measured to be 0.9%, thus meeting the 3% GENSETS program target. The experimental results for the emissions, stability, and pressure drop therefore show the applicability of the LSB for the future generation of low emissions microturbines.

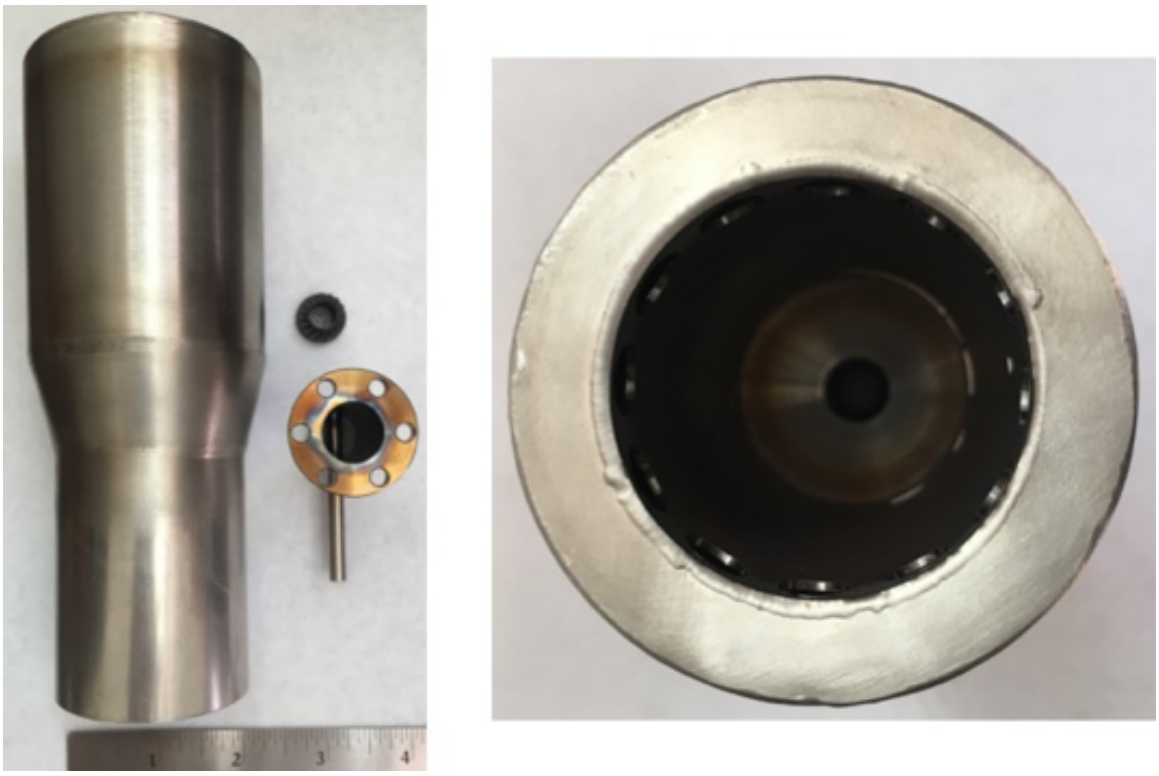

Figure A.2: GENSETS fabricated combustor showing a side view (left) and a top view (right).

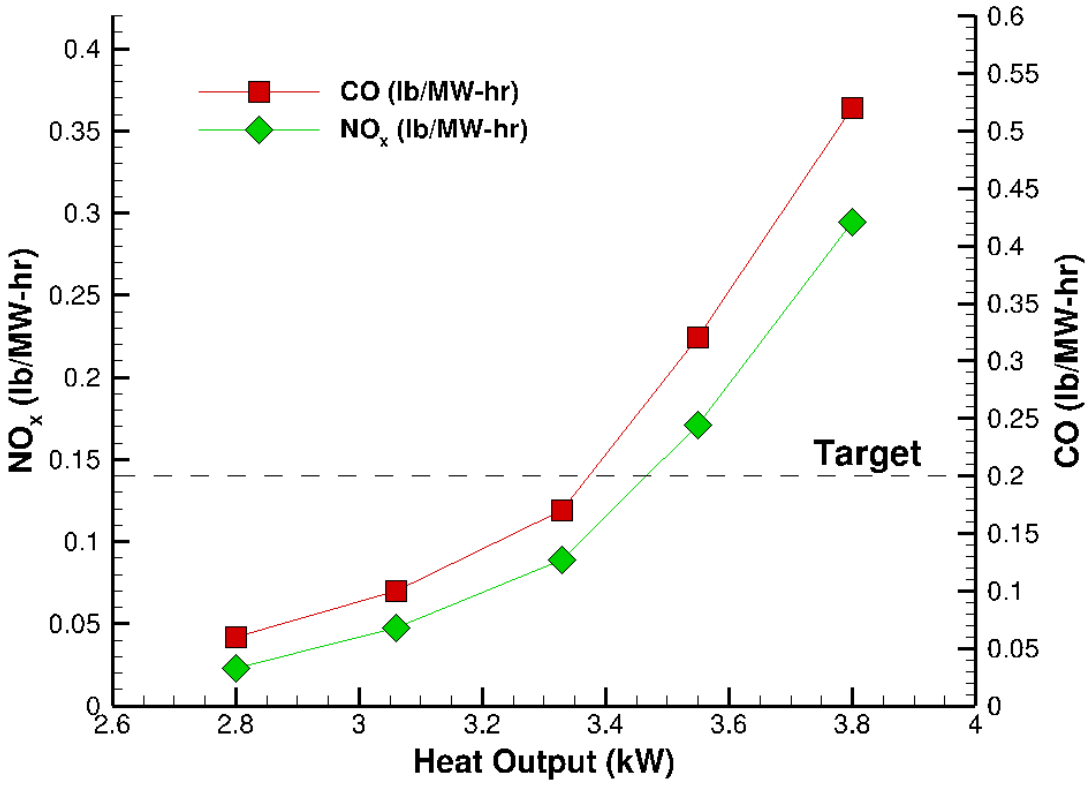

Figure A.3: GENSETS LSB can combustor NO_x and CO emissions at varying heat output

Appendix B

US Provisional Patent: Ultra-Low NOx Emissions Low Swirl Gas Turbine Combustor

Ultra-low NOx emissions low swirl gas turbine combustor

Inventors: Peter Therkelsen, and Aaron Alexander Frank

CROSS REFERENCE TO RELATED APPLICATIONS

[0001] Not applicable

STATEMENT OF GOVERNMENTAL SUPPORT

[0002] The invention described and claimed herein was made in part utilizing funds supplied by the U.S. Department of Energy under Contract No. DE-AC02-05CH11231 between the U.S. Department of Energy and the Regents of the University of California for the management and operation of the Lawrence Berkeley National Laboratory. The government has certain rights in this invention.

BACKGROUND OF THE INVENTION

Field of the Invention

[0003] The present invention relates to the field of low swirl gas turbine combustors.

Related Art

[0004] The application disclosure relates to burner assemblies, specifically, low emissions and low pressure drop burners with applications in gas turbines, sterling engines, among others requiring an enclosed continuous fuel and air mixture that produces a continuous heat (hot gas) output.

BRIEF DESCRIPTION OF THE DRAWINGS

[0005] The foregoing aspects and others will be readily appreciated by the skilled artisan from the following description of illustrative embodiments when read in conjunction with the accompanying drawings.

[0006] Figure 1 illustrates

DETAILED DESCRIPTION

[0007] In the discussions that follow, various process steps may or may not be described using certain types of manufacturing equipment, along with certain process parameters. It is to be appreciated that other types of equipment can be used, with different process parameters employed, and that some of the steps may be performed in other manufacturing equipment without departing from the scope of this invention. Furthermore, different process parameters or manufacturing equipment could be substituted for those described herein without departing from the scope of the invention.

[0008] These and other details and advantages of the present invention will become more fully apparent from the following description taken in conjunction with the accompanying drawings.

[0009] In this application we disclose an apparatus and process for combining a fuel and air mixture that is burned in a combustion chamber utilizing the combination of a swirling and non-swirling air/fuel mixture. The apparatus is configured to mix a fuel stream with an air stream in order to produce a fully homogeneous and uniform flow through a channel. This flow then passes through a mechanical swirler which produces a swirling and non-swirling fuel/air mixture. This device is also configured to mix a second "bypass" stream of air with the combustion products which serves to cool and dilute the mixture, lowering the device exit temperature and providing the desired total flow rate. This bypass air flow enters the apparatus in parallel to the air utilized for combustion and flows around the combustor, entering the into the combustion products downstream, near the exit of the apparatus. The process comprises the steps of discharging the fuel stream into the flowing air stream which then flows through the channel to produce a non-swirling and swirling flow. The process further comprises the step of flowing the bypass air around the swirler and non-swirling flow which then later combines with this flow downstream.

[0010] The following document is attached to this Provisional Application, and is incorporated herein by reference as if fully set out in their entirety: "Disclosure of Low Swirl Injector Combustion System".

Claims

1. An air/fuel combustion system comprising

a mechanical device to divide airflow between two concentric channels

an air/fuel transfer tube designed to discharge air into a combustion chamber,

a fuel supply tube that discharges fuel into the central channel

a central channel which holds the mechanism for the low swirl injector

a duct which carries air around the central channel and combustion chamber and discharges it into the combustion chamber downstream of the combustion products.

2. A low swirl injector comprising of:
a channel carrying the fuel/air mixture which has passed through the low swirl injector

a passage adapted to impart a swirl onto the flow through angular momentum

a flow balancing insert where said fuel balancing insert introduces a pressure drop which serves as a means to direct the flow.

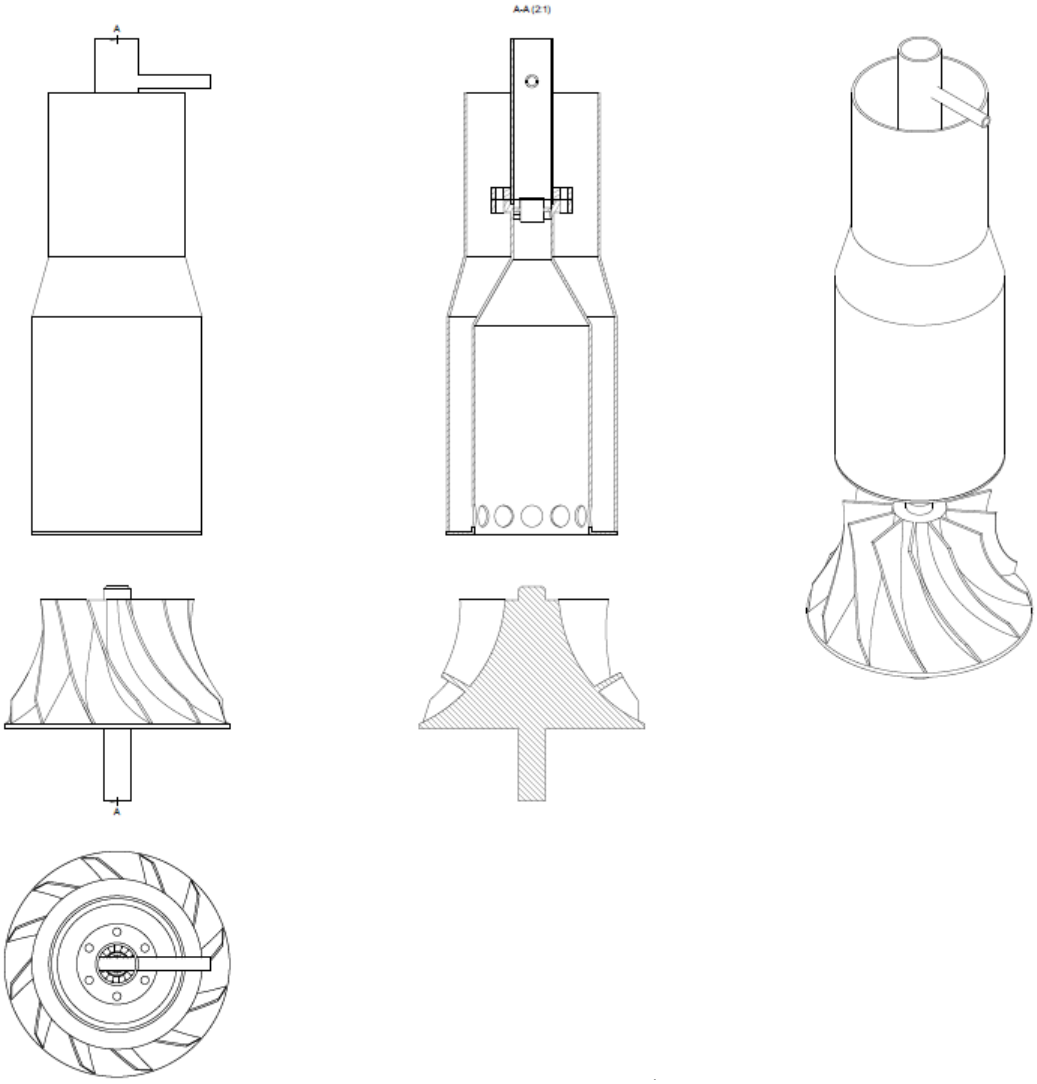

FIG. 1